Università degli Studi di Pisa

Facoltà di Scienze Matematiche, Fisiche e Naturali

Corso di Laurea in Geofisica d'Esplorazione ed Applicata

Tesi di Laurea Magistrale

Algorithmic Seismic predictions of overpressure in AVA in fluid line

Relatore:

prof. Alfredo Mazzotti

Correlatore:

dott. Mattia Aleardi

Laureando:

Natale Cristian Rugna

ANNO ACCADEMICO 2015–2016

Ringraziamenti

Il ringraziamento più grande va ai miei genitori per avermi sostenuto in questo percorso universitario, assieme a loro ringrazio mia nonna.

Un grazie infinito va a tutti gli amici di Pisa, che in questi anni sono stati come una seconda famiglia.

Un ringraziamento speciale al prof. Mazzotti e al dott. Aleardi per gli insegnamenti dati durante il mio percorso di laurea magistrale.

Abstract

The subject of detection of abnormally high pressured zones from seismic has received a great deal of attention in exploration and production geophysics because of increasing activities in frontier areas or offshore and a need to lower cost without compromising safety and environment, and managing risk and uncertainty associated with very expensive drilling. An estimation of pore pressure can be obtained from seismic velocity as well as from well logs. Pore pressure is one of the most important parameters for drilling plan and for geomechanical and geological analyses. If the pore pressure is higher than the hydrostatic pressure (normal pore pressure), it is abnormal pore pressure. When pore pressure exceeds the normal pressure, it is overpressure. In the present study, amplitude variation with angle (AVA), will be evaluated. AVA analysis can provide important information about reservoir rocks such as lithology, porosity, and pore fluids that can be used to reduce hydrocarbon exploration risk. Seismic amplitudes reflecting from an interface change when the angle increases between the source and receveir points at the surface. AVA analysis is normally carried out in a deterministic way to predict lithology and fluids from seismic data. Amplitude variation with angles (AVA) interpretations may be facilitated by crossplotting the AVA Intercept (A) and Gradient (B). In the present study an algorithm has been developed, with the goal to discover wheter it was possible to predict overpressure phenomenons from the seismic data. It considers and compares an AVA Analytical and Experimental response. In the AVA Experimental response, well logs of the seismic velocities and density have been exploited to derive the synthetic seismograms (CMP) using the convolutional method, and the Intercept and Gradient values extracted from synthetic seismograms. In the AVA analytical response well logs of the seismic velocities have been used, and the Intercept and Gradient values extracted from the velocities (Vp, Vs) and density well logs. The strategy followed to tackle the problem has been Shuey's approximation. Shuey's approximation was used for AVA crossplot analysis. The primary attributes extracted for AVA analysis are Intercept (A) and the Gradient (B), which are obtained from velocity corrected CMP records. This Gradient ("slope") AVA attribute is calculated from a least square regression analysis of the amplitudes for angles from 0-30 degrees, using an X-axis of sine squared theta (where theta is the incidence angle), and the Intercept is zero-offset amplitude determined (using an Y-axis the amplitude) by extrapolating the AVA Gradient. This yields two AVA attributes, basically the Slope and Intercept of a straight

line, which describes, in simpler terms how the amplitude behaves with angle of incidence. Each point in the AVA crossplot is mapped using the amplitude of Intercept (A) and Gradient (B) in a time window. The extraction provides band-limited information on which attempt to discover anomalies caused by overpressure phenomens. AVA crossplotting can play a significant role in minimizing the risk associated with an exploration play. The stability of the Background Trend (Vp/Vs) can have an impact on what is being interpretated as anomalous, be it fluid or lithology induced outliers. The third and fourth chapters deal with the direct problem. We shall start with an initial model in which the Vp/Vs ratio is known, after which I shall apply Shuey's approximation, and through the methodology of least squares and the " Singular Value Decomposition" method, I obtain two values of Vp/Vs to predict two empirical equations, Costant Density and Gardner Density. Several examples were evaluated. The first example, it started from a Vp/Vs model that varied linearly. The second example added a bit of random noise to the initial model (Vp/Vs). The third example is considered to show the correct relationship of Vp/Vs. The fourth example considered a ratio Vp/Vs that varied linearly from 4 to 2 and then returned again to a ratio of Vp/Vs = 4, with the addition of random noise. As previously explained, it is considered an AVA Analytical and Experimental response. Using an Analytical AVA response, the Vp/Vs ratio that was predicted was very close to the Vp/Vs ratio of the initial model. Using an Experimental AVA response, the predicted Vp/Vs ratio deflected from the Vp/Vs ratio of the initial model, especially when we consider the Gardner Density equation. This present study, attempts to define a low resolution profile of Vp/Vs ratio and not its local variations of high frequency. It was necessary to study many strategies which make the method robust and reliable. The present study is partitioned in four chapters. The first chapter attempts to analyze the problems of overpressure from the theoretical and practical points of view. The second chapter focuses on the use of AVA seismic attributes, and how that seismic attribute can provide information about possible presence of overpressure from seismic data. The third and fourth chapters illustrate the algorithm developed in Matlab and provide information about the possible presence of overpressure.

Index

Chapter 1

Basic pressure concepts

This chapter provides general information about the pressure theory. It indroduces the terminology used to describe the various types of pressure that are encountered during drilling. It explains the different mechanisms can generate overpressure phenomenons. It indroduces some methods of pore pressure prediction.

1.1 Definitions and pressure concepts

Pore pressure is defined as the fluid pressure in the pore space of the rock matrix. In a geologic setting with perfect communication between the pores, the pore pressure is the hydrostatic pressure due to the weight of the fluid. The pore pressure at depth z can then be computed as :

$$Ph = \rho f g z \tag{1.1}$$

where z, ρf and g are the height of the column, the fluid density, and acceleration due to gravity, respectively. The size and shape of the cross-section of the fluid column have no effect on hydrostatic pressure. The fluid density depends on the fluid type, concentration

of dissolved solids and gasses in the fluid column, and the temperature and pressure. Thus, in any given area, the fluid density is depth dependent. In SI system, the unit of pressure is pascal (abbreviated by Pa), and in the British system, the uniti is pounds per square inch (abbreviated by psi). We note that 1 Pa= 1.45×10^{-4} psi = 1 N/m^2 . This is a rather small unit and for most practical applications, it is customary to use megapascals (MPa), where 1 MPa = 10^6 N/m^2 . The formation pressure gradient, expressed usually in pounds per square inch per foot (abbreviated by psi/ft) in the British system of units, is the ratio of the formation pressure, P (in psi) to the depth, z (in feet). It is not the true instantaneous gradient, dP/dz. Hydrostatic pressure is often referred to as normal pressure conditions. Conditions that deviate from normal pressure are said to be either overpressured or underpressured, depending on whether the pore pressure is greater than or less than the normal pressure. In general, the hydrostatic pressure gradient, Pg(in psi/ft), can be defined by

$$Pg = 0.433 \times \text{fluid density (in } g/cm^3 \text{).} \tag{1.2}$$

The overburden pressure $S(z)$ is defined as the combined weight of sediments and fluid in the pore space overlying a formation. Mathematically, the overburden pressure can be defined as

$$S(\mathrm{z}) = \mathrm{g} \int_0^{\mathrm{z}} \rho\,(\mathrm{z})\ \mathrm{g}\ \mathrm{dz} \tag{1.3}$$

where

$$\rho\,(z) = \phi\,(z)\,\rho f\,(z) + \big(1 - \phi\,(z)\big)\,\rho m\,(z). \tag{1.4}$$

In equation (1.4), ϕ is the porosity , while ρf and ρm are the fluid and rock matrix densities, respectively. If the density is known, the overburden pressure can be measured.

The overburden pressure is depth dependent and increases with depth. The overburden pressure ha salso been referred to as the geostatic or lithostatic pressure [Dutta, 2002].

The effective pressure or differential pressure is defined as

$$Pe = S - n\,p, \tag{1.5}$$

Where p is the pore fluid pressure, and n is called the Biot coefficitent. For static compression of the rock frame, the Biot coefficient is defined as (Fjær, 1989)

$$n = 1 - \frac{Kfr}{Ks} \tag{1.6}$$

where Kfr is the bulk modulus of the rock frame and Ks is the bulk modulus of the mineral that the rock is composed of. For soft materials, n = 1.

Pore pressure can be calculated from Eq. (1.5) when one knows overburden and effective stresses. Overburden stress can be easily obtained from bulk density logs, while effective stress can be correlated to well log data, such as resistivity, sonic travel time/velocity, bulk density and drilling parameters. Fig. (1.1) demonstrates the hydrostatic pressure, formation pore pressure, overburden stress and vertical effective stress with the true vertical depth (TVD) in a typical oil and gas exploration well. The pore pressure profile with depth in this field is similar to many geologically young sedimentary basins where overpressure is encountered at depth. At relatively shallow depths (less than 2,000 m), pore pressure is hydrostatic, indicating that a continuous, interconnected column of pore fluid extends from the surface to that depth. Deeper than 2,000 m the overpressure starts, and pore pressure increases with depth rapidly, implying that the deeper formations are hydraulically isolated from shallower ones. By 3,800 m, pore pressure reaches to a value close to the overburden stress, a condition referred to as hard 106 overpressure. The

effective stress is conventionally defined to be the subtraction of pore pressure from overburden stress, as shown in Fig. (1.1). The increase in overpressure causes reduction in the effective stress. The pore pressure gradient is more practically used in drilling engineering, because the gradients are more convenient to be used for determining mud weight (or mud density), as shown in (Fig. 1.2). The pore pressure gradient at a given depth is the pore pressure divided by the true vertical depth. The mud weight should be appropriately selected based on pore pressure gradient, wellbore stability and fracture gradient prior to setting and cementing a casing. The drilling fluid (mud) is applied in the form of mud pressure to support the wellbore walls for preventing influx and wellbore collapse during drilling. To avoid fluid influx, kicks and wellbore instability in an open hole section, a heavier mud pressure than the pore pressure is needed. However, when mud weight is higher than the fracture gradient of the drilling section, it may fracture the formation, causing mud losses or even lost circulation. To prevent wellbore from hydraulic fracturing by the high mud weight, as needed where there is overpressure, casing needs to be set to protect the overlying formations from fracturing, as illustrated in (Fig. 1.2). Pressure gradients and mud weight are expressed in the metric unit, g/cm^{3}in Fig(1.2).

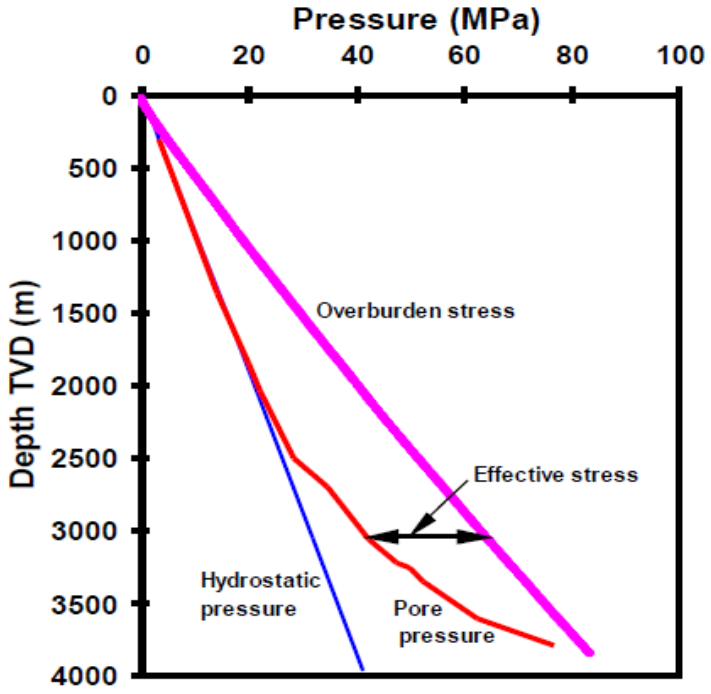

Fig. 1.1. Hydrostatic pressure, pore pressure, overburden stress, and effective stress in borehole (Figure from Zhang, 2011).

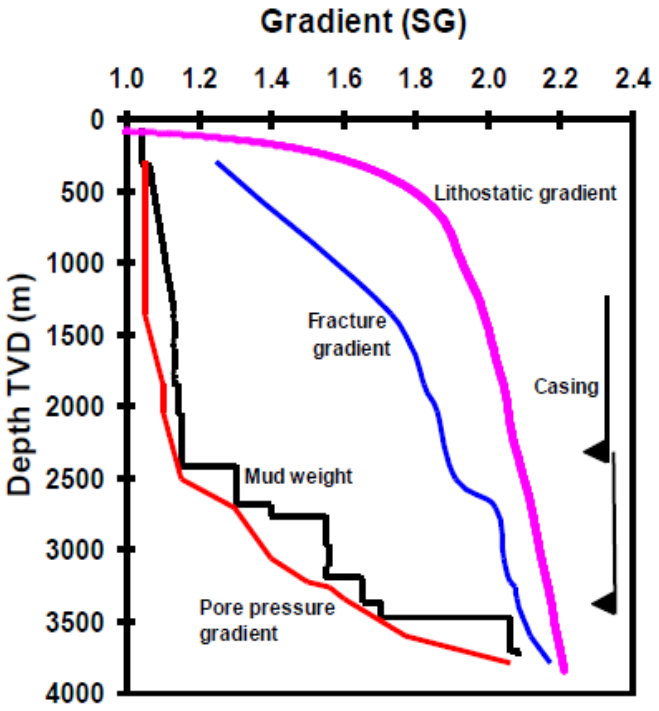

Fig. 1.2. Pore pressure gradient, fracture gradient, overburden stress gradient (lithostatic gradient),mud weight, and casing shoes with depth (Figure from Zhang, 2011).

Pore pressure analyses include three aspects: pre-drill pore pressure prediction, pore pressure prediction while drilling and post-well pore pressure analysis. The pre-drill pore pressure can be predicted by using the seismic interval velocity data in the planned well location as well as using geological, well logging and drilling data in the offset wells. The pore pressure prediction while drilling mainly uses the logging while drilling (LWD), measurement while drilling (MWD), drilling parameters, and mud logging data for analyses. The post-well analysis is to analyze pore pressures in the drilled wells using all available data to build pore pressure model, which can be used for pre-drill pore pressure predictions in the future wells.

Fracture pressure is the pressure required to fracture the formation and cause mud loss from wellbore into the induced fracture. Fracture gradient can be obtained by dividing the true vertical depth from the fracture pressure. Fracture gradient is the maximum mud weight; therefore, it is an important parameter for mud weight design in both drilling

planning stage and while drilling. If mud weight is higher than the formation fracture gradient, then the wellbore will have tensile failure (be fractured), causing losses of drilling mud or even lost circulation. Fracture pressure can be measured directly from downhole leak-off test (LOT). There are several approaches to calculate fracture gradient. The following two methods are commonly used in the drilling industry, the minimum stress method and tensile failure method.

1.2 Overpressure Mechanisms

Development of overpressure indicates that fluid movement is retarded both vertically and laterally. This can be caused by a rapid burial of low-permeability sediments (rapid enough to prevent compaction water to leave the system), or expansion of pore fluid from diagenetic and lithologic changes, or both [Hubbert and Rubey, 1959]. Some of the important mechanisms related to geopressure are:

1) Mechanical compaction disequilibrium.
2) Clay dehydration and alteration due to burial diagenesis.
3) Dipping or lenticular permeable beds embedded in shales.
4) Buoyancy.
5) Tectonism / uplift and erosion.
6) Aquatermal pressuring.

Mechanical compaction disequilibrium is believed to be the primary cause of geopressure in sedimentary basins [Hubert and Rubey, 1959]. There, low-permeability sediments (such as high-porosity clay) accumulate at rates faster than they can dewater and compact due to gravity. Therefore, the pore fluid is forced to support some portion of the combined weight of the overlying rocks and fluids. The magnitude of the overpressure due to mechanical disequilibrium and the depth where the pressure deviates from hydrostatic condition are dictated by the burial history of the sediments and the hydraulic communication with neighboring formations and faults. Smectite or swelling clay is a common component of clay, especially in the Gulf of Mexico. It contains a considerable amount of water bound

in the clay platelets. At 150–250±F, smectite begins to dehydrate and transform to illite, with potassium feldspar acting as a catalytic agent. This process releases interlayer bound water from the smectite into free pore water, and causes an additional increase in pore pressure and decrease of effective stress. In addition, the process also causes a longrange ordering of clay platelets and redistribution of effective stress (Hower et al., 1976). The interlayering of smectite and illite layers is characterized by an ordering parameter RN. RN means that at least N illite layers separate every pair of smectite layers [Dutta, 1987]. The entire process is kinetic in nature and controlled by the temperature and time history of burial of the sediments. The third mechanism, due to flow of fluids through dipping or lenticular sands, is a local phenomenon. When these sands are embedded in geopressured shales, they provide a very efficient mechanism by which high-pressured shales can dewater, especially if the sand has a considerable structural relief. This is because the sand has much higher permeability than the encasing shales which, in turn, causes the pore fluid pressure gradient within the sand to be hydrostatic. This causes a transmittal of high pressure from the downdip positions of the sands to their crestal positions. This can also happen when sands are juxtaposed by faulting. This phenomenon, in principle, can cause lateral changes in the velocity field around the sand with a significant structural relief. In the literature this has also been termed as the centroid phenomenon [Traugott, 1997]. Oil and gas are lighter than water. Hence, when water is replaced by hydrocarbons, it results in an increase in the pore pressure at the reservoir level due to buoyancy effect. The key factors that dictate the amount of overpressuring caused by this mechanism are the density of hydrocarbons, the height of the column of hydrocarbons, and the density of pore water at that depth. In provinces such as Orinoco Delta, Venezuela, Trinidad, Sumatra, and California, tectonic compression and shear (tectonic wrench faulting) can cause significant geopressure. Rapid uplifting and erosion of a sealed compartment, while maintaining the pore fluid pressure within the compartment, will also cause pore pressure to be abnormally high at its depth of burial. Seismic detection of pore pressure due to these mechanisms is very difficult. Aquathermal pressuring has been a much-discussed phenomenon in the literature. It is also controversial. This phenomenon is due to the fact that the coefficients of thermal expansion of pore fluids are greater than the corresponding coefficients of the rock matrix. Consequently, when a compartment is sealed and buried, the pore fluids are

subjected to a high pressure due to the pore fluid volume expansion caused by increased temperature. However, there is considerable disagreement as to how perfect the seal must be for this mechanism to significantly contribute to high pore pressure. As far as the seismic detection of abnormally high pore pressure is concerned, the first two mechanisms (mechanical compaction disequilibrium and clay dehydration) can be detected relatively easily compared to the remaining mechanisms. This is because the compaction properties of sediments dealing with both mechanical disequilibrium and clay dehydration are relatively well behaved and easier to describe and model using well-known rock physics and seismic principles. Further, these mechanisms can be reconciled with observations easier relative to the other mechanisms. However, there still remains a certain ambiguity; the contribution from the other mechanisms can never be ruled out completely.

1.3 Pore pressure prediction methods

Hottmann and Johnson were probably the first ones to make pore pressure prediction from shale properties derived from well log data (acoustic travel time/velocity and resistivity). They indicated that porosity decreases as a function of depth from analyzing acoustic travel time in Miocene and Oligocene shales in Upper Texas and Southern Louisiana Gulf Coast. This trend represents the “normal compaction trend” as a function of burial depth, and fluid pressure exhibited within this normal trend is the hydrostatic. If intervals of abnormal compaction are penetrated, the resulting data points diverge from the normal compaction trend. They contended that porosity or transit time in shale is abnormally high relative to its depth if the fluid pressure is abnormally high. Most methods of pore pressure predictions are based on Terzaghi’s effective stress relation [Terzaghi, 1943] that expresses elastic wave velocity as a function of vertical effective stress. Since the stress is normal, it can otherwise be called pressure and be used

interchangeably. If the relation between elastic wave velocity and vertical effective stress is known, the pore pressure P can be calculated from Equation (1.1), and the total overburden stress determined from Equation (1.3). Most common methods used for determining pore pressure from compressional seismic velocity include the Eaton's method, Bowers' method. The choice for each method depends on the overpressure generation mechanism in the area of interest. Browers calculated the effective stresses from measured pore pressure data of the shale and overburden stresses and analyzed the corresponded sonic interval velocities from well logging data. He proposed that the sonic velocity and effective stress a power relantionship as follows:

$$Vp = Vml + A\sigma^B \tag{1.7}$$

where Vp is the complessional velocity at a given depth; Vml is the compressional velocity in the mudline (the sea floor or the ground surface, normally Vml ≈5000 ft/s, or 1520 m/s); A and B are the parameters calibrated with offset velocity versus effective stress data. Rearranging Eq. (1.7) and considering $Pe = S(z) - Ph$, the pore pressure can be obtained from the velocity as described in Eq. (1.7), as:

$$Ph = S(z) - \frac{(Vp - Vml)}{(A)}^{1/B} \tag{1.8}$$

For Gulf of Mexico wells, A = 10-20 and B = 0.7-0.75 in the English units (with Ph, $S(z)$ in psi and vp, Vml in ft/s).

Eaton presented the following empirical equation for pore pressure gradient prediction from sonic compressional transit time:

$$Ppg = OBG - (OBG - Png)\left(\frac{\Delta tn}{\Delta t}\right)^3 \tag{1.9}$$

where Ppg is the formation pore pressure gradient; OBG is the overburden stress gradient; Png is the hydrostatic pore pressure gradient (normally 0.45 psi/ft or 1.03 MPa/km, dependent on water salinity), Δtn is the sonic transit time or slowness in shales at the normal pressure; Δt is the sonic transit time in shales obtained from well logging, and it can also be derived from seismic interval velocity. This method is applicable in some petroleum basins, but it does not consider unloading effects. This limits its application in geologically complicated area, such as formations with uplifts. To apply this method, one needs to determine the normal transit time (Δtn).

In young sedimentary basins where under-compaction is the major cause of overpressure, the Gulf of Mexico, North Sea, the well-log-based resistivity method can fairly predict pore pressure. Eaton (1972) presented the following equation to predict pore pressure gradient in shales using resistivity log:

$$Ppg = OBG - (OBG - Png)\left(\frac{R}{Rn}\right)^{n} \quad (1.10)$$

where R is the shale resistivity obtained from well logging; Rn is the shale resistivity at the normal (hydrostatic) pressure; n is the exponent varied from 0.6 to 1.5, and normally n = 1.2. Eaton's resistivity method is applicable in pore pressure prediction, particularly for young sedimentary basins, if the normal shale resistivity is properly determined. One approach is to assume that the normal shale resistivity is a constant.

In Eaton's original equation, it is difficult to determine the normal shale resistivity or the shale resistivity in the condition of hydrostatic pore pressure. One approach is to assume that the normal shale resistivity is a constant. However, the normal resistivity (Rn) is not a constant in most cases, but a function of the burial depth, as shown in Fig 1.2. Thus normal compaction trendline needs to be determined for pore pressure prediction. Based on the relationship of measured resistivity and burial depth in the formations with normal pressures, the following equation of the normal compaction trend of resistivity can be used :

$$Rn = Ro\, e^{bz} \tag{1.11}$$

Where Rn is the shale resistivity in the normal compaction condition; Ro is the shale resistivity in the mudline; b is the costant; and Z is the depth below the mudline. Substituting Eq. (1.11) into Eq. (1.10), the Eaton's resistivity equation can be expressed in the following form:

$$Ppg = OBG - (OBG - Png)\left(\frac{R}{R0e^{bz}}\right)^{n} \tag{1.12}$$

where R is the measured shale resistivity at depth of Z; Ro is the normal compaction shale resistivity in the mudline; b is the slope of logarithmic resistivity normal compaction trendline. A case study is examined to verify the adapted Eaton's resistivity method with depth dependence. The studied basini s located in a deepwater field in Green Canyon of the Gulf of Mexico, U.S.A [Zhang, 2011]. The water depth is 5000 ft, and the Tertiary formations are mainly shales (mudstones) with some sandstones. The target reservoir is located in the Miocene sandstones. Several offset wells are analyzed to examine pore pressures in this field. Fig (1.3) shows the pore pressure calculation in an oil well from the modiefild Eaton's resistivity method in this basin. Prior to the pore pressure calculation, the normal resistivity compaction trend is firstly analyzed based on Eq. (1.12), as shown in Fig. 1.3.a. With calibration of the measured pore pressure data, the normal compaction trendline is obtained with the following parameters in this basin.

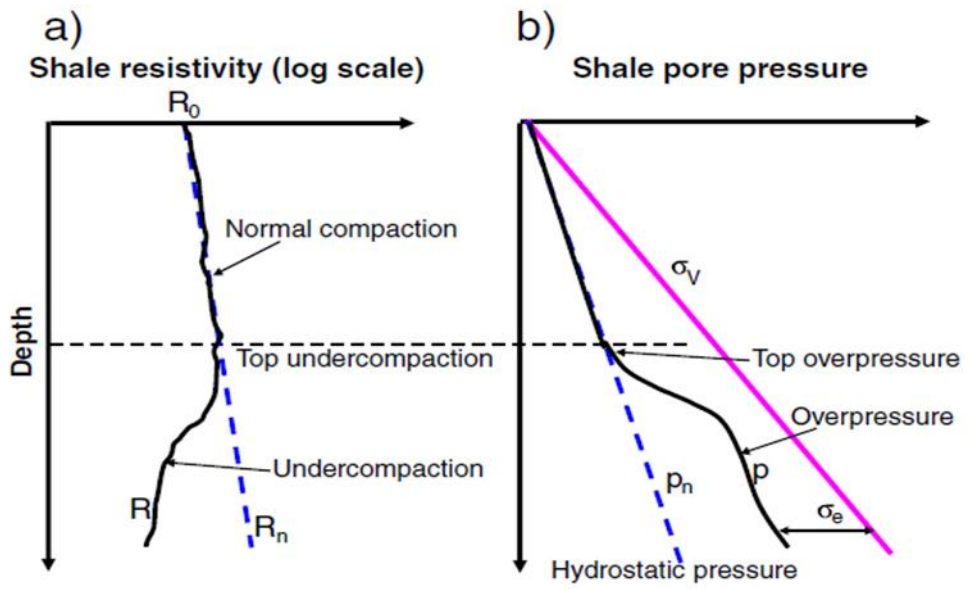

Fig. 1.3. Schematic resistivity (a) and pore pressure (b) in an undercompacted basin. The inclined line in (a) represents the resistivity in normally compacted formation (normal resistivity, *Rn*). In the under- compacted section the resistivity (*R*) reversal occurs, corresponding an overpressured formation in (b). In the under-compacted/overpressured section, resistivity is lower than that in the normalcompaction trendline (*Rn*). In the figure, σv or *S(z)* = lithostatic or overburden stress; σe or *Pe* = the effective vertical stress; *Pn* = normal pore pressure; p = pore pressure (Figure from Zhang, 2011).

Fig. 1.3 indicates that the formation is in normal compaction when depth is less than 4900 ft below the sea floor. Deeper than this depth (from 4900 to 7600 ft), the formation is slightly under-compacted with a lower resistivity than the normal compaction trend (Fig. 1.3.a), implying that the pore pressure increases, as shown in Fig. 1.3.b. From 7600 to 13,000 ft, the formation is further under-compacted and more elevated pore pressure exist. Fig 1.3 demonstrates that the adapted Eaton's resistivity method gives a fairly good result in pore pressure calculation. It should be noted that the pore pressure in the formation near the wellbore is affected by drilling-induced stresses [Zhang and Roegiers, 2005]. Therefore, in order to obtain the formation pore pressure the deep resistivity is needed for the pore pressure calculation.

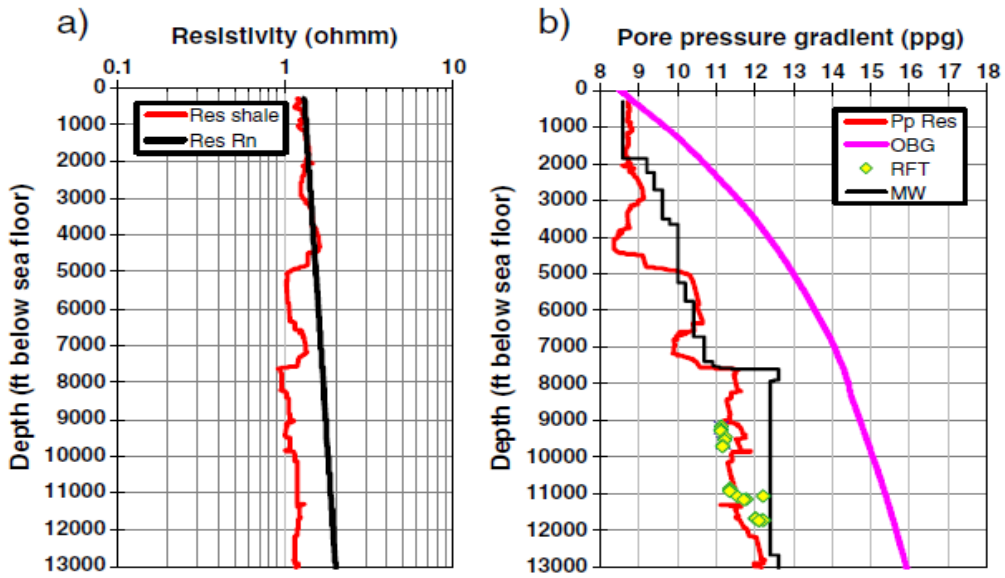

Fig.1.3. Pore pressure calculated by adapted Eaton's resistivity method with depth-dependent compaction trendline in a deepwater post-well analysis in the Gulf of Mexico. The left figure (a) plots the resistivity in shale and the normal resistivity calculated from Eq. (1.11), and the resistivity is plotted in logarithmic scale. The right figure (b) shows the overburden stress gradient (*OBG*), mud weight used while drilling (*MW*), measured pore pressure gradient (*RFT*) and pore pressure gradient (*Pp Res*) calculated from resistivity using Eq. (1.12), (Figure from Zhang, 2011).

Slotnick (1936) recognized that the compressional velocity is a function of depth, velocity increases with depth in the subsurface formations. Therefore, the normal compaction trendline of travel time should be a function of depth. The oldest and simplest normal compaction trend of seismic velocity is a linear relationship given by Slotnick (1936) in the following form:

$$V = V_0 + KZ \tag{1.13}$$

Where V is the seismic velocity at depth of Z; V_0 is the velocity in the ground surface or at the sea floor; K is a costant.

Sayers (2002) used this relationship as the normally pressured velocity for pore pressure prediction. A normal compaction trend for shale acoustic travel time with depth in the

Carnarvon Basin was established by fitting an exponential relationship to averaged acoustic travel times from 17 normally pressured wells [van Ruth, 2004]:

$$\Delta t_n = 225 + 391e^{-0.00103Z} \quad (1.14)$$

Where Δt_n is the acoustic transit time from the normal compaction trend at the depth of investigation (μs/m); Z in meters.

A similar relationship was used for a petroleum basin in Brunei [Tingay, 2009]:

$$\Delta t_n = 176.5 + 461.5e^{-0.0007Z} \quad (1.15)$$

Based on the data of the measured sonic transit time in the formations with normal pore pressures, as illustrated in (Fig. 1.4), the following general relationship of the normal compaction trend of the transit time is proposed:

$$\Delta t_n = \Delta t_m + (\Delta t_{ml} - \Delta t_m)\, e^{-cZ} \quad (1.16)$$

where Δt_m is the compressional transit time in the shale matrix (with zero porosity); Δt_{ml} is the mudline transit time; and c is the costant.

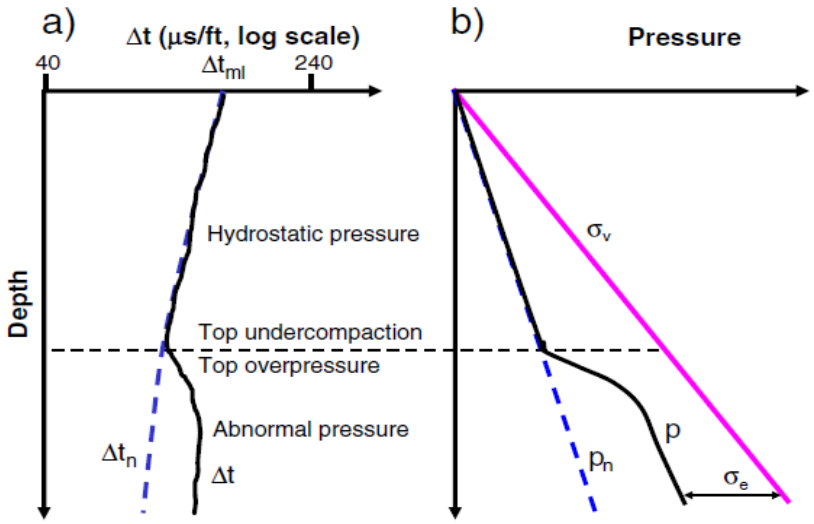

Fig. 1.4. Schematic plots showing sonic transit time (Δt) measured in shale, the normal compaction trend of the transit time in the normal pressure condition (Δt_n) and the pore pressure response to the transit time (Δt), (Figure from Zhang, 2011].

As introduced before, the under-compaction is the primary reason to cause formation overpressured, which occur primarily in rapidly subsiding basins and in rocks with low permeability. The indicators of under-compaction are higher pore pressure and larger formation porosity than those in the normal compaction condition. It is commonly accepted that porosity decreases exponentially as depth increases in normally compacted formations [Athy, 1930]:

$$\phi = \phi_0 e^{-cZ} \tag{1.16}$$

where ϕ is porosity; ϕ_0 is the porosity in the mudline; Z is the true vertical depth below the mudline; c is the compaction constant in 1/m or 1/ft.

As discussed previously, porosity is an indicator (a function) of effective stress and pore pressure, particularly for the overpressures generated from under-compaction and hydrocarbon cracking. Therefore, pore pressure can be estimated from formation porosity. Fig. 1.5 illustrates how to identify under-compaction and overpressure from porosity

profile. When the porosity is reversal, the under-compaction occurs and overpressure generates. The starting point of the porosity reversali s the top of under-compaction or top of overpressure. In the formation with under-compaction, porosity and pore pressure are higher than those in the normally compacted one.

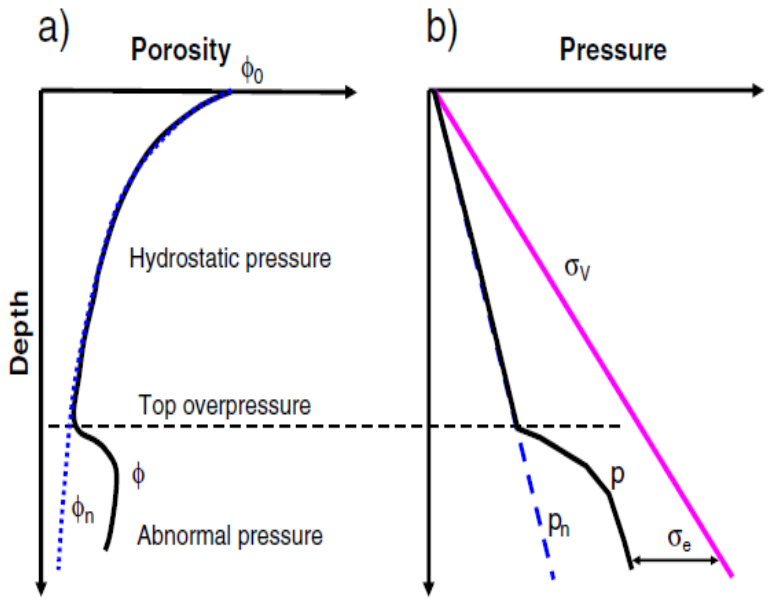

Fig. 1.5. Schematic porosity (a) and corresponding pore pressure (b) in a sedimentary basin. The dash porosity in (a) represents normally compacted formation. In the overpressured section the porosity reversal occurs (heavy line). In the overpressured section, porosity is larger than that in the normal compaction trendline (ϕ_n), (Figure from Zhang, 2011).

1.4 Seismic velocity for overpressure analysis

Seismic data acquisition with multifold coverage is done in shot-receiver (s, g) coordinates. Figure 1.6a is a schematic depiction of the recording geometry and ray paths associated with a flat reflector. Seismic data processing, on the other hand, conventionally is done in midpoint-offset (y, h) coordinates. The required coordinate transformation is achieved by sorting the data into CMP gathers. Based on the field geometry information, each individual trace is assigned to the midpoint between the shot and receiver locations associated with that trace. Those traces with the same midpoint location are grouped together, making up a CMP gather. Albeit incorrectly, the term common depth point (CDP) and common midpoint (CMP) often are used interchangeably. Figure 1.6b depicts

the geometry of a CMP gather and raypaths associated with a flat reflector. Note that CDP gather is equivalent to a CMP gather only when reflectors are horizontal and velocities do not vary horizontally. However, when there are dipping reflectors in the subsurface, these two gathers are note quivalent and only the term CMP gather should be used. The dotted area represents the coverage used in recording the seismic profile along the midpoint axis, Oy. Each dot represents a seismic trace with the time axis perpendicular to the plane of paper. The following gather types are identified in:

(1) Common-shot gather (shot record, field record),

(2) Common-receiver gather,

(3) Common-midpoint gather (CMP gather, CDP gather),

(4) Common-offset section (constant-offset section),

(5) CMP-stacked section (zero-offset section).

For most recording geometries, the fold of coverage nf for CMP stacking is given by

$$nf = \frac{ng\ \Delta g}{2\ \Delta s} \tag{1.17}$$

where Δg and Δs are the receiver-group and shot intervals, respectively, and ng is the number of recording channels. By using this relationship, the following rules can be established:

(a) The fold does not change when alternating traces in each shot record are dropped.

(b) The fold is halved when every other shot record is skipped, whether or not alternating traces in each record are dropped.

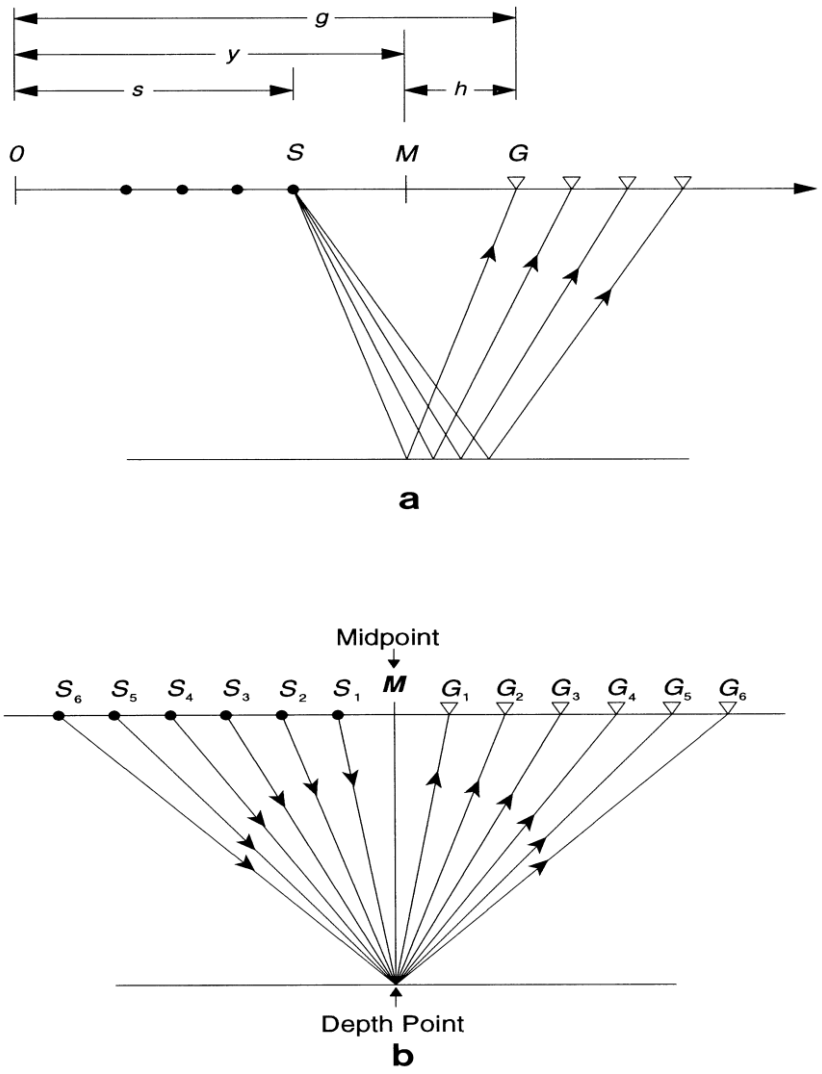

FIG. 1.6. (a) Seismic data acquisition is done in shot-receiver (s, g) coordinates. The raypaths are associated with a planar horizontal reflector from a shot point (indicated by the solid circles) to several receiver locations (indicated by the triangles). The processing coordinates, midpoint-(half) offset, (y, h) are defined in terms of (s, g): $y = (g + s)/2$, $h = (g - s)/2$. The shot axis here points opposite the profiling direction, which is to the left. On a flat reflector, the subsurface is sampled by reflection points which span a length that is equal to half the cable length. (b) Seismic data processing is done in midpoint-offset (y, h) coordinates. The raypaths are associated with a single CMP gather at midpoint location M. A CMP gather is identical to a CDP gather if the depth point were on a horizontally flat reflector and if the medium above were horizontally layered (Figure from Yilmaz, 1987).

All seismic methods for pressure prediction use a relation between the rock velocity and the effective pressure. The rock velocities provides information for both pore pressure and

effective pressure. The rock velocity is described how the acustic wave velocity throught a rock sample [Dutta, 2001].

The seismic method detects changes of interval velocity with depth from velocity analysis of the seismic data. These changes are in turn related to lithology, pore fluid type, rock fracturing and pressure changes within a stratigraphic column. When the factors affecting the velocity are understood for a given area, a successful pressure prediction can be made. In general, the interval velocity of the rocks increases with depth because of compaction. In areas deviations from normal compaction trends are related to abnormally high pore pressures. The seismic velocity versus depth is translated into pore pressure gradient versus depth in any place where seismic velocity analysis has been performed. In seismology we are concerned with the speed of propagation of a seismic wave in the earth. The seismic velocity, therefore, refers to the speed of wavefront in the direction of energy propagation (perpendicular to the wavefront for isotropic earth). Unfortunately, we cannot directly measure the seismic velocity using reflection seismic data. We must measure normal moveout (NMO) velocity, interpret root means square (RMS) velocity from NMO velocity and then convert RMS velocity to interval velocity. Interval velocities thus derived are our best estimate of the velocity of rocks required for overpressure prediction. In the reflection method the two primary measurements we can make for estimating velocity are distance between the shot and receiver and the travel time from the shot to the receiver. In the order to exploit these measurements effectively, the common midpoint (CMP) method is used. This method provides multiple measurements of source-to-reveiver distance (offset) and time for any given interface in the subsurface. As shown in Fig. 1.6, the CMP method consists of recording a number of seismic traces for which the midpoint between the source and reveiver are the same surface location. Each trace has a different offset distance. The group of traces which have a common midpoint is called a CMP gather. When the traces are assembled so that the offset distance progressively increases, the arrival time for a given reflection also increases. These velocities are obtained from an analysis of the traveltime equation valid for the horizontally stratifield earth model, assuming that the offset is small compared to the depth (small spread approximation). In this case, the series coefficient can be truncated as follows:

$$T^2(x) = T^2(0) + \frac{x^2}{V^2 RMS} \tag{1.18}$$

This may be compared with the well known NMO equations:

$$T^2(x) = T^2(0) + \frac{x^2}{V^2 NMO.} \tag{1.19}$$

Comparing equation (1.19) with equation (1.18), we realize that the velocity required for NMO correction for a horizontally stratiefied medium is equal to the *RMS* velocity, provided the small-spread approximation is made. The hyperbolic moveout velocity should be distinguished from the stacking velocity that optimally allows stacking of traces in CMP gather. The hyperbolic form is used to define the best stacking path:

$$T^2{}_{st}(x) = T^2(0) + \frac{x^2}{V^2 st}, \tag{1.20}$$

where V_{st} is the velocity that allows the best fit of the traveltime curve on a CMP gather to a hyperbola within the spread lenght. This hyperbola is not necessarily the small-spread hyperbola implied by either equation (1.18) or equation (1.19). The differences can be significant as shown in figure (1.7).

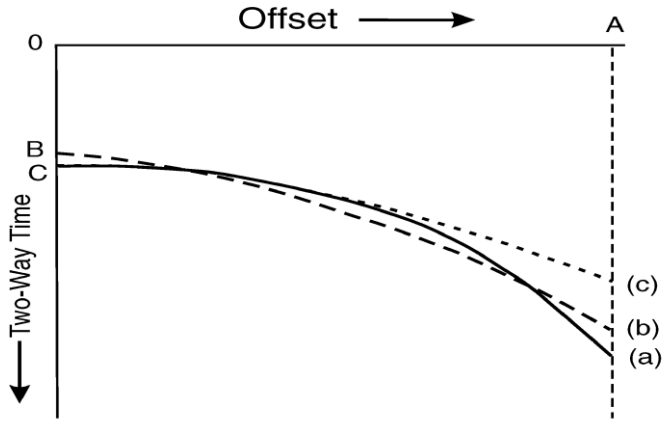

Fig. 1.7. Errors associated with NMO assumptions. The NMO approximation assumes a small-spread hyperbola. The stacking velocity is derived from the best-fit hyperbola over the entire offset range. Here, (a) is the actual traveltime, (b) is the best-fit hyperbola over the full offset range 0A, and (c) is the small-spread hyperbola (Figure from Dutta, 2002).

In this figure, label (a) denotes the actual traveltime, (b) denotes the best-fit hyperbola over the full offset range, and (c) is the small-spread hyperbola. The difference between the stacking velocity, *Vst*, and the NMO velocity, V_{NMO}, is called the spread-lenght bias and should be accounted for any velocity analysis. The equation (1.20) contains the basis for velocity analysis for a CMP gather. This describes a straight line on the t^2 versus x^2 plane. The slope of the line is $1/V^2_{st}$, and the intercept value at $x = 0$ is $t\,(0)$. In practise, a least- squares method is used to do the curve fitting. The traditional form of the Dix's interval velocity equatin for the N th layer in terms of the rms velocities and travel times (valid horizontal layers) is

$$VN = \frac{\sqrt{V^2 rms,N^{tN} - V^2 rms,N-1^{tN-1}}}{tN - tN-1} \tag{1.21}$$

where VN is the interval velocity of the $N\,th$ layer, $V_{rms,\,N}$ is the rms velocity of the $N\,th$ layer and tN is the traveltime to the $N\,th$ layer. Considering costant velocity for every layer, for this reason we consider a velocity smoothing. Velocity smoothing (and interpolation) is an essential step in conditioning velocities for pore pressure prediction work. This oprerations have the attempt to close from the velocity obtained to real; and to reduce the mistakes due inversion from the interval velocity. The last operation, we have to convert from time to depth domain. With all these operations we can start from the V_{RMS}, and obtain a velocity that can be consider an approximation of the real. These operations are obligated and they can introduce mishakes and approximations with a less reliable estimate of pressures.

1.5 Relationship between Poisson's ratio (Vp/Vs) and overpressure

Laboratory investigations suggest that a precise relationship exists between Poisson's ratio, pore pressure and fluid type. Values of Poisson's ratio (Vp/Vs) for dry samples are significantly smaller than those for fluid-saturated samples. The values are anomalously high for high pore pressure, with the possibility of differentiating between gas saturated,

brine-saturated and oil saturated porous rocks. High pore pressures reduce the total effective pressure acting on the framework of the sediment in both consolidated and unconsolidated formations. However, the amount of effective pressure reduction due to increased pore pressure depends on the state of the formation. In unconsolidated sediments, pore pressure reduces the overburden pressure, so that the total effective pressure. As a consequence, the frame is softened and, in extreme conditions of very high pore pressure (low effective pressure), the formation approaches a state of suspension. Since P-wave velocity in a suspension is close to that of the suspending fluid (usually water) and S-waves cannot propagate in suspensions, theVp/Vs ratio or Poisson's ratio must dramatically increase as a sediment passes through the transition zone from load bearing to a suspension. Thus, at low effective pressures when the sediment approaches critical porosity and starts to loose its shear strenght, Vp/Vs ratio shows large changes and can be used to predict overpressured zones. Figure 1.8 shows a plot of Poisson's ratio versus effective stress based on the data from Stanford Rock Physics laboratory for two cases: sand filled with water and sand filled with gas. Note the behavior of Poisson's ratio at low effective stress. For the water filled case, the ratio increases with increases pressure (lowering effective stress), whereas the opposite is true for the gas-filled case. The increse of the saturated-rock Poisson's ratio with increasing pore pressure has a physical basis. The higher the pore pressure, the softer the rock and the larger the relative increase in the bulk modulus between dry and water-saturated samples. With the shear modulus being the same for dry and saturated rock [Gassmann, 1951], Poisson's ratio is larger in the saturated than in the dry sample, especially in soft rocks. An example of saturated-rock Poisson's ratio increasing with decreasing differential pressure is given in Figura 2A (mettere il numero della figura giusto). However, one may observe the opposite effect as well Figura (2b). The direction of the saturated-rock Poisson's ratio change depends on the porosity and elastic moduli of the sample and has to be calibrated by using fluid substitution with site-specif rock data.

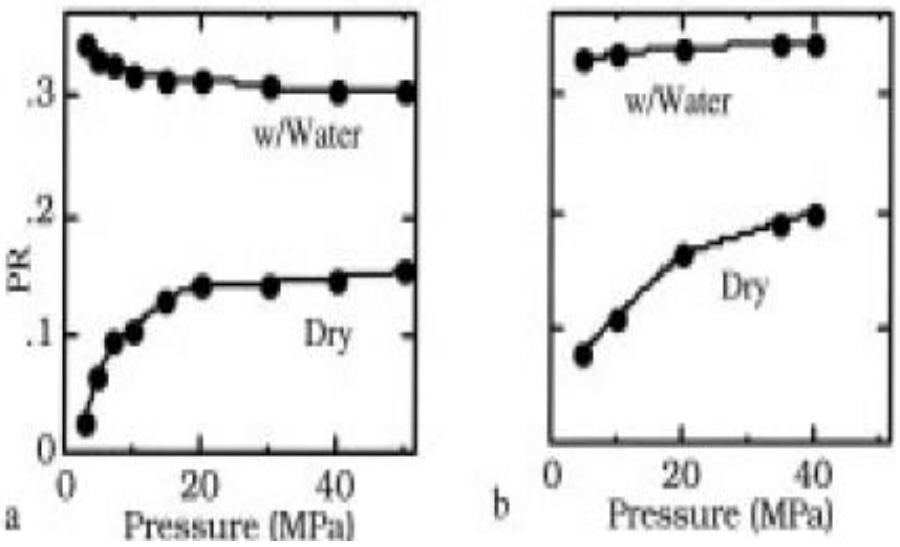

Figure 1.8. Poisson's ratio and water-saturated samples versus differential pressure (Figure from Prasad, 2002).

Decreasing Poisson's ratio with increasing pore pressure in rocks with gas can be used as a physical basis for more reliable pore pressure and pore fluid monitoring and overpressure detection.

Chapter 2

Amplitude Versus Angle

Having a relationship between Poisson's ratio and overpressure (as shown in the first chapter), a fundamental question one must ask is: how can estimate the Vp/Vs ratio? A metodology is AVA analysis. This chapter provides general information about the AVA theory. It indroduces the AVA interpretations may be facilitated by crossplotting AVA Intercept (A) and Gradient (B). Seismic AVA crossplotting can be a diagnostic tool for classifying AVA response, and for identyfyng hydrocarbon deposit and anomaly caused by overpressure phenomens.

2.1 Introduction to AVA analysis

Seismic amplitude-versus angle (AVA) analysis has been a powerful geophysical method in aiding the direct detection of overpressures from seismic records. This method of seismic reflection data is widely used to infer the presence of overpressure and hydrocarbon. The main thrust of AVA analysis is to obtain subsurface rock properties using conventional surface seismic data. The Poisson‟s ratio change across an interface has been of particular interest. These rock properties can then assist in determining lithology, fluid saturants, and porosity. It has been shown through solution of the Zoeppritz equations that the energy reflected from an elastic boundary varies with the angle of incidence of the incident wave. This behavior was studied further by Koefoed (1962). He established in 1955 that, the change in reflection coefficient with the incident angle is dependent on the Poisson's ratio difference across an elastic boundary. Poisson's ratio is defined as the ratio of transverse strain to longitudinal strain [Sheriff, 1973], and is related to the P-wave and S-wave velocities and density. The Poisson's ratio σ has a physical definition described by the formula :

$$\sigma = \frac{\left(\frac{Vp}{Vs}\right)^2 - 1}{2\left(\frac{Vp}{Vs}\right)^2 - 1} \qquad (2.1)$$

It varies in function of *Vp* and *Vs* :

$$Vp = \frac{\sqrt{K + \frac{4}{3}\mu}}{\sqrt{\rho}} \tag{2.2}$$

$$Vs = \frac{\sqrt{\mu}}{\sqrt{\rho}} \tag{2.3}$$

That in turn are dependent on three fundamental parameters that describe a material :

K = Bulk modulus
μ = Share modulus
ρ = density

The Bulk Modulus represents the parameter that is more influenced by the saturation changes (gas or brine). In presence of brine saturated sediments its value become bigger because brine is stiffer than gas; so the Poisson's ratio will decrease in presence of gas and in turn the Vp too. Vs slightly increase with gas saturation because it reduces the density of the material.

AVA is used as a method of detecting overpressure. The variation in amplitude can be fitted in this form of function ($amp = A + B\sin^2\theta$), where A is the intercept of AVA, B is the AVA gradient and θ is the angel of incidence. In practical world, both the estimated intercept and the gradient volumes are used in locating gas fields and other anomalies [Rutherford, 1989]. Seismic traces-recordings of transmitted and reflected sound are sorted into pairs of source-receiver combinations that have different offsets but share a common reflection point midway between each source-receiver pair. This collection of traces is referred to as a common midpoint (CMP) gather. In geophysics, amplitude versus angle (AVA) is a variation in seismic reflection amplitude with change in distance between shot point and receiver that indicates differences in lithology and fluid content in

rocks above and below the reflector. AVA studies are being done on CMP data, the offset increases with the angle. An AVA anomaly is most commonly expressed as increasing (rising) AVA in a sedimentary section, often where the hydrocarbon reservoir is "softer" (lower acoustic impedance) than the surrounding shale. Typically amplitude decreases (falls) with offset due to geometrical spreading, attenuation and other factors. An AVA anomaly can also include examples where amplitude with offset falls at a lower rate than the surrounding reflective events [Schlumberger Oilfield Glossary]. AVA analysis lies in the dependence of the offset-dependent-reflectivity of reflected compressional waves on the elastic properties of the subsurface. As different lithologies may exhibit distinct Poisson's ratios and gas bearing strata usually exhibit anomalously low Poisson's ratios. AVA has been recognized as a potential seismic lithology tool and direct hydrocarbon and overpressure indicator.

2.2 Theory

In exploration geophysics, we rarely deal with simple isolated interfaces. However, we must begin our understanding of offset-dependent reflectivity with the partitioning of energy at just such an interface [Castagna , 1993]. In Figure (2.1), the angles for incident, reflected and transmitted rays synchronous at the boundary are related according to Snell's law by:

$$P = \frac{sin\theta 1}{Vp1} = \frac{sin\theta 2}{Vp2} = \frac{sin\theta 1}{Vs1} = \frac{sin\theta 2}{Vs2} \qquad (2.4)$$

Where $Vp1$ = P- wave velocity in medium 1, $Vp2$ = P- wave velocity in medium 2; $Vs1$ = S- wave velocity in medium 1; $Vs2$ = S-wave velocity in medium 2; $\theta 1$ = incident P-wave angle, $\theta 2$ = trasmitted P-wave angle; $\acute{\emptyset}1$ = reflected S-wave angle, $\acute{\emptyset}2$ = transmitted S-wave angle, and P is the ray parameter.

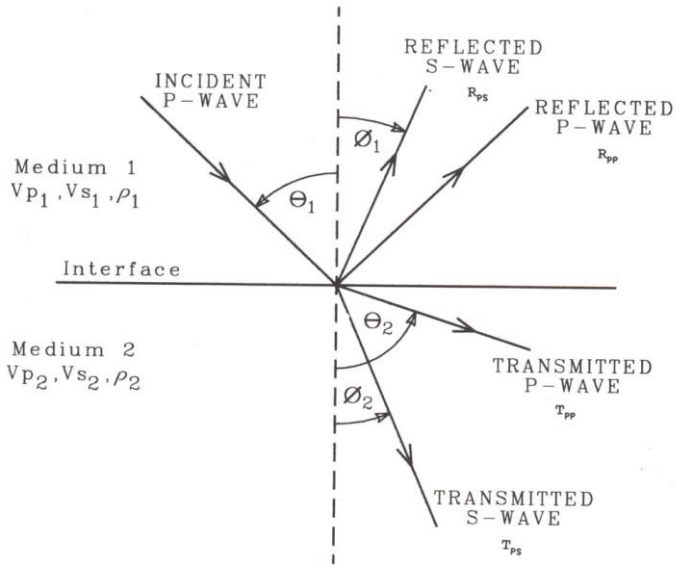

FIG. 2.1. Reflection and transmission at an interface between two infinite elastic half-spaces for an incident P-wave (Figure from Castagna and Backus, 1993).

Seismic reflectivity and reflection amplitudes were first calculated by Karl Bernhard Zoeppritz (1919). Zoeprittz equations calculate the amplitudes of reflected and refracted P waves at an interface. The seismic amplitude is a function of incidence angle and some elastic properties. Because it is difficult to understand the algebra of the equations, geophysicists have used approximations instead. Before Zoeprittz, Cargill Gilston Knott's equations were proposed to find partitioning seismic wave energy. Reflection coefficients can be analyzed as a function of angle with Aki & Richard's (1980) approximation:

$$R_{pp}(\theta) \approx \frac{1}{2}\left(1 - 4p^2Vs^2\right)\left(\frac{\Delta\rho}{\rho}\right) + \frac{1}{2cos^2(\theta)}\frac{\Delta Vp}{Vp} - 4Vs^2\rho^2\frac{\Delta Vs}{Vs} \qquad (2.5)$$

Where ΔVp is the change in compressional velocity across the interface ($Vp_2 - Vp_1$), Vp is the average compressional velocity across the interface [($Vp_2 - Vp_1$)/2], $\Delta\rho$ is the change in density across the interface ($\rho_2 - \rho_1$), ρ is the average density across the interface, ΔVs is the change in shear velocity across the interface ($Vs_2 - Vs_1$), Vs is the average shear velocity across the interface [($Vs_2 - Vs_1$)/2], with Vp_1, Vs_1, ρ_1 and Vp_2, Vs_1,

ρ_2 being the medium properties in the first (overlying) and second (underlying) media, respectively.

By simplifying the Zoeppritz equations, Shuey (1985) presented another form of the Aki and Richards (1980) approximation:

$$R(\theta) \approx Ro + G\sin^2\theta + [\tan^2\theta - \sin^2\theta] \tag{2.6}$$

$$G = \frac{1}{2} + \frac{\Delta Vp}{Vp} - 2\frac{Vs^2}{Vp^2}\left(\frac{\Delta\rho}{\rho} + 2\frac{\Delta Vs}{Vs}\right) \tag{2.7}$$

$$G = R(0) - \frac{\Delta\rho}{\rho} - \left(\frac{1}{2} + 2\frac{Vs^2}{Vp^2}\right) - 4\frac{Vs^2}{Vp^2}\frac{\Delta Vs}{Vs}$$

$$F = \frac{1}{2}\frac{\Delta Vp}{Vp} \tag{2.8}$$

$R(\theta)$ form can be interpreted in terms of different angular ranges. Ro is the normal-incidence reflection coefficient. G is the gradient and describes the variation in the intermediate offsets. F dominates the far offsets near the critical angle. For incidence angles less than 30°, this can be reduced to:

$$R(\theta) \approx Ro + G\sin^2\theta \tag{2.9}$$

The knowledge of these two parameters enable us to identify and classify the presence of a fluid saturation within an horizon that exhibits anomalous amplitude values in the seismic data. In my study, *Shuey's approximation* (1985) was used for cross plotting data.

2.3 AVA behavior for gas sands

In a clastic sequence, a typical top reservoir is represented by the interface between shale and an hydrocarbon-saturated sand. The AVA analysis proposed by Ostrander (1984) was applied in presence of amplitude anomalies produced by gas sands that have lower impedance of the encasing shale and an increasing amplitude with offset. Appling the equation (2.9) to this situation, the intercept value Ro, measured at zero offset, and the reflecting coefficients, measured at different angles of incidence, will have negative values; also the measured gradient G will have a negative value. Then, both negative values of G and Ro describe the most general situation of the AVA behavior of a reflector produced by a gas sand covered by a shale. Its seismic evidence is depicted by the classical bright spot. Unfortunately, gas presence is not always evidenced by a bright spot and gas sands could manifest different AVA characteristics.

AVA responses have been discriminated by Rutherford and Williams (1989) into 3 classes in function of the values of Ro and G as defined by equation (2.9).

Figure (2.2) shows the Zoeppritz's P-wave reflection coefficients for a shale-gas sand interface for a range of values of Ro. The Poisson's ratio and density of the shale were assumed, by Rutherford and Williams (1989), to be 0.38 and 2.4 g/cm^3, and for the gas sand to be 0.15 and 2.0 g/cm^3, respectively.

Class 1 response (blue line) is characterized by an increase in impedance downwards across the interface, causing a decreasing amplitude with increasing incident angles; the magnitude of reflectivity can change polarity with adequate offset/angle rate. The polarity change, if pronounced, might cancel out the reflection response from the stacked section or can produce polarity opposite to that predicted by normal incidence modeling.

Class 2 response (green lines) has nearly the same impedance of the encasing material and small normal incidence amplitude (positive or negative), but the AVA leads to high negative amplitudes at far offsets. The polarity change occurs if Ro is positive but it is not usually detectable because this happens at small offset where the signal is often below the overall noise level. Class 3 response (red line) has large negative impedance contrast and the negative gradient leads to increasing amplitude with angles; such sands are usually

unconsolidated and undercompacted, producing amplitude anomalies on the stacked profile and large reflectivity along the offset.

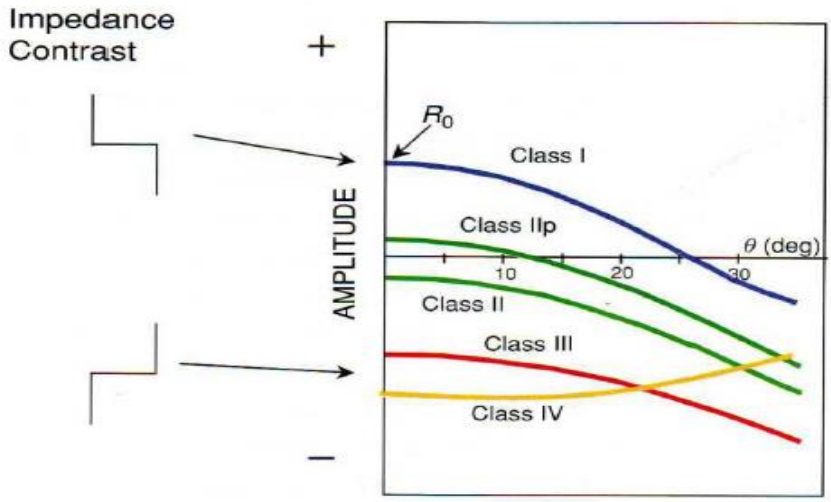

Figure 2.2 AVO sand classes of Rutherford and Williams (1989) and Castagna and Swan (1997) in a model originally based on shale/brine sand interface (Figure from Bacon, 2009).

Castagna and Swan (1997) introduced a Class 4 gas sand (yellow line) representing low impedance gas sands for which the reflection coefficients decrease with increasing offset, in particular when the shear wave velocity of the gas sand is lower than in the shale. In a clastic sequence, the AVA classes are related to differences of consolidation of sand and shales with depth. The general increase in impedance with depth reflects the decrease in porosity due to compaction. Class 1 results are characteristic of deep well consolidate sediments and class 3 responses, as said before, of relatively unconsolidated and shallow sediments. Class 4 may occur in very unconsolidates and very shallow (up to 1000m) sands, or when they are covered by an hard non clastic layer. With respect to class 3, class 4 has very low gradient.

2.4 Crossplot visualization of AVA Gradient and Intercept

Castagna and Swan (1997) used the crossplot representation of the AVA Gradient versus the AVA Intercept to make easier the interpretation of the AVA method. The Intercept

and Gradient can be calculated on every CMP gather in a seismic survey, by measuring the amplitude and the best fit to a plot of $R(\theta)$ as a function of $sin^2(\theta)$. The resulting pairs of Ro and G values may be display in a crossplot graph and they give information about fluid filling, saturation and lithology.

To better understand the Crossplot analysis of AVA, in this section the theoretical analysis of Castagna et al., (1998), will be considered in detail. The Shuey's approximation of the Zoeppritz equation is described by:

$$R(\theta) \approx Ro + G\,sin^2\theta \quad = R(\theta) \approx A + B\,sin^2\theta \tag{2.10}$$

with:

$$A = \frac{1}{2}\left(\frac{\Delta Vp}{<Vp>} + \frac{\Delta \rho}{<\rho>}\right); \tag{2.11}$$

$$B = \frac{1}{2}\,\frac{\Delta Vp}{<Vp>} - 2\left(\frac{<Vs>}{<Vp>}\right)^2\left(2\,\frac{\Delta Vs}{<Vs>} + \frac{\Delta \rho}{<\rho>}\right); \tag{2.12}$$

The crossplot analyzes the variations of the AVA Gradient B as a function of the AVA Intercept A; the correlations between these two parameters can be explained considering the variation of Vp/Vs at an interface, and the values of the density.
Let us start from the basic assumption of the "mudrock line" and the Gardner's equation. Castagna (1985), demonstrated that a succession of brine-saturated sand and shale, defined as "background", follows a specific trend defined as "mudrock" line where a linear relationship between Vp e Vs exists.
Within a fixed depth window the relation is:

$$Vp = mVs + c \tag{2.13}$$

where m and c are empirical coefficients depending by the lithology characteristics. Within the "background", the Gardner's equation asserts that the density is the multiplicationbetween a constant factor a time the velocity V, raised to a power factor g:

$$\rho = aV^{g} \tag{2.14}$$

so

$$\left(\frac{\Delta\rho}{<\rho>} \sim g\frac{\Delta Vp}{<Vp>}\right) \tag{2.15}$$

Gardner (1974), demonstrated that g is close to 0.25 for most of the sedimentary rocks.

$$A = \frac{1}{2}\left(\frac{\Delta Vp}{<Vp>} + \frac{\Delta\rho}{<\rho>}\right) = \frac{1}{2}\frac{\Delta Vp}{<Vp>}\ (1+g) \tag{2.16}$$

$$B = \frac{1}{2}\frac{\Delta Vp}{<Vp>} - 2\left(\frac{<Vs>}{<Vp>}\right)^{2}\left(2\frac{\Delta Vs}{<Vs>} + \frac{\Delta\rho}{<\rho>}\right) = \tag{2.17}$$

$$= \frac{A}{1+g} - 2\left(\frac{<Vs>}{<Vp>}\right)^{2}\left(2\frac{\Delta Vs}{m<Vs>} + + g\frac{\Delta Vp}{<Vp>}\right) \tag{2.18}$$

If $\Delta Vp = \frac{2\,A<Vp>}{1+g}$ (2.19)

,then

$$B = \frac{A}{1+g} - 2\left(\frac{<Vs>}{<Vp>}\right)^{2}\left(2\frac{2A\Delta Vp}{(1+g)m<Vs>} + g\frac{2A}{1+g}\right) =$$

$$= \frac{A}{1+g} - \frac{4A}{1+g}\left[\frac{<Vs>^{2}}{<Vp>^{2}}\left(2\frac{<Vp>}{m<Vs>} + g\right)\right] =$$

$$= \frac{A}{1+g}\left[1 - 4\frac{<Vs>}{<Vp>}\left(\frac{2}{m} + g\frac{<Vs>}{<Vp>}\right)\right] \tag{2.20}$$

The equation (2.20) represents the general equation for the background reflection in the *A-B* plane. Starting from this general relation, 2 specific relation between *Vp, Vs* and ρ can be considered.

1) Costant Vp/Vs and costant density

If *Vp/Vs* is costant, *c* must vanish and, from Gardner's relation

$$m = Vp/Vs = < Vp > / < Vs > = \frac{\Delta Vp}{\Delta Vs} \tag{2.21}$$

Assuming $\Delta\rho = 0$ (costant ρ values) in the equation (2.16) and substituting $g = 0$

$$A = \frac{1}{2}\left(\frac{\Delta Vp}{<Vp>}\right) \tag{2.22}$$

$$B = \left[1 - 8\left(\frac{<Vs>}{<Vp>}\right)^2\right] A \tag{2.23}$$

2) Costant Vp/Vs and Gardner's density

For limited depth ranges we can assume the Gardner's value of $g = ¼$.

$$m = < Vp > / < Vs > (costant\ Vp/Vs) \tag{2.24}$$

$$A = \frac{5}{8}\left(\frac{\Delta Vp}{<Vp>}\right) \tag{2.25}$$

$$B = \frac{4}{5}\left[1 - 9\left(\frac{<Vs>}{<Vp>}\right)^2\right] A \tag{2.26}$$

This last equation shows that all the lines cross the origin and that the slope of the background trend depends only by $< Vp > / < Vs >$ (figure 2.3a).

With increasing of $< Vp > / < Vs >$ the slope becomes more positive and the line rotates counterclockwise.
If $< Vp > / < Vs > = 2$, then $B = -A$, irrespective of the density and velocity relantionship.

From this relationship, we observe that the background trend passes through the origin and, as $< Vp >$ decreases, the background becomes more positive (rotates counterclockwise). In the Figure 2.3b (where $m = 1.16$ and $c = 1.36k\ km/s$ from Castagna, 1985) the background trend changes dramatically for velocities lower than about 2.5 km/s. These conclusions are similar for costant $< Vp > / < Vs >$, but we have to consider that along an interface, this ratio varies rather than remaining costant and this will produce different slopes for the bacground trend.

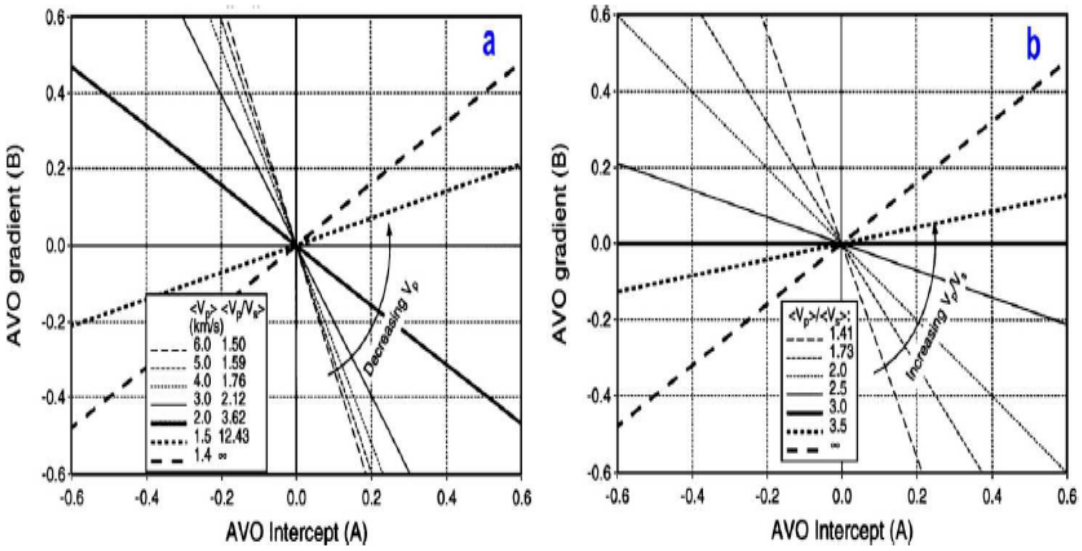

Figure 2.3: background trend with *VP/VS* constant and Gardner's relation; b: background trend with linear *VP/VS* and $m = 1.16$ and $c = 1.36 km/s$ (from Castagna, 1998).

Comparing the results of the different case analysis (Figure 2.4), we observe that the *B/A* trend is more affected by the variation of $< Vp > / < Vs >$ than by the variation of density: constant and linear relation between the two velocities gives very different

background trends. Moreover, for all the examined cases *B/A* increases with increasing $< Vp > / < Vs >$. Thus, if the depth range selected is too large, the $< Vp > / < Vs >$ background varies significantly (due to compaction) and several background trends may be superimposed. Also, for very high $< Vp > / < Vs >$, as for soft and shallow brine-saturated sediments , the background trend *B/A* becomes more positive and even non hydrocarbon-related reflection may exhibit increasing AVA, depicting false positive anomalies.

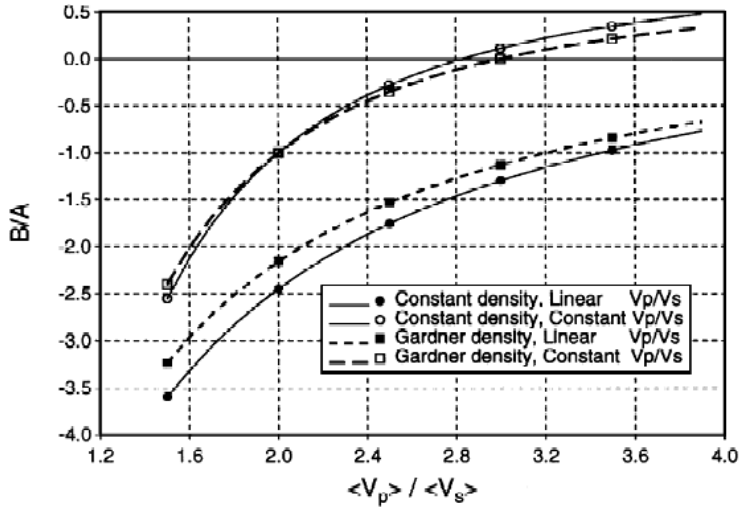

Figure 2.4. *B/A* versus *<VP >/<VS>* for various background trend assumptions: constant *VP/VS* and constant density, constant *VP/VS* and Gardner density, mudrock *VP* versus *VS* and constant density, mudrock *VP* versus *VS* and Gardner density. In all cases, *B/A* increases with increasing background *<VP>/<VS>* (Figure from Castagna, 1998).

The rotation of the line gives evidence that the background trend is also an implicit function of rock physic properties such as clay content and porosity. Increasing the clay content at a reservoir level will cause a counterclockwise rotation, as the $< Vp > / < Vs >$ increases. Increasing porosity related to less compaction will also cause a counterclockwise rotation, because less-compacted sediments tend to have relatively high $< Vp > / < Vs >$.

2.5 Deviations from petrophysical relationship

The AVA analysis studies the interpretation of magnitude of the deviation from the background trend, once introduced hydrocarbons in the clastic sequence. The most interesting deviation from background petrophysical relationship results, in fact, from replacement of brine by gas in the pore spaces: it reduces the $<Vp>/<Vs>$ and causes ΔVp and $\Delta\rho$ to become more negative. Thus, the equations (2.11) and (2.12) for a top of sand reflection, with partial gas saturation, causes both A and B to become more negative than for a fully brine saturated sand. Figure (2.5) well explains the difference of the calculated AVA Gradient and Intercept between pairs of shale/gas sands and shale/brine sands reflectors. For a shale over the brine-sand, reflection coefficients vary from strong positive to strong negative values. The Intercept and the Gradient lie along the straight line predicted using the linear relationship between $<Vp>$ and $<Vp>$ crossing the origin (blue line). With the introduction of gas fluids and calculating the effects of the variation bulk modulus with the Gassmann's equations, we observe that the reflecting coefficients also fall along a straight line but they lie to the lower left of the background trend (green line). This line moves towards negative values of A and B from brine to gas sand.

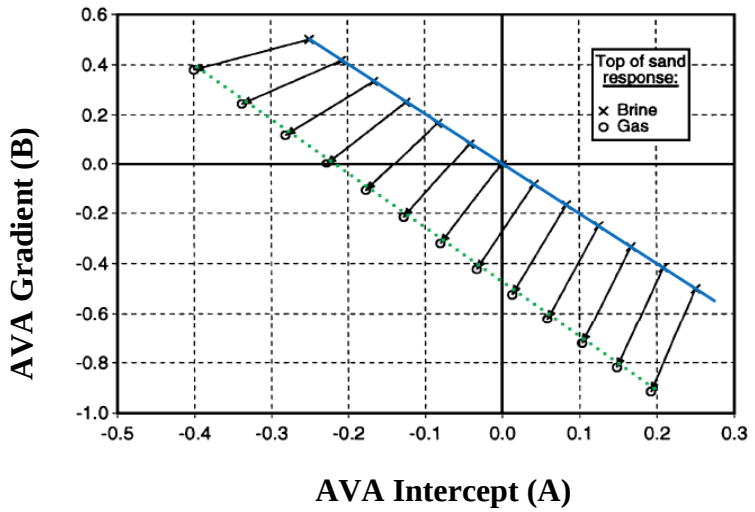

Figure 2.5. Brine sand–gas sand tie lines for shale over brine-sand reflections having an average *P*-wave velocity of 3 km/s and which conform to Gardner and mudrock petrophysical trend curves (g = 0,25, m = 1,16, c =1,36 km/s) and Gassmann's equations (Figure from Castagna, 1998).

The measure of the deviation from the line of background trend was introduced by Smith and Gidlow (1987) by calculating the parameter called “Fluid Factor”:

$$\Delta F = \left[\left(\frac{\Delta Vp}{<Vp>} - m \frac{<Vs>}{<Vs>} \frac{\Delta Vs}{<Vs>} \right) \right] \quad (2.26)$$

The gas sand classification of Rutherford and Williams (1989) was based only on normal incidence reflection coefficient ($R_P = A$); all the 3 classes exhibit a reflection coefficients to become more negative with increasing offset, but the reflection coefficients need not to increase with offset for gas sands. As we can see from Figure (2.5) a gas sand could have coefficients becoming more positive with increasing offsets; thus, introduced a 4th class representing this situation [Castagna and Swan, 1997].

The AVA behavior is well-explained by the crossplot of *A* versus *B*, in which we recognize all the four classes and their collocation inside the crossplot quadrants (Figure 2.6).

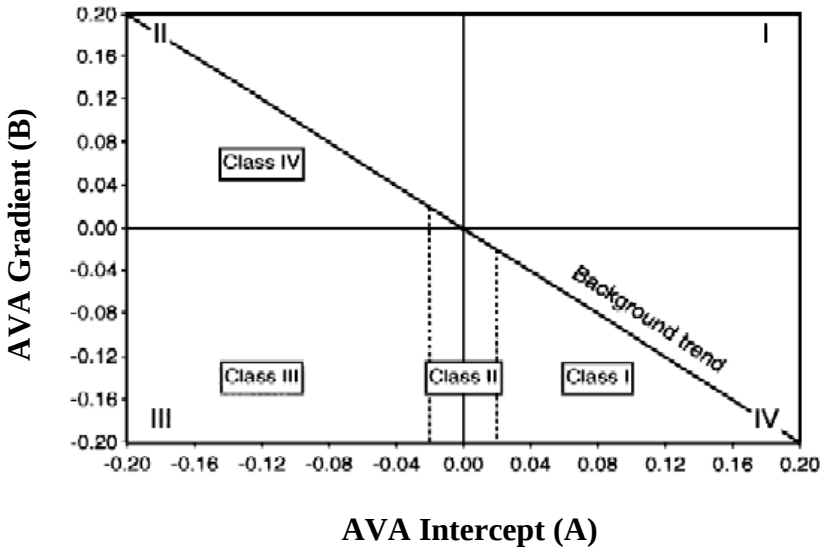

Figure 2.6. AVA Gradient *(B)* versus Intercept *(A)* crossplot showing four possible quadrants. For a limited time window, brine-saturated sandstones and shales tend to fall along a well-defined background trend. Top of gas-sand reflection tend to fall below the background trend, whereas bottom of gas-sand reflections tend to fall above the trend (from Castagna, 1998).

Chapter 3

Analytical Response

This chapter shows an algorithm has been developed. It consideres an AVA Analytical Response. The AVA Analytical Response well logs of the seismic have been used, and the Intercept and Gradient values extracted from the P-S velocities and density well logs. Shuey's approximation was used for AVA crossplot analysis. Each point in the AVA crossplot is mapped using the amplitude of Intercept (A) and Gradient (B) in a time window. Within this time window, it has calculated the *Singular Value Decomposition* (SVD), and obtained the eingenvector associated with the first singular value that gives the direction of maximum variance. The angle was calculated from the eingenvector that meet with the horizontal, it characterizes the Background Trend (Vp/Vs) was subsequently converted into Vp/Vs ratio value to predict two empirical equations, Costant Density and Gardner Density (as showed the chapter 2). The stability of the Background Trend (Vp/Vs) can have an impact on what is being interpretated as anomalous, be it fluid or lithology induced outliers. It was necessary to study many strategies which make robust and reliable method. To stabilize the estimation of Vp/Vs from the slope of the Background Trend, to do this, proceeded through the operation of outlier removal in Itercept and Gradient domain.

3.1 Linear Least Squares Regression

Linear least squares regression is by far the most widely used modeling method. It plays a strong underlying role in many modeling methods. Used directly, with an appropriate data set, linear least squares regression can be used to fit the data with any function of the form :

$$Y = B_0 + B_1X \tag{3.1}$$

where B_0 is a constant, B_1 is the regression coefficient, X is the value of the independent variable, and Y is the value of the dependent variable.

Given a random sample of observations, the population regression line is estimated by:

$$\hat{y} = b_0 + b_1 x \tag{3.2}$$

$$b_1 = \Sigma [(x_i - x)(y_i - y)] / \Sigma [(x_i - x)^2] \tag{3.3}$$

$$b_1 = r * (s_y / s_x) \tag{3.4}$$

$$b_0 = y - b_1 * x \tag{3.5}$$

where b_0 is the constant in the regression equation, b_1 is the regression coefficient, r is the correlation between x and y, x_i is the X value of observation i, y_i is the Y value of observation i, x is the mean of X, y is the mean of Y, Sx is the standard deviation of X, and Sy is the standard deviation of Y.

When the regression parameters (b_0 and b_1) are defined as described above, the regression line has the following properties:

1)The line minimizes the sum of squared differences between observed values (the y values) and predicted values (the $\hat{y}$ values computed from the regression equation).

2)The regression line passes through the mean of the X values (x) and through the mean of the Yvalues (y).

3)The regression constant (b_0) is equal to the y intercept of the regression line.

4)The regression coefficient (b_1) is the average change in the dependent variable (Y) for a 1-unit change in the independent variable (X). It is the slope of the regression line.

The least squares regression line is the only straight line that has all of these properties.

In statistical terms, any function that meets these criteria would be called a "linear function". The term "linear" is used, even though the function may not be a straight line, because if the unknown parameters are considered to be variables and the explanatory variables are considered to be known coefficients corresponding to those "variables", then

the problem becomes a system (usually overdetermined) of linear equations that can be solved for the values of the unknown parameters. To differentiate the various meanings of the word "linear", the linear models being discussed here are often said to be "linear in the parameters" or "statistically linear". In the least squares method the unknown parameters are estimated by minimizing the sum of the squared deviations between the data and the model. The minimization process reduces the overdetermined system of equations formed by the data to a sensible system of p,(where p is the number of parameters in the functional part of the model) equations in p unknowns. This new system of equations is then solved to obtain the parameter estimates. Linear least squares regression has earned its place as the primary tool for process modeling because of its effectiveness and completeness. Though there are types of data that are better described by functions that are nonlinear in the parameters, many processes in science and engineering are well-described by linear models. This is because either the processes are inherently linear or because, over short ranges, any process can be well-approximated by a linear model. The estimates of the unknown parameters obtained from linear least squares regression are the optimal estimates from a broad class of possible parameter estimates under the usual assumptions used for process modeling. Practically speaking, linear least squares regression makes very efficient use of the data. Good results can be obtained with relatively small data sets. Finally, the theory associated with linear regression is well-understood and allows for construction of different types of easily-interpretable statistical intervals for predictions, calibrations, and optimizations. These statistical intervals can then be used to give clear answers to scientific and engineering questions. The main disadvantages of linear least squares are limitations in the shapes that linear models can assume over long ranges, possibly poor extrapolation properties, and sensitivity to outliers. Linear models with nonlinear terms in the predictor variables curve relatively slowly, so for inherently nonlinear processes it becomes increasingly difficult to find a linear model that fits the data well as the range of the data increases. As the explanatory variables become extreme, the output of the linear model will also always more extreme. This means that linear models may not be effective for extrapolating the results of a process for which data cannot be collected in the region of interest. Of course extrapolation is potentially dangerous regardless of the model type. Finally, while the method of least squares often gives optimal estimates of the unknown parameters, it is very sensitive to the presence of unusual data points in the data used to fit a model. One or two outliers can sometimes seriously skew the results of a least squares analysis.

3.2 Singular Value Decomposition (SVD) Theory

For the solution of sets of linear equations defined by matrices that are either singular or numerically very close to singular a very robust method exists: the so-called singular value decomposition (SVD) method. The decomposition of a matrix is often called a factorization. The decomposition of a matrix is useful when the matrix is not of full rank. That is, the rows or columns of the matrix are linearly dependent. One can use Gaussian elimination to reduce the matrix to row echelon form and then count the number of nonzero rows to determine the rank. However, this approach is not practical when working in finite precision arithmetic.

The SVD represents an expansion of the original data in a coordinate system where the covariance matrix is diagonal. Using the SVD, one can determine the dimension of the matrix range or more-often called the rank. The rank of a matrix is equal to the number of linear independent rows or columns. This is often referred to as a minimum spanning set or simply a basis. The SVD can also quantify the sensitivity of a linear system to numerical error or obtain a matrix inverse. Additionally, it provides solutions to least-squares problems and handles situations when matrices are either singular or numerically very close to singular.

We assume that the number of equations is equal or larger than the number of unknowns, $M \geq N$. Any corresponding $M \times N$ matrix A can be written as the product of an $M \times N$ column-orthogonal matrix U ($UTU = I$), an $N \times N$ diagonal matrix with positive or zero elements, and the transpose of an $N \times N$ orthogonal matrix V ($V^TV=I$), where I is the unitary matrix.

$$A = U \times L \times V^T \tag{3.6}$$

L is a diagonal matrix with non-negative matrix elements having the same dimension as A, $Wi \geq 0$. The diagonal elements of L are the singular values of matrix A.

Calculating the SVD consists of finding the eigenvalues and eigenvectors of AA^T and A^TA. The eigenvectors of A^TA from the columns of V, the eigenvectors of AA^T form the columns of U. Also, the singular values in L are square roots of eigenvalues from AA^T or A^TA. The singular values are the diagonal entries of the L matrix and are arranged in descending order. The singular values are always real numbers. If the matrix A is a real matrix, then U and V are also real. For $M = N$, matrices U and V are square and the inverse matrix of A is

$$A^{-1} = (U\ L\ V^T)^{-1} = (V^T)^{-1}\ L^{-1} U^{-1} = V\ L^{-1} U^T \tag{3.7}$$

where the diagonal elements of L^{-1} are $1/L_i$. The matrices U and V are orthogonal and their inverse matrices are equal to their transposes

$$U^{-1} = U^T \text{ and } V^{-1} = V^T \tag{3.8}$$

If one or more Wi are zero or very close to zero then in this case A is singular. For a system of linear equations,

$$AX = Y \tag{3.9}$$

where A is a square matrix, and X and Y are column matrices, A^{-1} can be used to obtain X:

$$X = A^{-1}Y = VL^*U^TY \tag{3.10}$$

where L* is a diagonal matrix with elements $L^*_i = 1/L_i$ if $L_i \geq \mathbf{e}$, else 0, where **e** is the so-called *singularity threshold*. In other words, if L_i is zero or close to zero (smaller than **e**), one must replace $1/L_i$ with 0. The value of e depends on the precision of the hardware. This method can be used to solve linear equations systems even if the matrices are singular or close to singular.

Additionally an important property is that if there does not exists a solution when the matrix A is singular but replacing $1/L_i$ with 0 will provide a solution that minimizes the residue |AX -Y|. SVD finds the least squares best compromise solution of the linear equation system. Interestingly SVD can be also used in an over-determined system where the number of equations exceeds that of the parameters.

3.3 AVA Methodology

Let it considers two semi-infinite isotropic homogeneous elastic half-spaces in contact at a plane interface. For an incident plane wave, the reflection coefficient variation with angle of incidence is given by the well-known Knott-Zoeppritz equations. For small variations in layer parameters and angles of incidence commonly encountered in seismic reflected applications, these equations can be accurately approximated using in terms of the angular reflection coefficients A, B:

$$R(\theta) \approx A + B\,sin^2\theta \tag{3.11}$$

Where R is the reflection coefficient as a funcition of different angular (θ) ranges. The AVA Analytical Response well logs of the seismic have been used, and the Intercept and Gradient values extracted from the P-S velocities and density well logs, using Shuey's approximation:

$$A = \frac{1}{2}\left(\frac{\Delta Vp}{<Vp>} + \frac{\Delta \rho}{<\rho>}\right); \tag{3.12}$$

$$B = \frac{1}{2}\,\frac{\Delta Vp}{<Vp>} - 2\left(\frac{<Vs>}{<Vp>}\right)^2\left(2\,\frac{\Delta Vs}{<Vs>} + \frac{\Delta \rho}{<\rho>}\right); \tag{3.13}$$

Where ΔVp is the change in compressional velocity across the interface ($Vp_2 - Vp_1$), Vp is the average compressional velocity across the interface [($Vp_2 - Vp_1$)/2], $\Delta\rho$ is the change in density across the interface ($\rho_2 - \rho_1$), ρ is the average density across the interface, ΔVs is the change in shear velocity across the interface ($Vs_2 - Vs_1$), Vs is the average shear velocity across the interface [($Vs_2 - Vs_1$)/2], with Vp_1, Vs_1, ρ_1 and Vp_2, Vs_1, ρ_2 being the medium properties in the first (overlying) and second (underlying) media, respectively. A is the linearized form of the normal-incidence compressional-wave reflection coefficient (Rp). The parameters Vp, Vs, ρ are often highly correlated, with deviations attributable to hydrocarbons or unusual lithologies. These correlations imply relationship between the angular reflection coefficients A and B.

Starting from these general approximations (3.12, 3.13), two specif equations can be considered, Costant Density and Gardner Density. From these equations, it has been able to extract Vp/Vs values, as follows:

1) costant density

$$B = \left[1 - 8\left(\frac{<Vs>}{<Vp>}\right)^2\right] A \tag{3.14}$$

$$\frac{B}{A} = \left[1 - 8\left(\frac{<Vs>}{<Vp>}\right)^2\right] \tag{3.15}$$

$$\frac{B}{\frac{A}{8}} - 1 = -\left(\frac{<Vs>}{<Vp>}\right)^2 \tag{3.16}$$

$$\frac{<Vp>}{<Vs>} = \frac{\sqrt{-8}}{\sqrt{\frac{B}{A} - 1}} \tag{3.17}$$

2) *Gardner density*

$$B = \frac{4}{5}\left[1 - 9\left(\frac{<Vs>}{<Vp>}\right)^2\right] A \tag{3.18}$$

$$\frac{B}{\frac{A}{8}}\left(\frac{4}{5}\right) - 1 = -\left(\frac{<Vs>}{<Vp>}\right)^2 \tag{3.19}$$

$$\frac{<Vp>}{<Vs>} = \frac{\sqrt{-9}}{\sqrt{\left(\frac{5}{4}\right)\frac{B}{A} - 1}} \tag{3.20}$$

Three important logs were considered in this present study, P-S velocities (m/s) and density logs (g/cm^3), they are available from well logging (recording time = 355 ms).

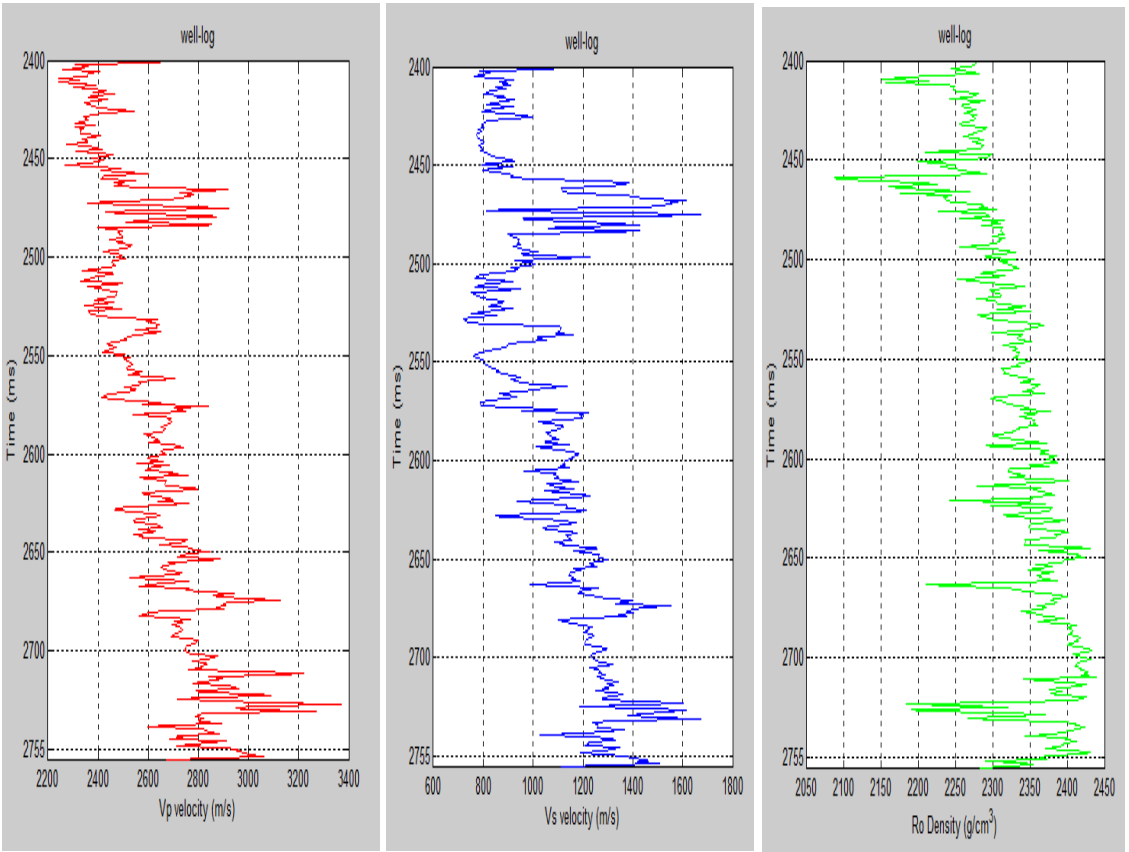

Fig. 3.1. Vp,Vs and Ro well logs.

In the Analytical Response three several examples were evaluated, applying of the time windows of 71 (ms) and 91 (ms).

It begins from the simplest case where the Vp/Vs ratio remains costant throughout the interval described by pseudo logs. In this case, it is clearly noted that the variations of Vp/Vs value, the slope of the Background Trend (and simultaneously that of the interpolating straight line) rotates counterclockwise. To improve the essessment of Vp/Vs from the slope of the Background Trend, it proceeded through the operation of outlier removal in Intercept and Gradient Domain. It considered the distance from the points to a straight line, and it has done a average of the distances from the straight line. Distances over two standard deviation were rimoved, and were considered as outliers. Background Trend rotations observed in AVA crossplot, is a function of time/depth. It has showed several AVA crossplot:

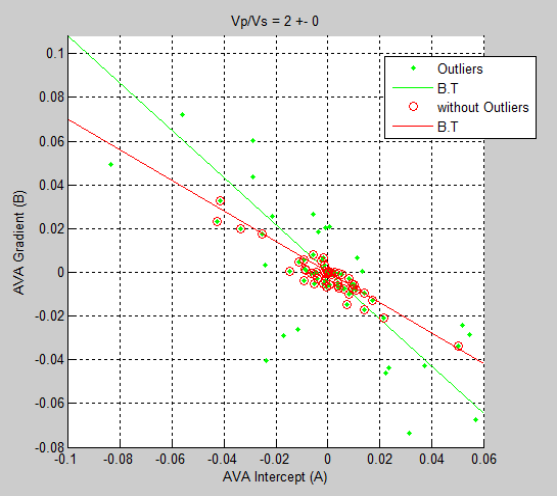

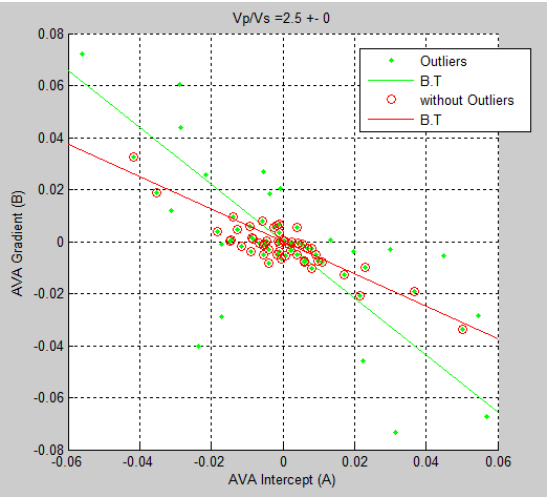

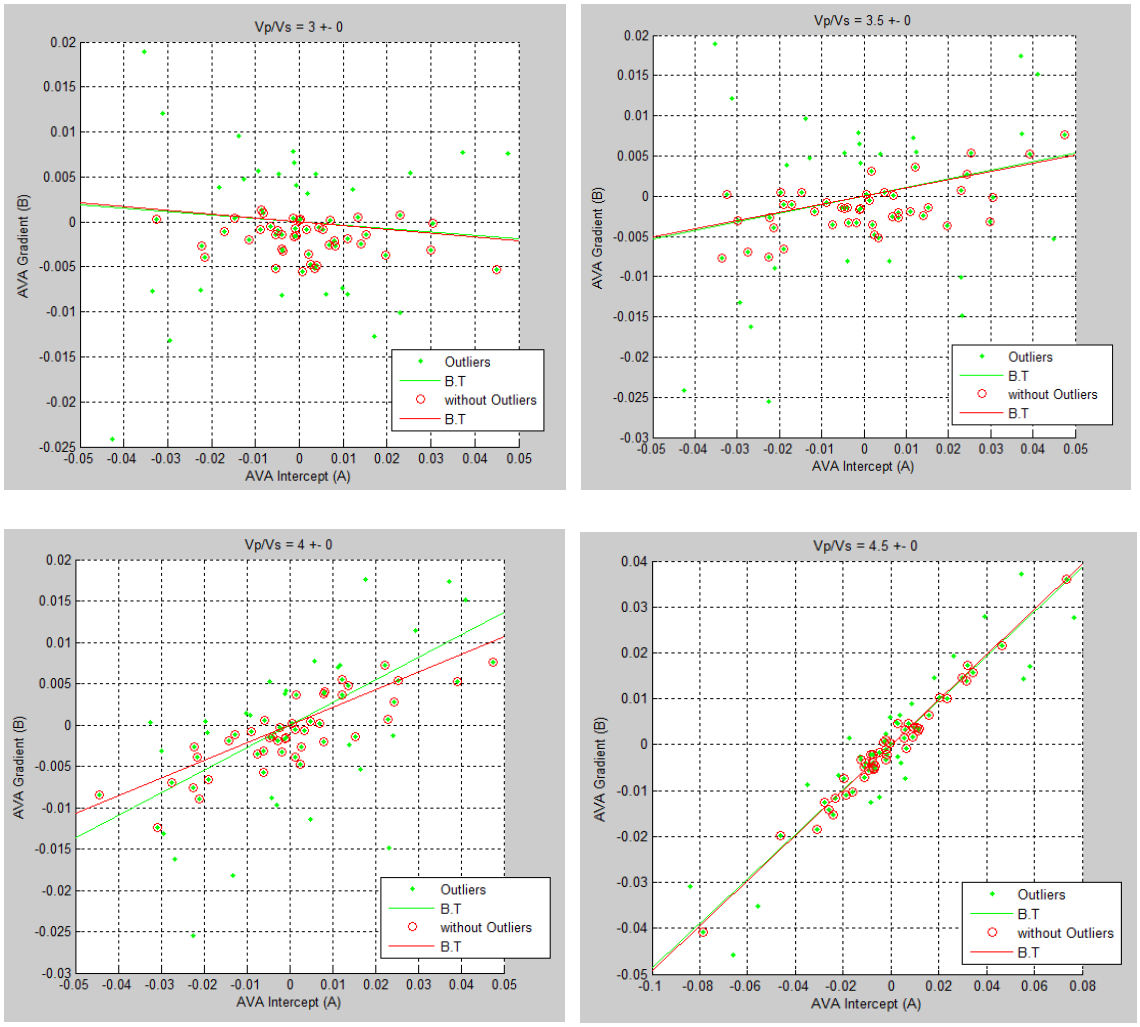

Fig. 3.2. Intercept and Gradient values calculated analytically, applying the Shuey's equation to pseudo logs of Vp, Vs and density with the variation of Vp/Vs ratio. The green line represent the slope of the Background Trend with outliers (green points), while, the red line represents the slope of the Background Trend without outliers (point circled in red).

In this case, the prediction made by the straight line of the Background Trend always overstimate the real Vp/Vs ratio, especially when we consider the Gardner Density.

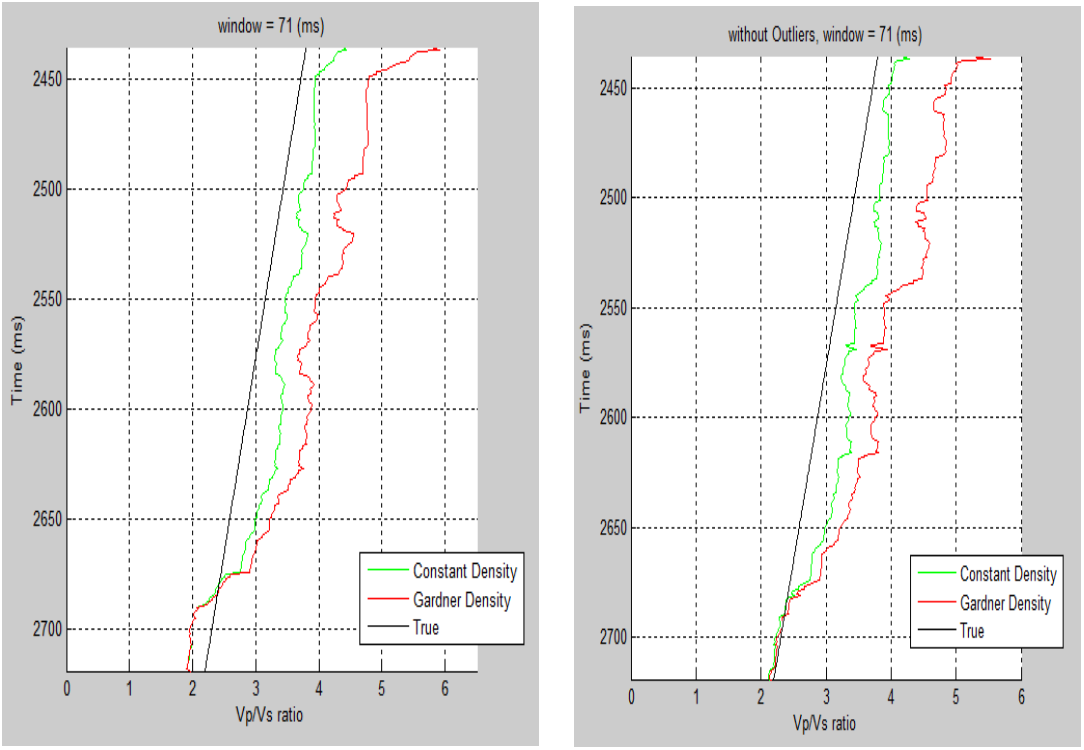

Fig. 3.3. Vp/Vs model (left) with outliers, and without outliers (right). Applying a time window of 71 (ms).

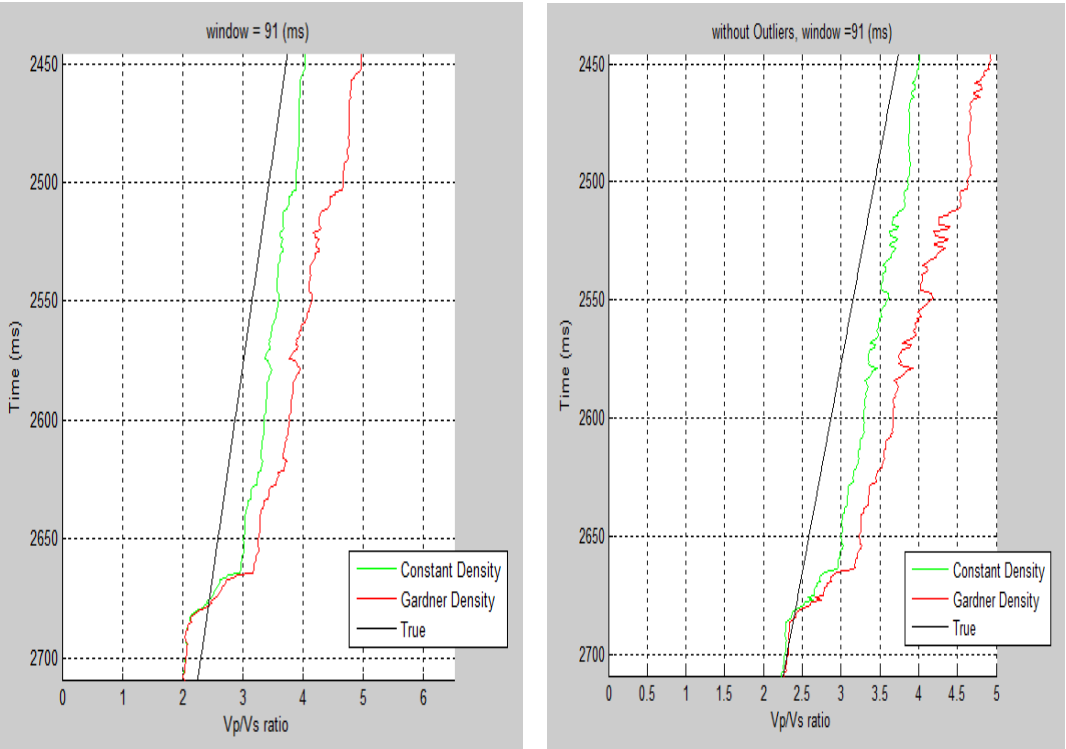

Fig. 3.4. Vp/Vs model (left) with outliers, and (right) without outliers. Applying a time window of 91 (ms).

Considering now a more realistic case where the Vp/Vs ratio does not remain constant throughout the interval described by the pseudo logs, but varies with a standard deviation of 0.01. The inclusion of changes in the Vp/Vs ratio simulates the presence of rapid discontinuity of Vp/Vs in correspondence of hypothetical layers of the subsoil. In this other case the slope of the Background Trend rotates counterclockwise. It notes that increasing the rate variation of Vp/Vs along the pseudo logs, it determines a greater divert of the Vp/Vs values predicted by Background Trend compared to the real values.

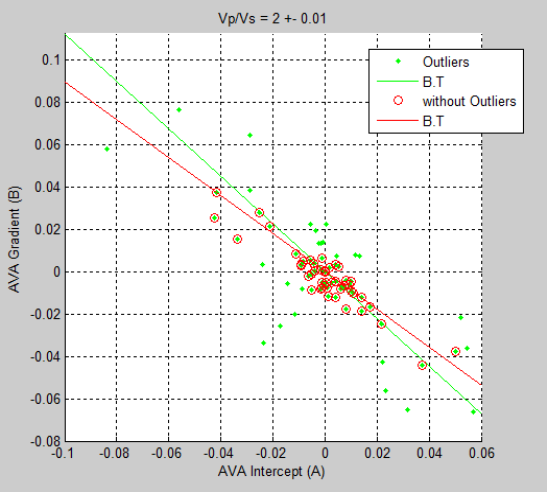
Vp/Vs = 2 +- 0.01
Outliers
B.T
without Outliers
B.T
AVA Gradient (B)
AVA Intercept (A)

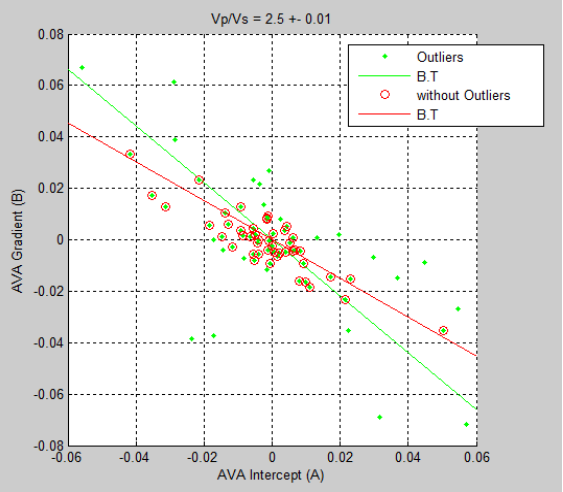
Vp/Vs = 2.5 +- 0.01
Outliers
B.T
without Outliers
B.T
AVA Gradient (B)
AVA Intercept (A)

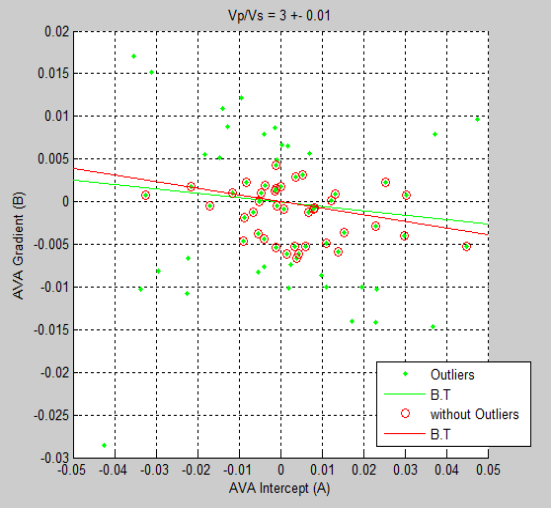
Vp/Vs = 3 +- 0.01
Outliers
B.T
without Outliers
B.T
AVA Gradient (B)
AVA Intercept (A)

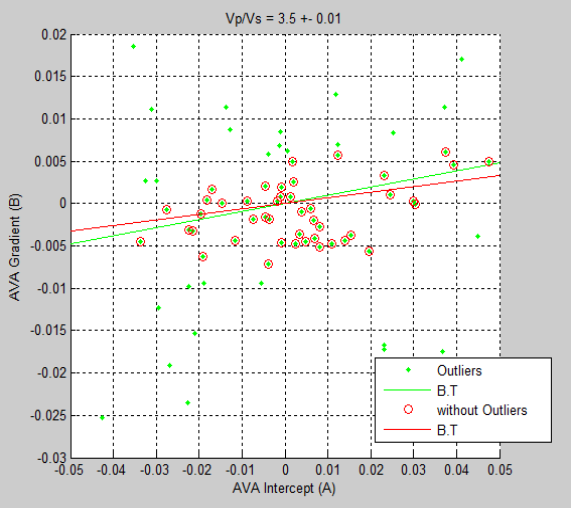
Vp/Vs = 3.5 +- 0.01
Outliers
B.T
without Outliers
B.T
AVA Gradient (B)
AVA Intercept (A)

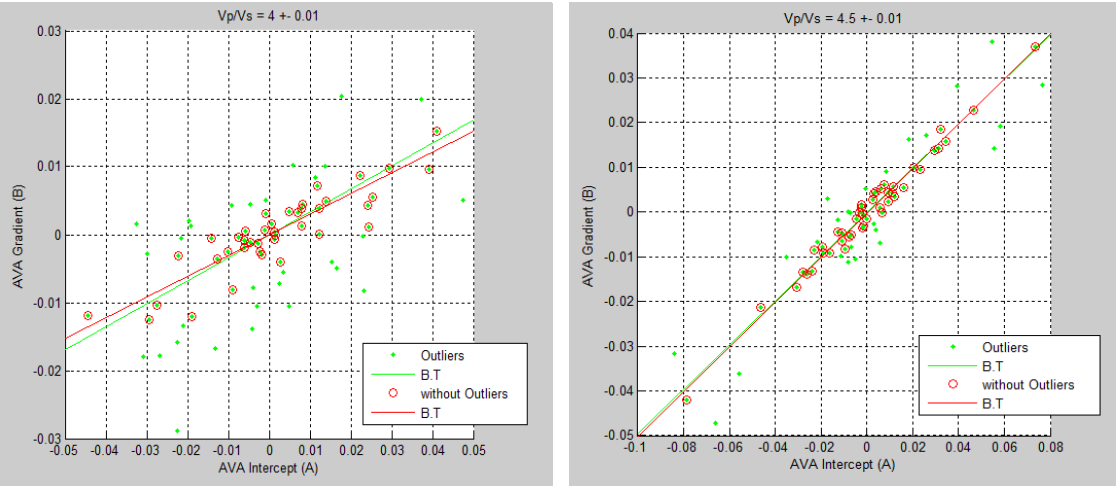

Fig. 3.5. Intercept and Gradient values calculated analytically, applying the Shuey's equation to pseudo logs of Vp, Vs and density with the variation of Vp/Vs ratio. The green line represent the slope of the Background Trend with outliers (green points), while, the red line represents the slope of the Background Trend without outliers (point circled in red). We can note, in this case the Vp/Vs ratio changes with a standard deviation = 0.01.

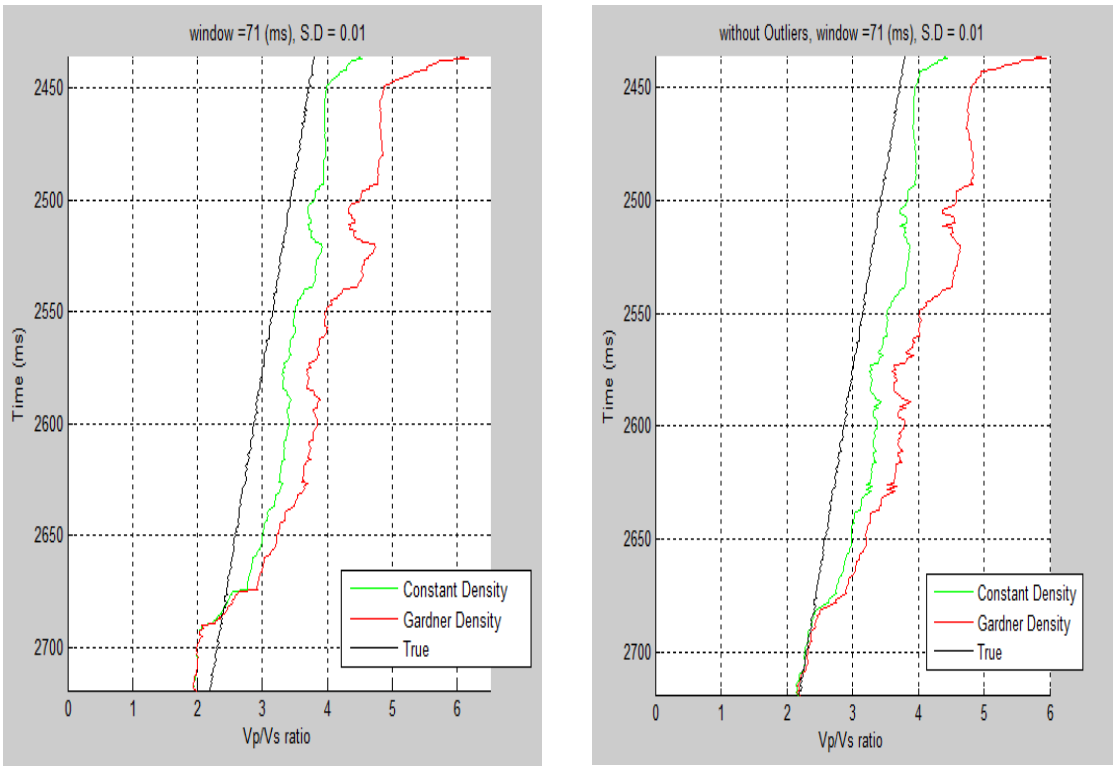

Fig. 3.6. Vp/Vs model (left) with outliers, and (right) without outliers. Applying a time window of 71 (ms). Applying a standard deviation = 0.01.

Considering a time window of 91 (ms) :

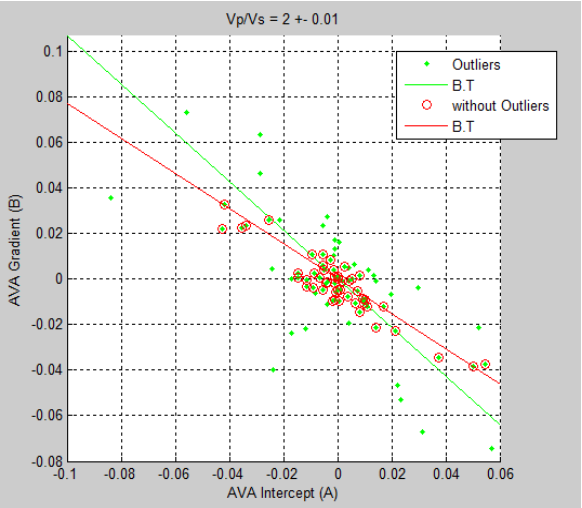

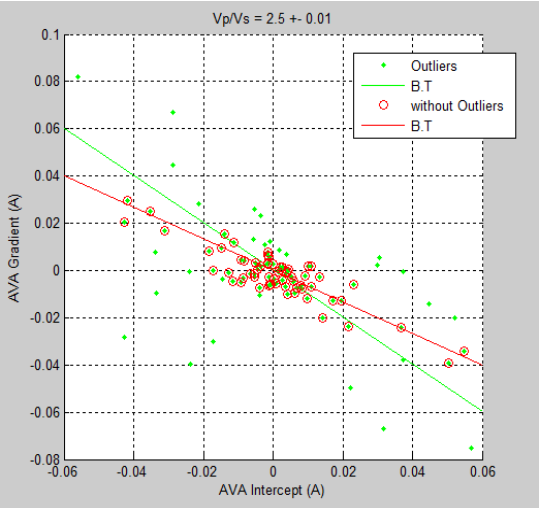

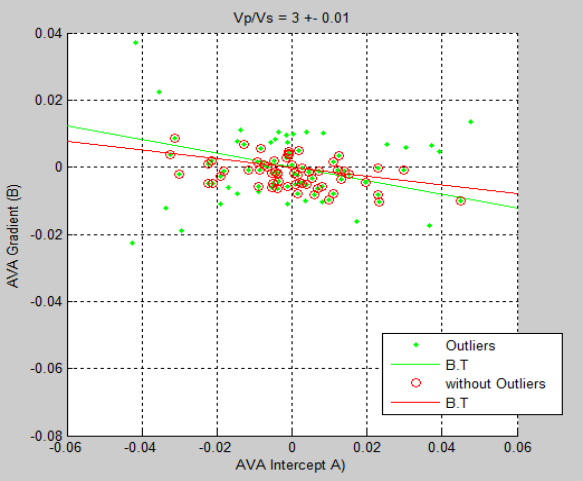

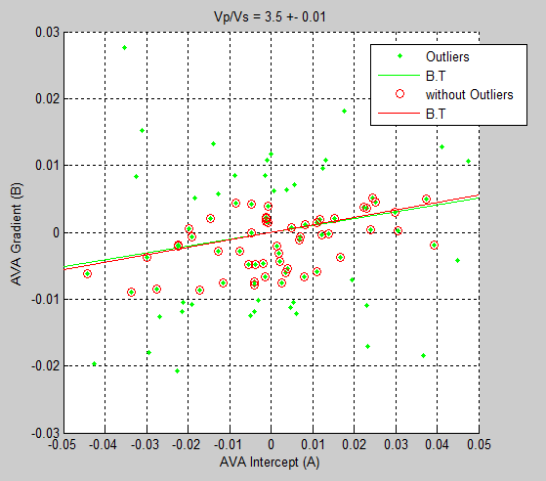

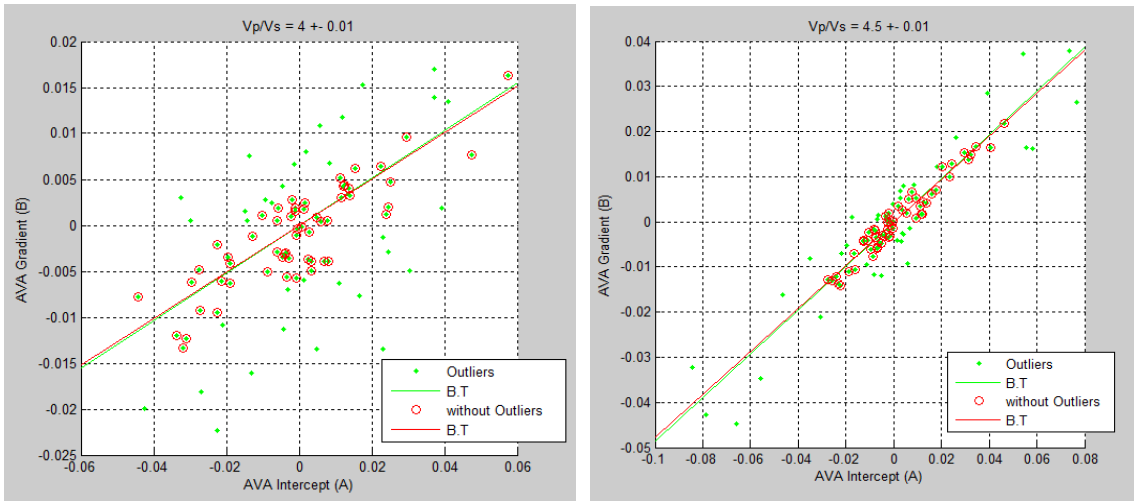

Fig. 3.7. Intercept and Gradient values calculated analytically, applying the Shuey's equation to pseudo logs of Vp, Vs and density with the variation of Vp/Vs ratio. The green line represent the slope of the Background Trend with outliers (green points), while, the red line represents the slope of the Background Trend without outliers (point circled in red). We can note, in this case the Vp/Vs ratio changes with a standard deviation = 0.01.

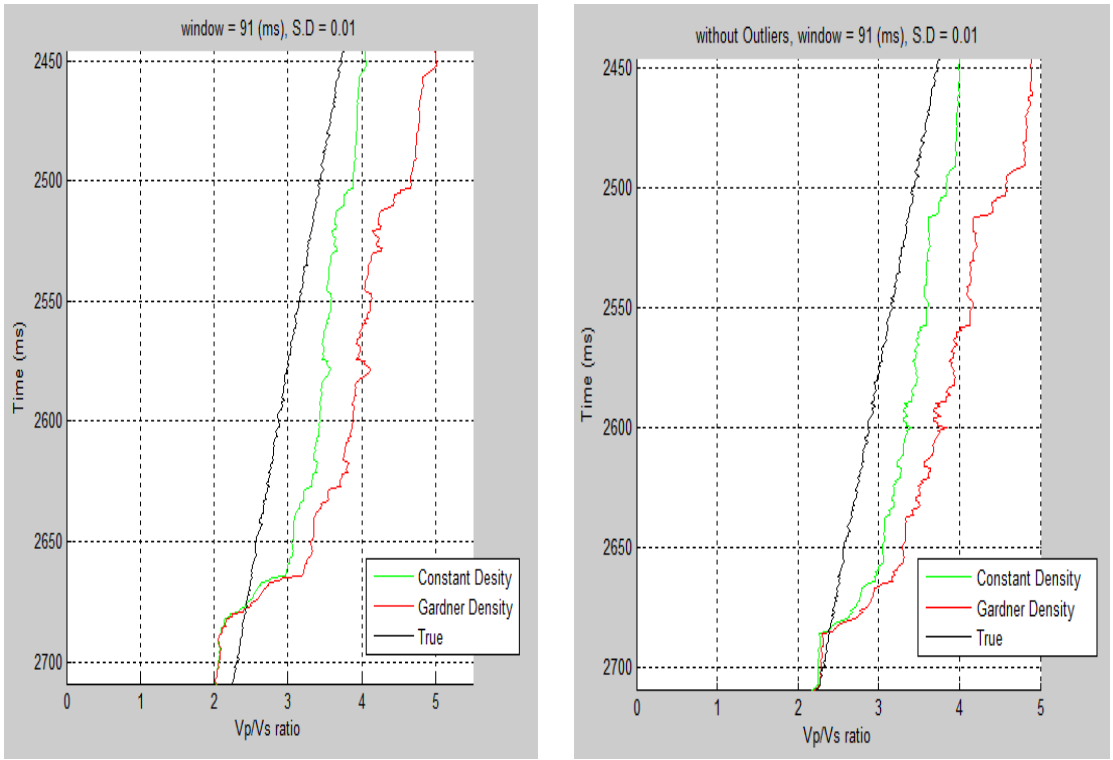

Fig. 3.8. Vp/Vs model (left) with outliers, and (right) without outliers. Applying a time window of 91 (ms). Applying a standard deviation = 0.01.

This divert becomes even more evidenti if we increase the standard to 0.05. We simulate the presence of even more significant fluctuations of Vp/Vs. The variation of Vp/Vs along the pseudo logs influence the assessment of the slope of Background Trend, particularly in cases of low Vp/Vs values (less than 3.5). A variations of Vp/Vs ratio produces a strong variation of the slope of the Background Trend.

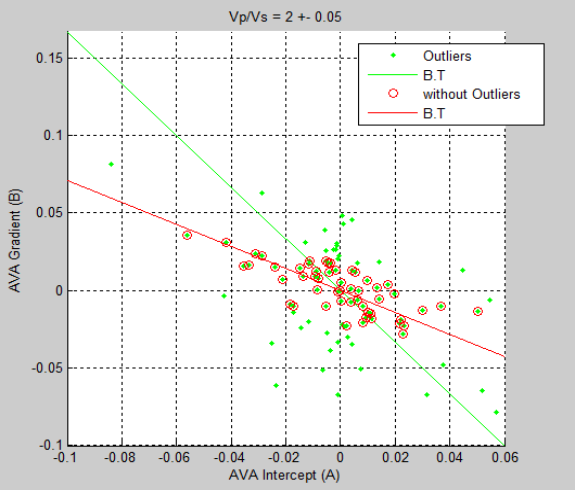

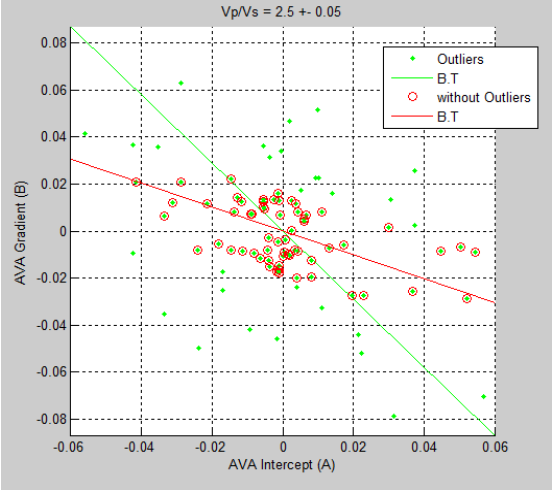

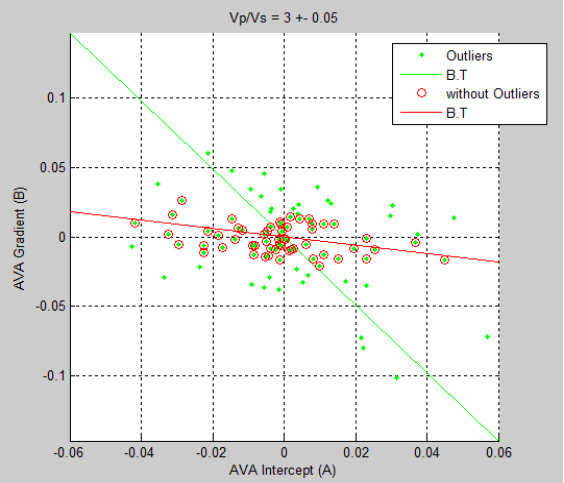

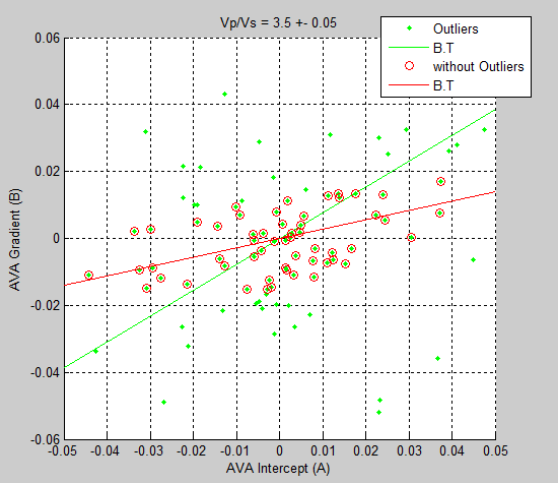

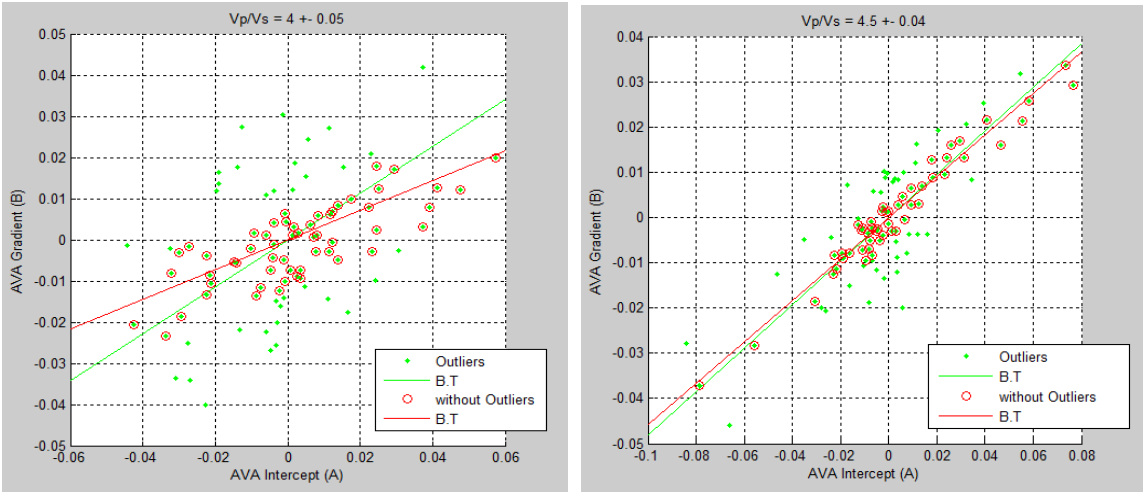

Fig. 3.9. Intercept and Gradient values calculated analytically, applying the Shuey's equation to pseudo logs of Vp, Vs and density with the variation of Vp/Vs ratio. The green line represent the slope of the Background Trend with outliers (green points), while, the red line represents the slope of the Background Trend without outliers (point circled in red). We can note, in this case the Vp/Vs ratio changes with a standard deviation = 0.05.

Considering the correct relationship of Vp/Vs ratio, the variations of Vp/Vs along the pseudo logs, it determines a small divert of the Vp/Vs values predicted by Background Trend compared to the correct relationship of Vp/Vs ratio. Considering a time window of 71 (ms):

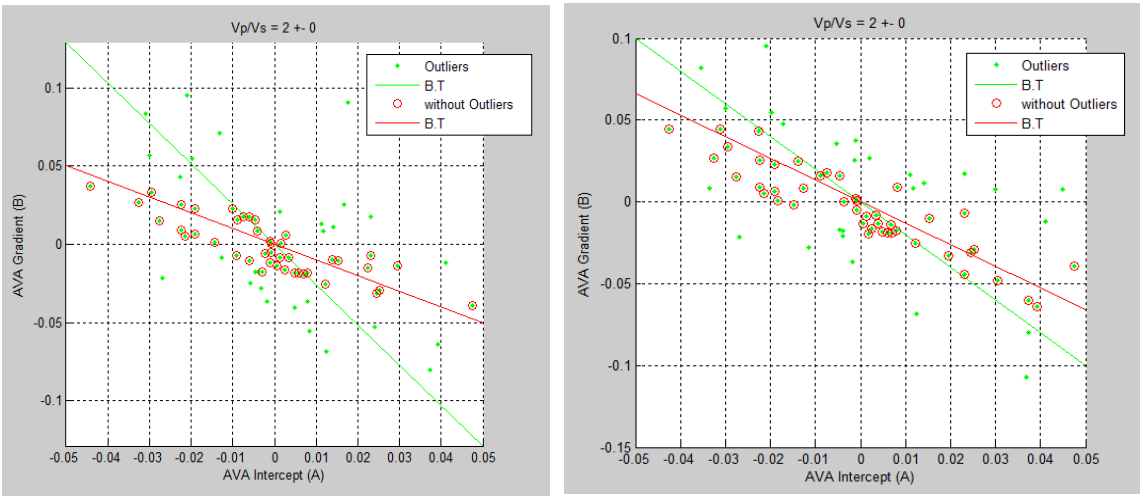

Fig. 3.9. Intercept and Gradient values calculated analytically, applying the Shuey's equation to pseudo logs of Vp, Vs and density with the variation of Vp/Vs ratio. The green line represent the slope of the Background Trend with outliers (green points), while, the red line represents the slope of the Background Trend without outliers (point circled in red). Correct relationship of Vp/Vs ratio.

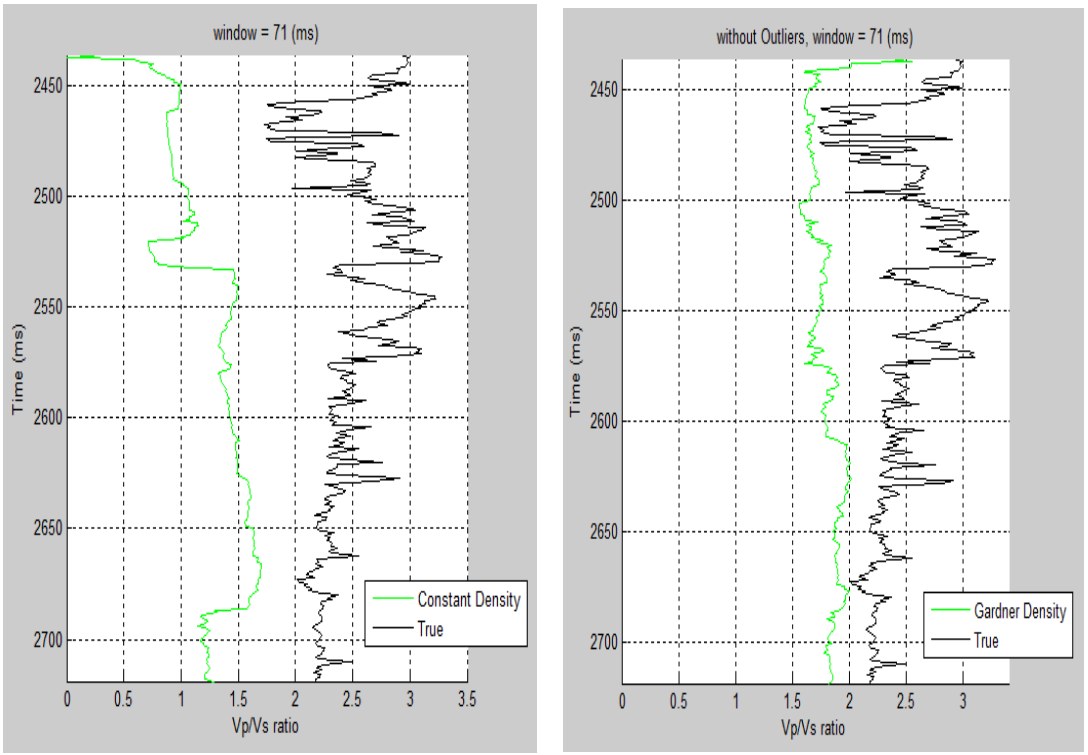

Fig. 3.10. Vp/Vs model (left) with outliers, and (right) without outliers. Correct relationship of Vp/Vs ratio.

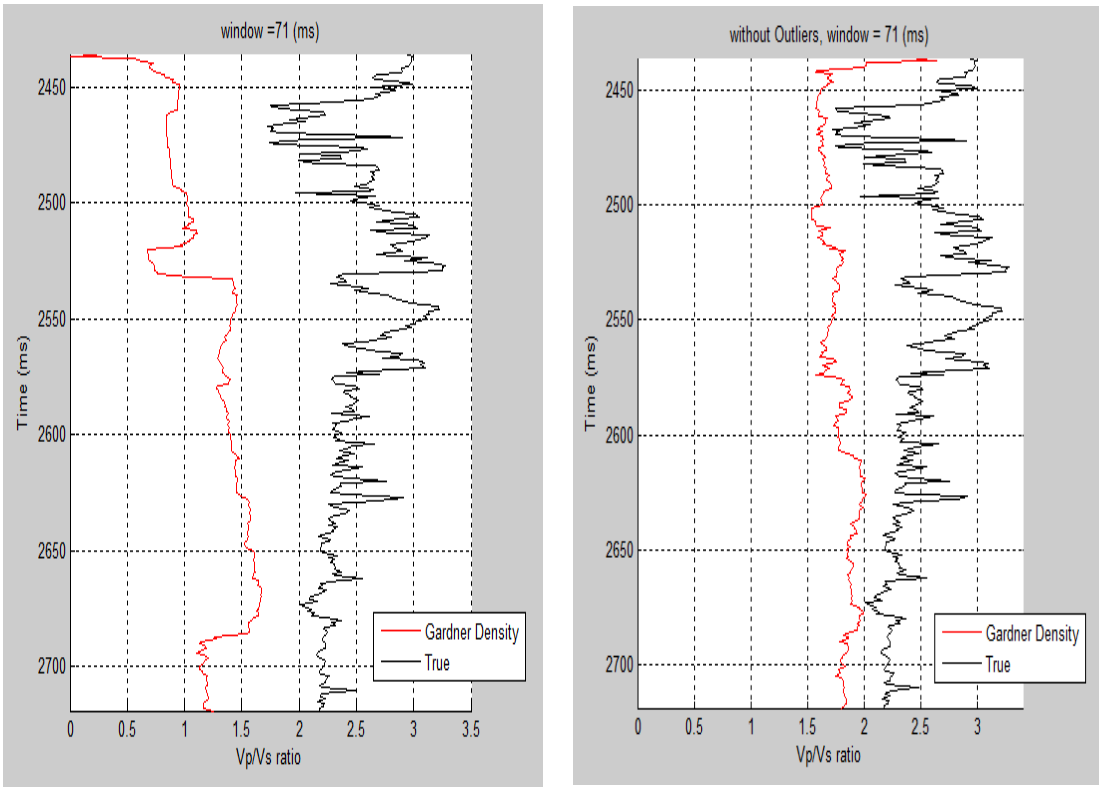

Fig. 3.11. Vp/Vs model (left) with outliers, and (right) without outliers. Correct relationship of Vp/Vs ratio.

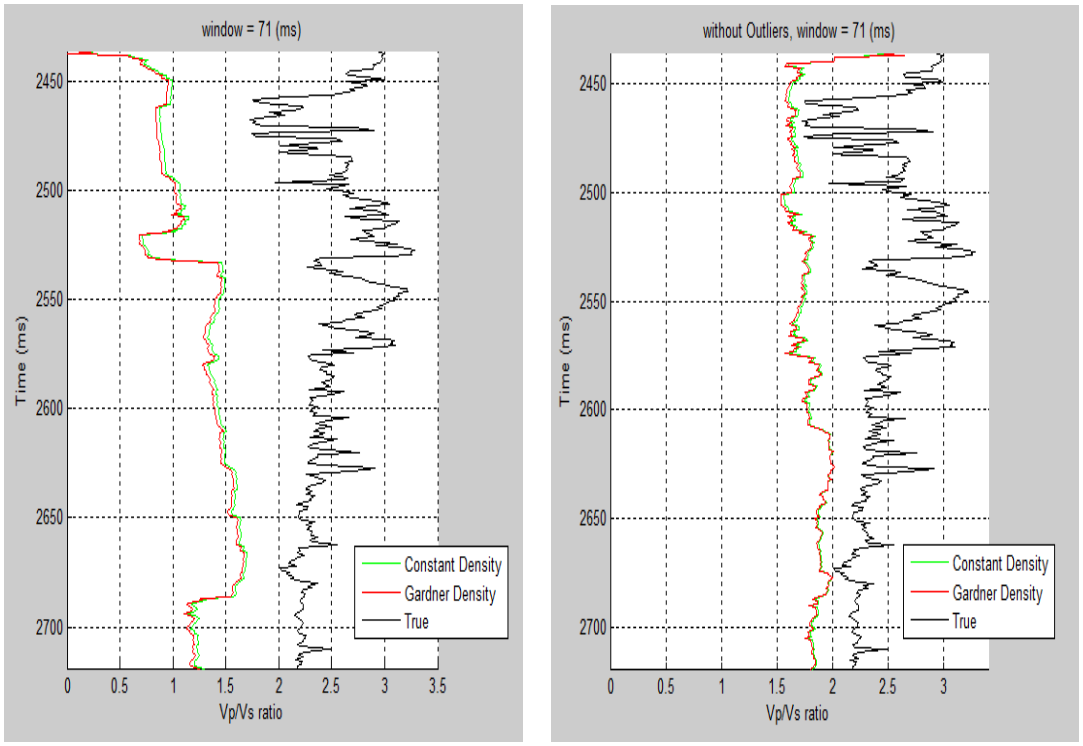

Fig. 3.12. Vp/Vs model (left) with outliers, and (right) without outliers. Correct relationship of Vp/Vs ratio.

Considering a time window of 91 (ms):

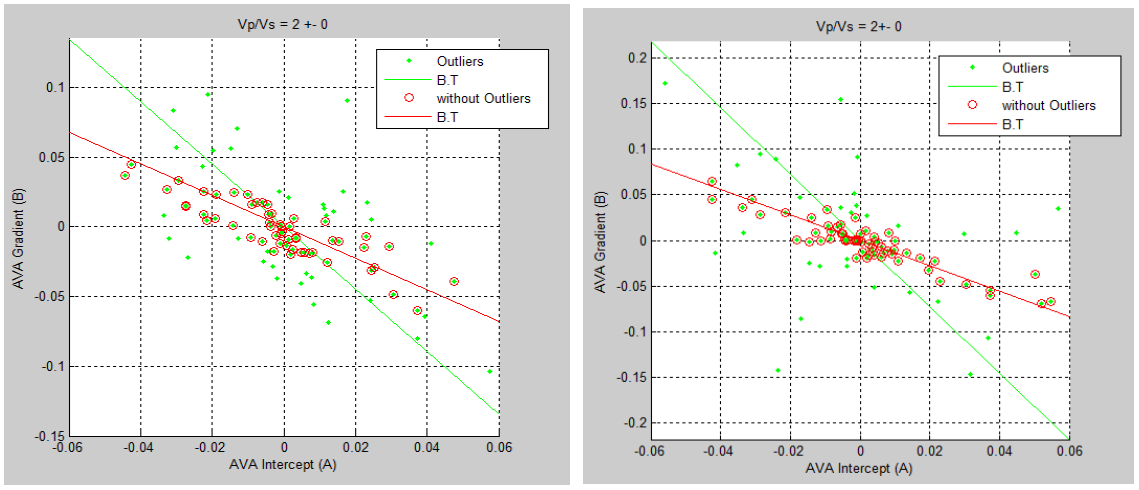

Fig. 3.13. Intercept and Gradient values calculated analytically, applying the Shuey's equation to pseudo logs of Vp, Vs and density with the variation of Vp/Vs ratio. The green line represent the slope of the Background Trend with outliers (green points), while, the red line represents the slope of the Background Trend without outliers (point circled in red). Correct relationship of Vp/Vs ratio.

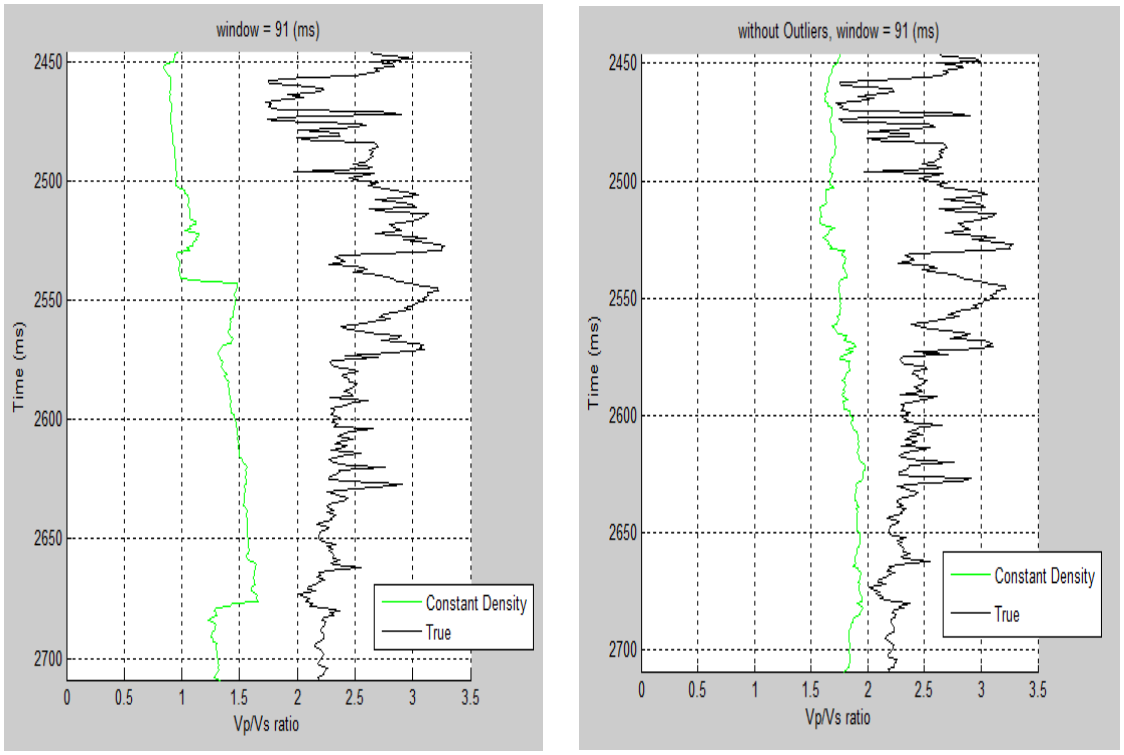

Fig. 3.14. Vp/Vs model (left) with outliers, and (right) without outliers. Correct relationship of Vp/Vs ratio.

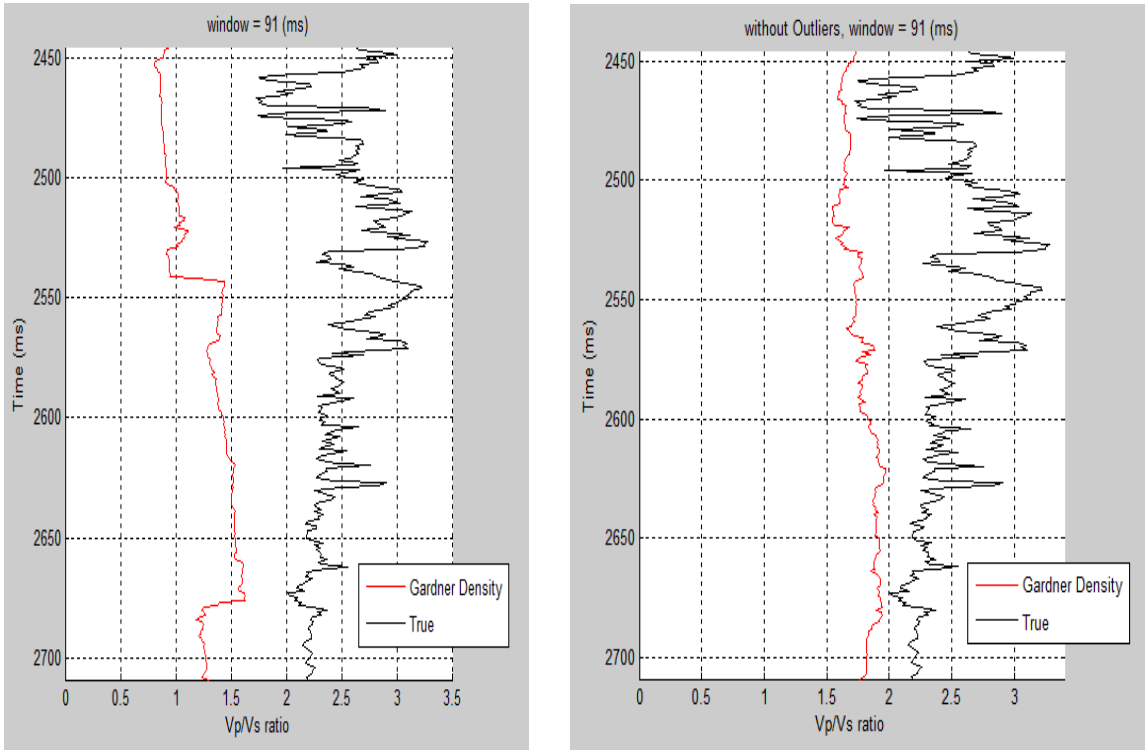

Fig. 3.15. Vp/Vs model (left) with outliers, and (right) without outliers. Correct relationship of Vp/Vs ratio.

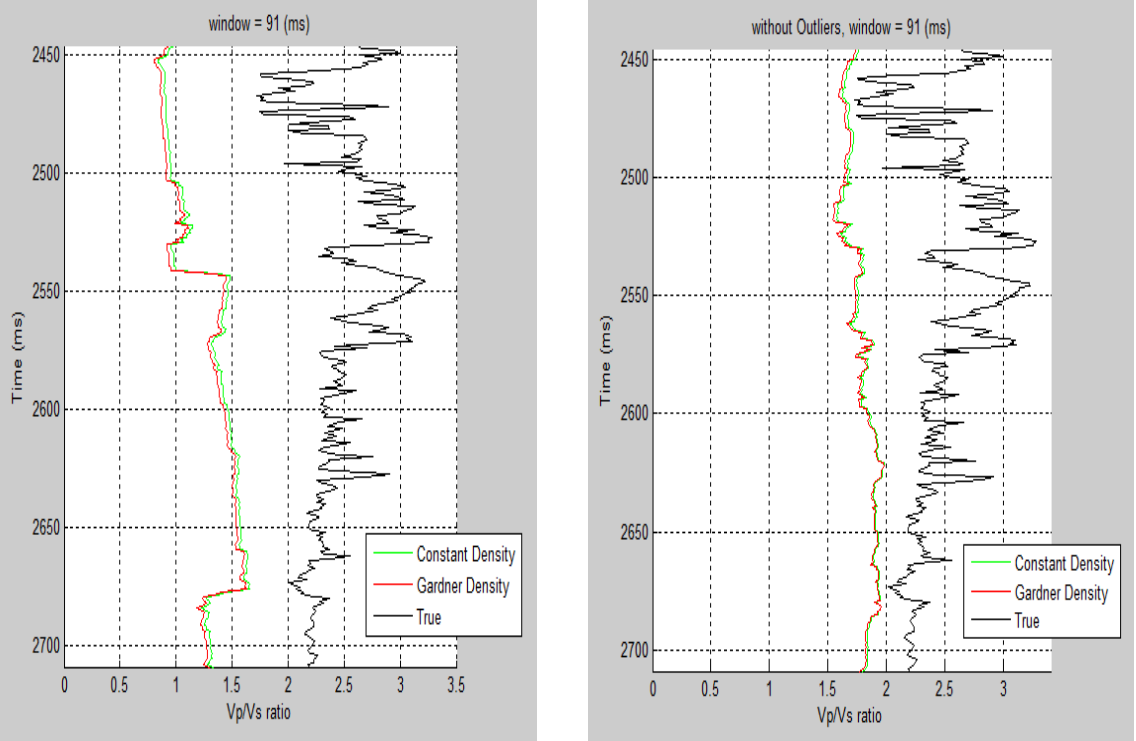

Fig. 3.16. Vp/Vs model (left) with outliers, and (right) without outliers. Correct relationship of Vp/Vs ratio.

Chapter 4

Experimental Response

This chapter shows an algorithm has been developed in Matlab. It consideres an AVA Experimental Response. In the AVA Experimental response, it has made use of well logs of the seismic velocities and density to derive the synthetic seismograms (CMP) using the convolutional method, and the Intercept and Gradient values extracted from synthetic seismograms .Shuey's approximation was used for AVA crossplot analysis. This Gradient ("slope") AVA attribute is calculated from a least square regression analysis of the amplitudes for angles from 0-30 degrees, using an X-axis of sine squared theta (where theta is the incidence angle), and the Intercept is zero-offset amplitude determinated (using an Y-axis the amplitude) by extrapolating the AVA Gradient. Each point in the AVA crossplot is mapped using the amplitude of Intercept (A) and Gradient (B) in a time window. Within this time window, it has calculated the *Singular Value Decomposition* (SVD), and obtained the eingenvector associated with the first singular value that gives the direction of maximum variance. The angle was calculated from the eingenvector that meet with the horizontal, it characterizes the Background Trend (Vp/Vs) was subsequently converted into Vp/Vs ratio value to predict two empirical equations, Costant Density and Gardner Density (as showed the chapter 2 and 3). The stability of the Background Trend (Vp/Vs) can have an impact on what is being interpretated as anomalous, be it fluid or lithology induced outliers. To stabilize the estimation of Vp/Vs from the slope of the Background Trend, to do this, proceeded through the operation of outlier removal in Itercept and Gradient domain.

4.1 The Convolutional Model in Time Domain

Suppose a vertically propagating downgoing plane wave with source signature (4.1.a) travels in depth and encounteres a layer boundary at 0.2-s two-way time. The reflection coefficient associated with the boundary is represented by the spike in (Figure 4.1.b). As a result of reflection, the source wavelet replicates itself such that it is scaled by the reflection coefficient. If we have a number of layer boundaries represented by the individual spikes in (Figures 4.1.b through 4.1.f), then the wavelet replicates itself at those boundaries in the same manner. If the reflection coefficienti is negative, then the wavelet replicates itself with its polarity reversed, as in (Figure 4.1.c). Now consider the ensemble of the reflection coefficients in (Figure 4.1.g). The response of this sparse spike series to the basic wavelet is a superposition of the individual impulse response. This linear processi s called the *principle of superposition*. It is achieved computationally by convolving the basic wavelet with the reflectivity series (Figure 4.1.g). The response of the sparse spike series to the basic wavelet in Figure 4.1.g has some important characteristics. Note that for events at 0.2 and 0.35 s, we identify two layer boundaries. However, to identify the three closely spaced reflecting boundaries from the composite response (at around 0.6 s).

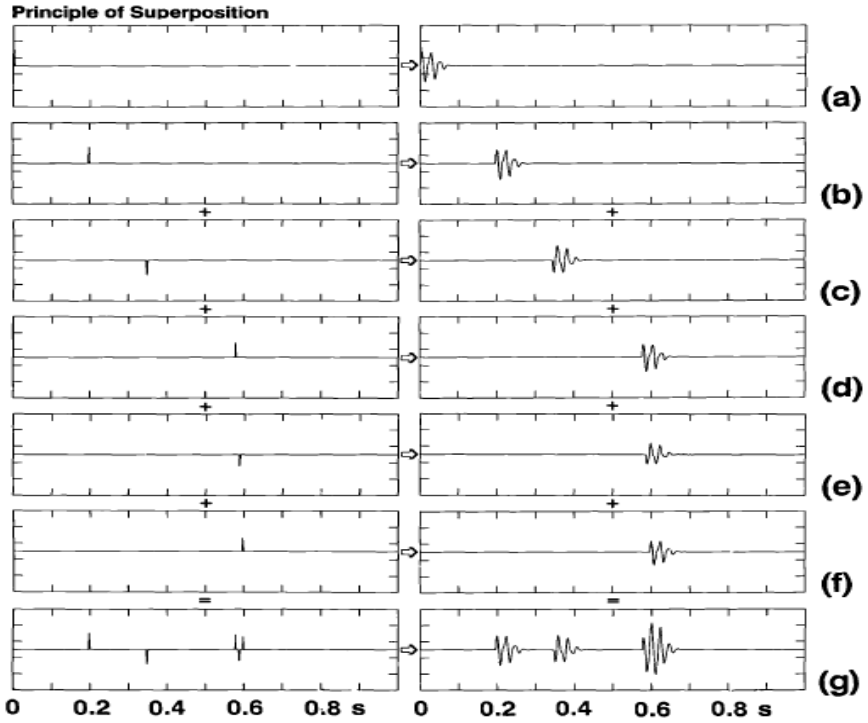

Fig. 4.1. A wavelet (a) traveling in the earth repeats itself when it encounters a reflector along its path (b, c, d, e, f). The left column represents the reflection Coefficients, while the right column represents the response to the wavelet. Amplitudes of the response are scaled by the reflection coefficient. The resulting seismogram (bottom right) represents the composite response of the earth reflectivity (bottom left) to the wavelet (top right), (Figure from Yilmaz, 1987).

Convolution of a source signature with the impulse response yields the synthetic sesmogram shown in (Figure 4.2). For a more realistic representation of a recorded seismogram, noise is added (Figure 4.2). Mathematically, the convolutional model illustrated in (Figure 4.2) is given by

$$x(t) = w(t) * e(t) + n(t), \qquad (4.1)$$

where $x(t)$ is the recorded seismogram, $w(t)$ is the basic seismic wavelet, $e(t)$ is the earth's impulse response, $n(t)$ is the random ambient noise, and * denotes convolution.

In equation (4.1), $x(t)$ is known (the recorded seismogram). The earth's impulse response $e(t)$ must be estimated everywhere except at the location of wells with good sonic logs. Also, the surce waveform $w(t)$ normally in unknown. In certain cases, however, the source

waveform is partly known; for example, the signature of an air-gun array can be measured. However, what is measured is only the waveform at the very onset of excitation of the source array, and not the wavelet that is recorded at the receiver. Finally, there is no a priori knowledge of the ambient noise n (t).

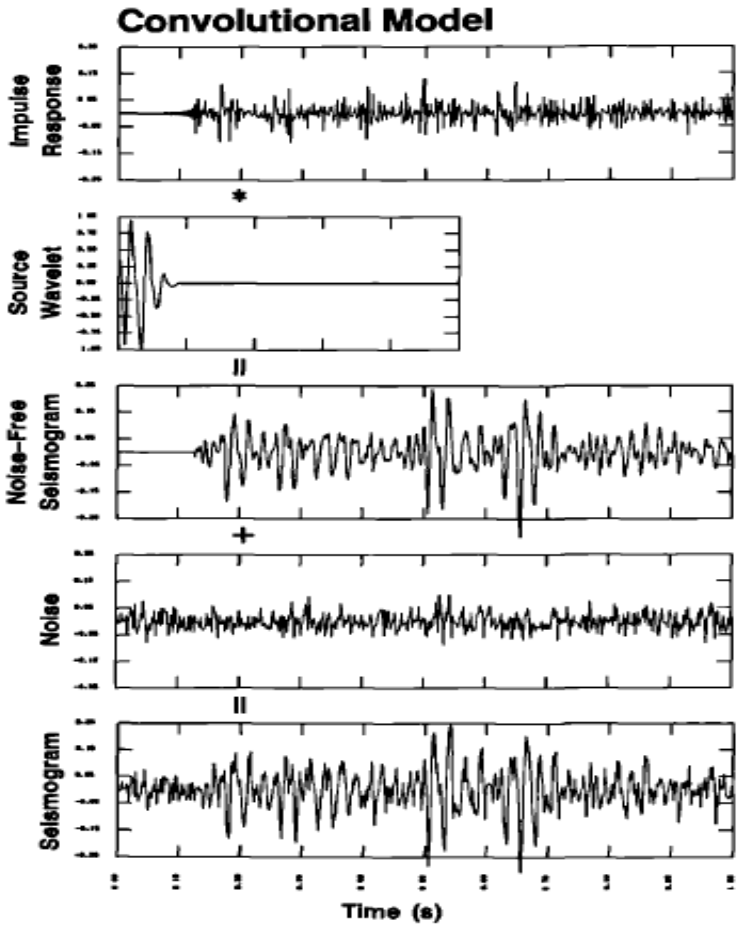

Figure 4.2. The asterisk denotes convolution. The recorded seismogram (bottom frame) is the sum of the noise free seismogram and the noise trace (Figure from Yilmaz, 1987).

4.2 Methodology

Seismic reflection coefficients depend on the material properties of the subsurface. An isotropic, elastic medium is completely described by three material parameters. We have chosen {α (*t*), β (*t*), ρ (*t*)}, where α is P-wave velocity, β is S-wave velocity, ρ is density, and *t* is the two-way vertical seismic traveltime. The inversion method is based on a weak contrast approximation to the PP reflection coefficient (Aki and Richards, 1980):

$$c_{pp}(\theta) = a_{\alpha}(\theta)\frac{\Delta\alpha}{<\alpha>} + a_{\beta}(\theta)\frac{\Delta\beta}{<\beta>} + a_{\rho}(\theta)\frac{\Delta\rho}{<\rho>} \tag{4.2}$$

where

$$a_{\alpha}(\theta) = \frac{1}{2}(1 + tan^2\theta), \tag{4.3}$$

$$a_{\beta}(\theta) = -4\frac{<\beta>^2}{<\alpha>^2}sin^2\theta, \tag{4.4}$$

$$a_{\rho}(\theta) = \frac{1}{2}\left(1 - 4\frac{<\beta>^2}{<\alpha>^2}sin^2\theta\right). \tag{4.5}$$

where, $<\alpha>$, $<\beta>$ and $<\rho>$ are averages over the reflecting interface; $\Delta\alpha$, $\Delta\beta$ and $\Delta\rho$ are the corresponding contrasts; and θ is the reflection angle.

The single-interface reflection coefficient in equation (4.2) can be extended to a time-continuous reflectivity function (Stolt and Weglein, 1985):

$$c_{pp}(\theta) = a_{\alpha}(t,\theta)\frac{\partial}{\partial t}ln\,\alpha(t) + a_{\beta}(t,\theta)\frac{\partial}{\partial t}ln\,\beta(t) + a_{\rho}(t,\theta)\frac{\partial}{\partial t}ln\,\rho(t), \tag{4.6}$$

where $a_{\alpha}(t,\theta)$, $a_{\beta}(t,\theta)$ and $a_{\rho}(t,\theta)$ are generalizations of the coefficients in expressions (4.3)-(4.5) with time-dependent velocities $<\alpha(t)>$ and $<\beta(t)>$. We assume that $<\alpha(t)>$ and $<\beta(t)>$ can be represented by a constant or slowly varying known background model, such that $<\alpha(t)>$ and $<\beta(t)>$ are the average or moving average of α (*t*), β (*t*) in a time window. The reflection angle θ is used as an independent variable. However,

the seismic data are recorded as a function of source-receiver distance h (offset). The trasform of the data from the (t, h) domain to the (t, θ) domain depends on the velocity function. This transform can be performed by offset-angle relations based on a smooth background model.

4.3 AVA Forward Modeling

A discrete version of the continuos reflectivity function :

$$c_{pp}(\theta) = a_\alpha(t,\theta)\frac{\partial}{\partial t} ln\,\alpha(t) + a_\beta(t,\theta)\frac{\partial}{\partial t} ln\,\beta(t) + a_\rho(t,\theta)\frac{\partial}{\partial t} ln\,\rho(t), \qquad (4.7)$$

in a time interval and for a set of reflection angles can be written as

$$\mathbf{C = A\ m'} \qquad (4.8)$$

where

$$\mathbf{m} = \left[\frac{\partial}{\partial t} ln\,\alpha(t), \frac{\partial}{\partial t} \ln\beta(t), \frac{\partial}{\partial t} ln\,\rho(t) \right]^T \qquad (4.9)$$

where the elements can be regognized in the reflectivity function, expression (4.6)

The sparse matrix **A** is defined by

$$\mathbf{A} = \begin{bmatrix} \mathbf{A}_\alpha(\theta_1) & \mathbf{A}_\beta(\theta_1) & \mathbf{A}_\rho(\theta_1) \\ \vdots & \vdots & \vdots \\ \mathbf{A}_\alpha(\theta_{n_\theta}) & \mathbf{A}_\beta(\theta_{n_\theta}) & \mathbf{A}_\rho(\theta_{n_\theta}) \end{bmatrix},$$

where $A_\alpha(\theta_i)$, $A_\beta(\theta_i)$, and $A_\rho(\theta_i)$ are $(n_m/3) \times (n_m/3)$ diagonal matrices containing discrete time samples of $a_\alpha(t, \theta_i)$, $a_\beta(t, \theta_i)$, and $a_\rho(t, \theta_i)$, respectively; n_θ is the number of reflection angles; and nm is the dimension of **m** and **m'**.

The convolution of the reflection coefficients **c** with the wavelets can be formulated as a matrix-vector multiplication

$$\mathbf{d}_{obs} = \mathbf{Sc} + \mathbf{e}, \tag{4.10}$$

where **S** is a block-diagonal matrix containing one wavelet for each reflection angle. In an expanded form, expression ( ) can be written

$$\begin{bmatrix} \mathbf{d}_{obs}(\theta_1) \\ \vdots \\ \mathbf{d}_{obs}(\theta_{n_\theta}) \end{bmatrix} = \begin{bmatrix} \mathbf{S}(\theta_1) & & \\ & \ddots & \\ & & \mathbf{S}(\theta_{n_\theta}) \end{bmatrix} \times \begin{bmatrix} \mathbf{c}(\theta_1) \\ \vdots \\ \mathbf{c}(\theta_{n_\theta}) \end{bmatrix} + \begin{bmatrix} \mathbf{e}(\theta_1) \\ \vdots \\ \mathbf{e}(\theta_{n_\theta}) \end{bmatrix}$$

Where $\mathbf{d}_{obs}(\theta_i)$ is the seismic time trace for angle θ_i and where $\mathbf{c}(\theta_i)$ and $e(\theta_i)$ are the corresponding reflection coefficients and error samples, respectively. The block matrix $\mathbf{S}(\theta_i)$ represents the wavelet for angle (θ_i)

$$\mathbf{S}(\theta_i) = \begin{bmatrix} s_1(\theta_i) & & & & & & \\ s_2(\theta_i) & s_1(\theta_i) & & & & & \\ \vdots & & \ddots & & & & \\ s_{n_s}(\theta_i) & \cdots & \cdots & s_1(\theta_i) & & & \\ & \ddots & & & \ddots & & \\ & & s_{n_s}(\theta_i) & \cdots & \cdots & s_1(\theta_i) & \\ & & & \ddots & & \vdots & \\ & & & & \ddots & \vdots & \\ & & & & & s_{n_s}(\theta_i) & \end{bmatrix}$$

Where $(s_1(\theta_i), \ldots\ldots, s_{ns}(\theta_i))$ are the samples of the wavelet for angle θ_i. In this example, the sampling of the wavelet is equal to the sampling of the seismic data. If the sampling

of **c** and dobs are different, the rows of **S** contains wavelets corresponding to the sampling of **c**, and the rows are shifted relatively according to the sampling of $\mathbf{d}_{obs}$.

Input parameters for *seismic forward modeling*:

- Vp, Vs, Ro well logs (Figure 4.3).
- The maximum incidence angle considered is approximately 30 degrees.
- Ricker wavelet to zero phase (Figure 4.4) with:
    - Lenght = 71 (sample)
    - Frequency = 50 Hz
    - Sampling interval = 2 (ms)
- Recording Time = 355 (ms).

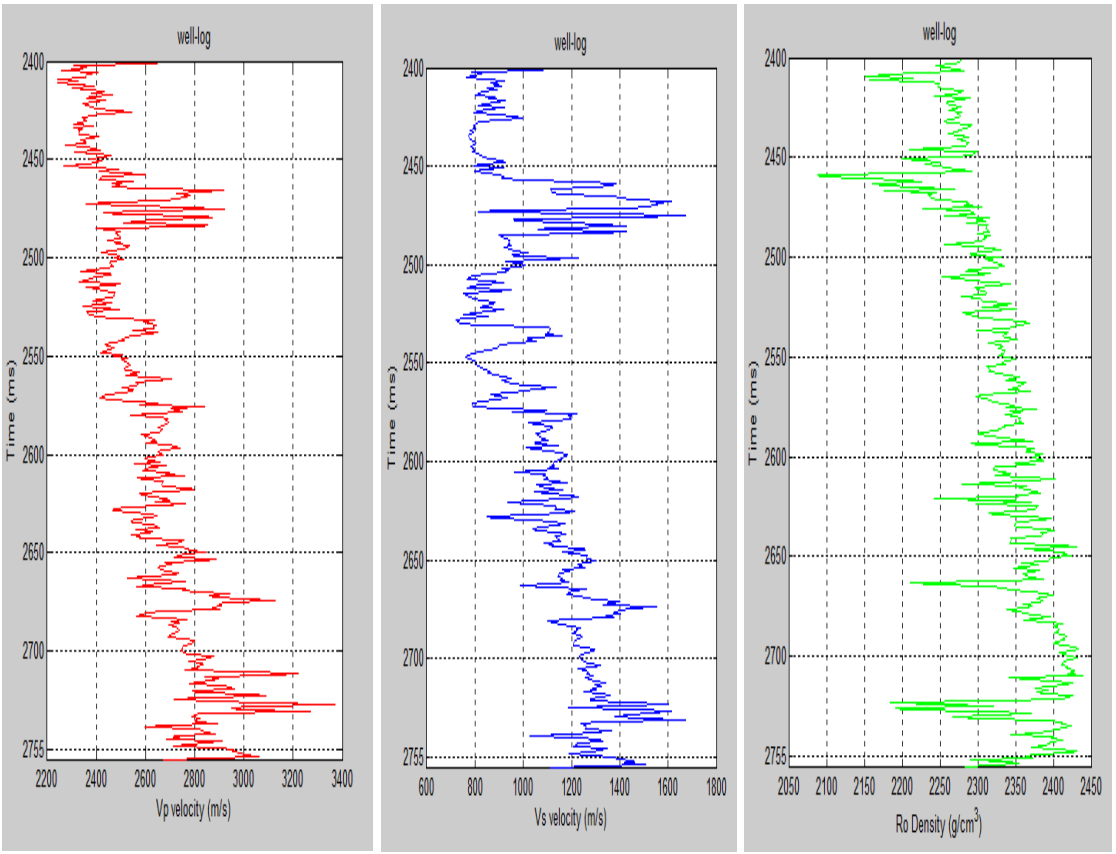

Fig. 4.3. Vp,Vs and Ro well logs.

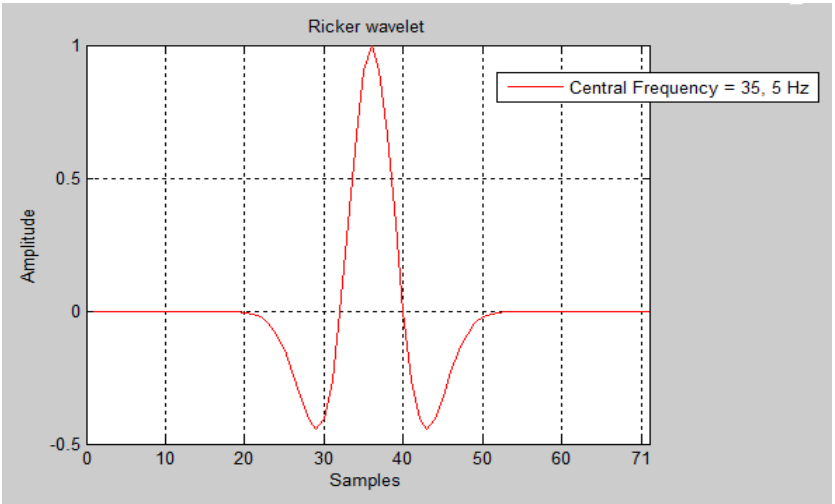

Fig.4.4. Ricker wavelet.

The convolutional model illustrated in (Figure 4.5):

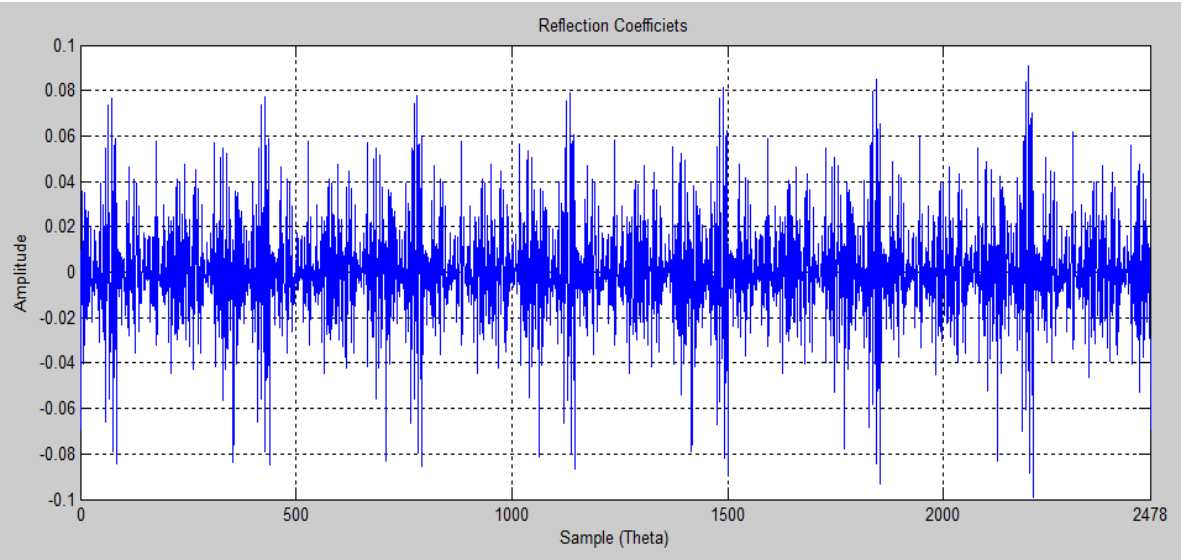

×

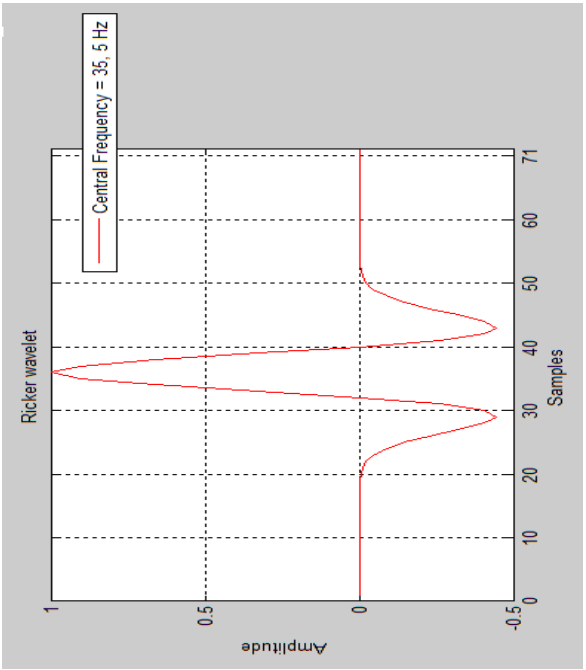

=

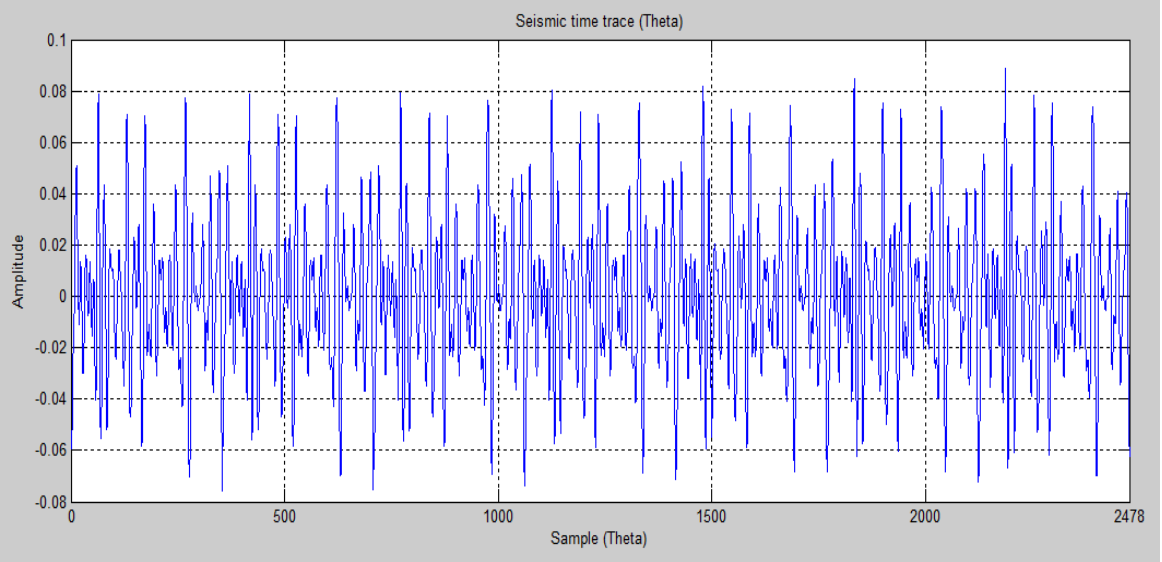

Fig. 4.5. Convolutional model (CMP). It shows the Seismic time trace for angle θ_i.

In the AVA Experimental response, the Intercept and Gradient values extracted from synthetic seismograms, which are obtained from velocity corrected CMP records. This Gradient ("slope") AVA attribute is calculated from a least square regression analysis of the amplitudes for angles from 0-30 degrees, using an X-axis of sine squared theta (where theta is the incidence angle), and the Intercept is zero-offset amplitude determined (using an Y-axis the amplitude) by extrapolating the AVA Gradient. In the Experimental Response several examples were evaluated, applying of the time windows of 71 (ms) and 91 (ms).

As illustrated in the third chapter (from equations 3.11, 3.14-3.20), the same equations were used in the Experimental response to extract Vp/Vs values, as follow:

1) costant density

$$B = \left[1 - 8\left(\frac{<Vs>}{<Vp>}\right)^2\right] A \tag{4.11}$$

$$\frac{<Vp>}{<Vs>} = \frac{\sqrt{-8}}{\sqrt{\frac{B}{A} - 1}} \tag{4.12}$$

2) Gardner density

$$B = \frac{4}{5}\left[1 - 9\left(\frac{<Vs>}{<Vp>}\right)^2\right] A \tag{4.13}$$

$$\frac{<Vp>}{<Vs>} = \frac{\sqrt{-9}}{\sqrt{\left(\frac{5}{4}\right)\frac{B}{A} - 1}} \tag{4.14}$$

In order to simulate variations in rock properties, we introduce perturbations to the reference model. Seismic modeling is carried out with the perturbed model, and values for *R0* and *G* are estimated.

It begins from the simplest case where the Vp/Vs ratio remains costant throughout the interval described by pseudo logs. The assessment Vp/Vs by the slope of the Background Trend, it closes fit to the real. Moreover, we note, as strong reflections (such as those seen

between 2410 and 2500 ms) can locally perturb the Gradient and Intercept values, and therefore, the asses of the slope of the Background Trend.

Throught a function, it has transformed vector to matrix, and it obtained a synthetic seismogram:

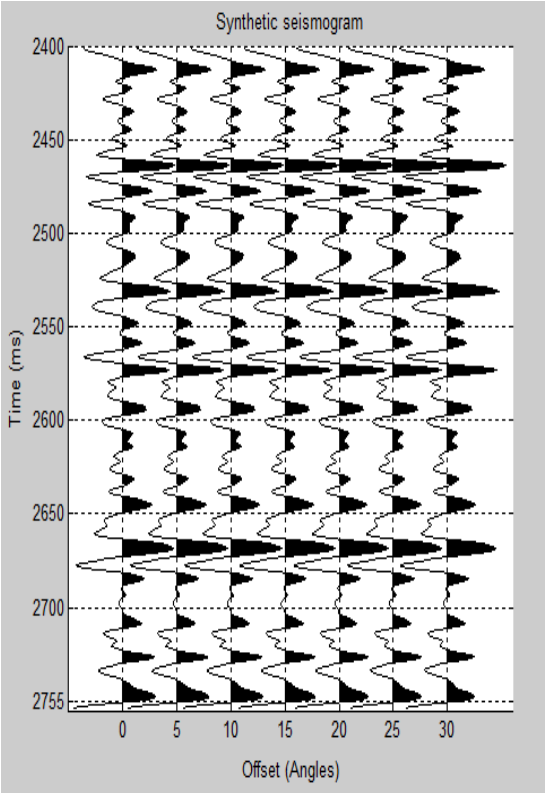

Fig. 4.6. Synthetic seismogram

Time window = 71 (ms):

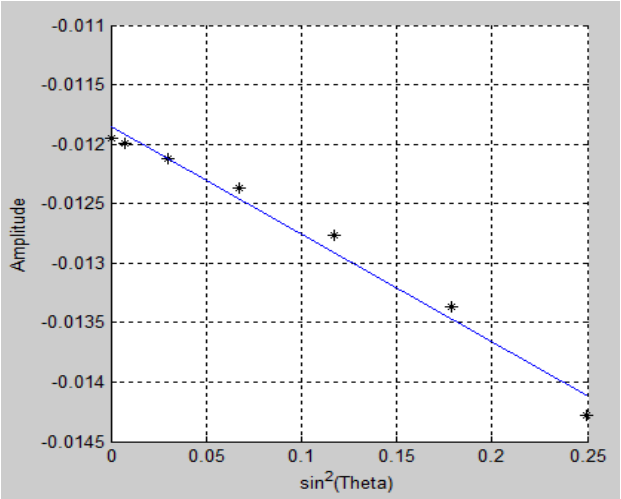

Figure 4.7: Estimated reflection coefficients from the synthetic seismic shown in Figure 4.6. The AVA parameters R_0 and G are computed from linear regression on the data.

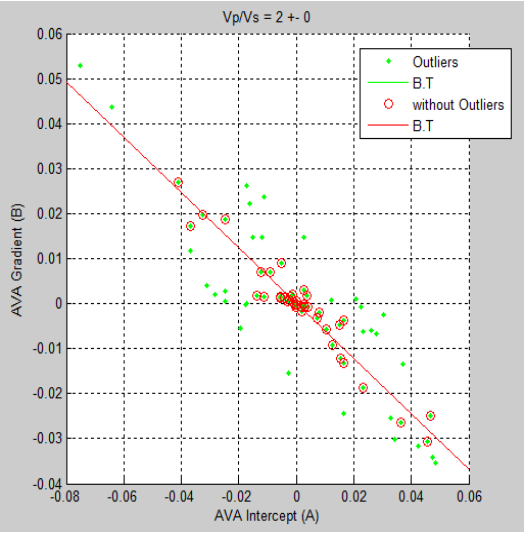

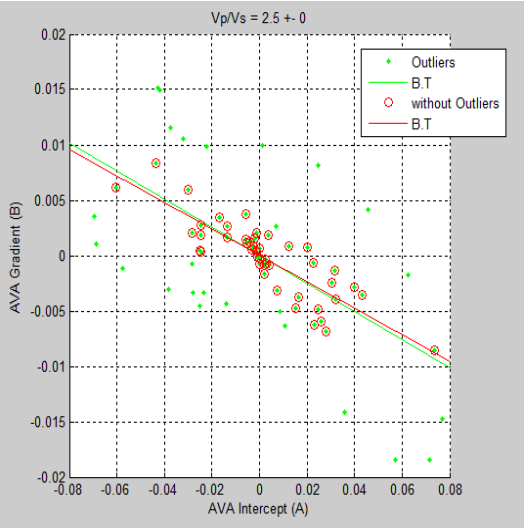

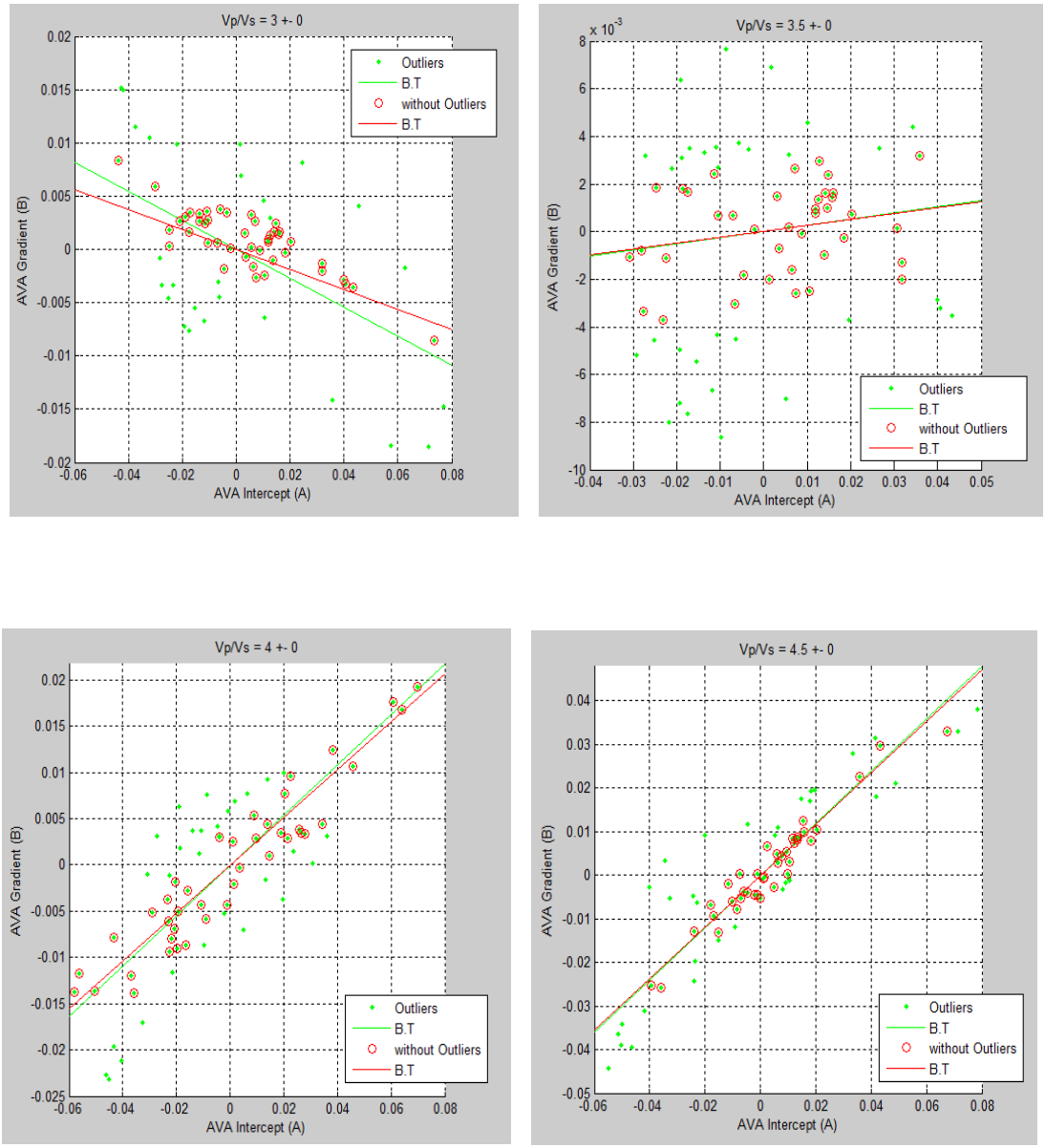

Fig.4.8. Intercept and Gradient values calculated analytically, applying the Shuey's equation to pseudo logs of Vp, Vs and density with the variation of Vp/Vs ratio. The green line represent the slope of the Background Trend with outliers (green points), while, the red line represents the slope of the Background Trend without outliers (point circled in red).

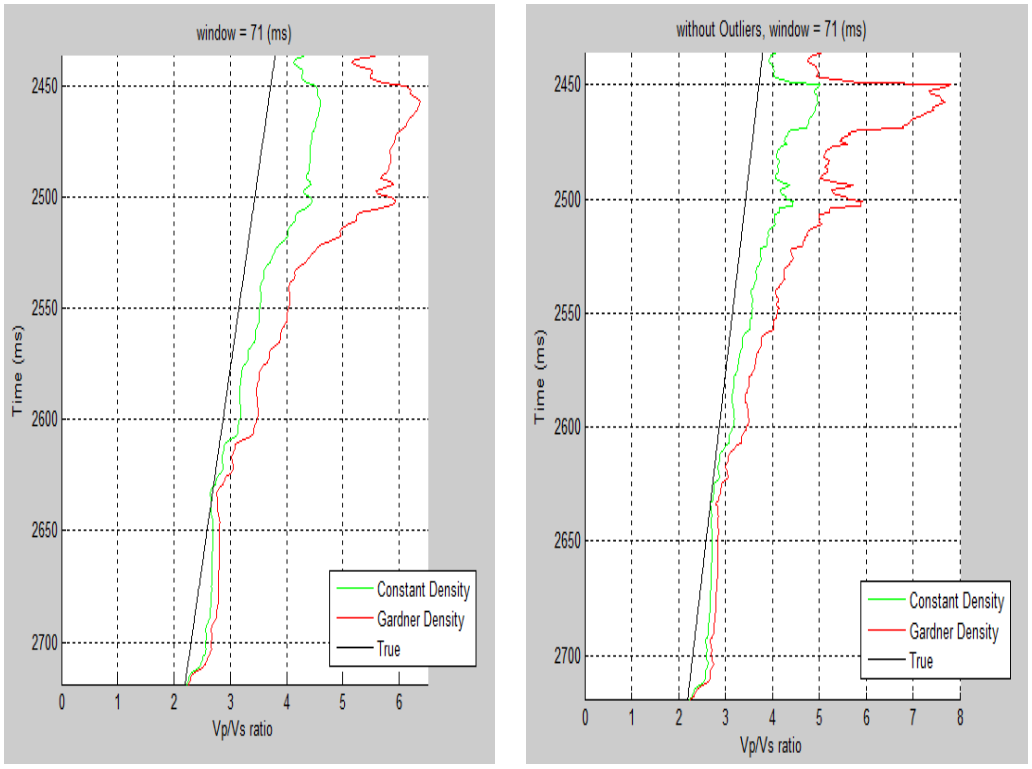

Fig.4.9. Vp/Vs model (left) with outliers, and (right) without outliers. Applying a time window of 71 (ms).

Time window = 91 (ms):

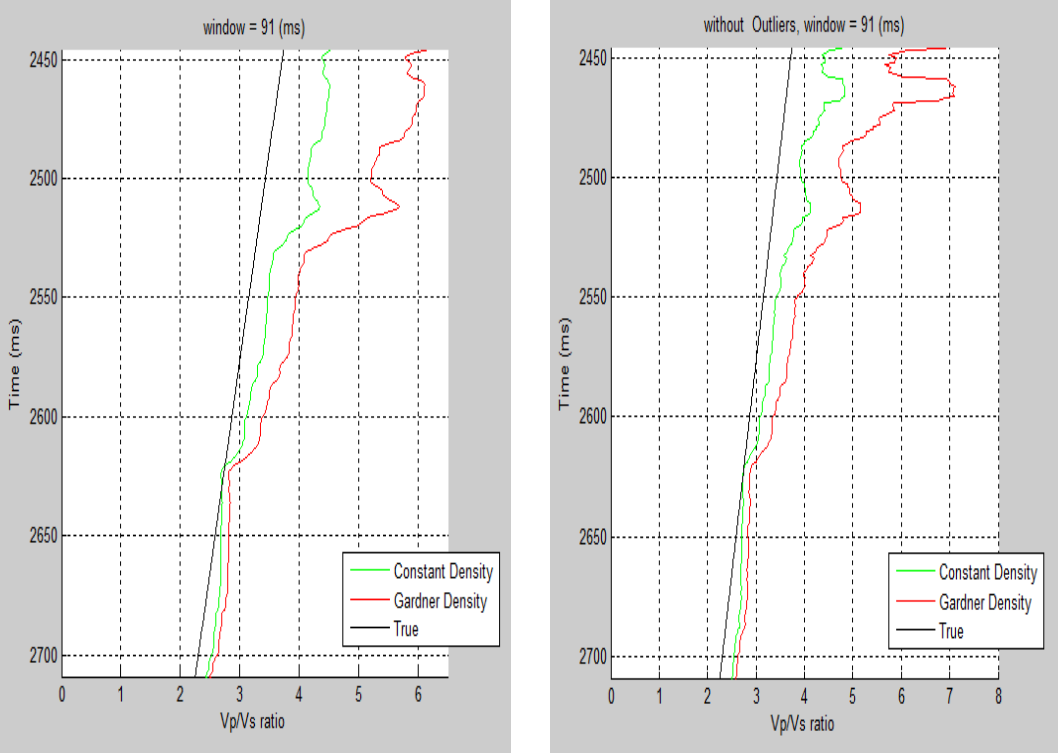

Fig.4.10. Vp/Vs model (left) with outliers, and (right) without outliers. Applying a time window of 91 (ms).

This case the prediction made by the straight line of the Background Trend always overstimate the real Vp/Vs ratio, especially when we consider the Gardner Density.

Considering now the case where the Vp/Vs ratio does not remain constant throughout the interval described by pseudo logs, but varies with a standard deviation of 0.01. It notes that increasing the rate variation of Vp/Vs ratio, it determines a divert of the Vp/Vs values predicted by Background Trend compared to the real values.

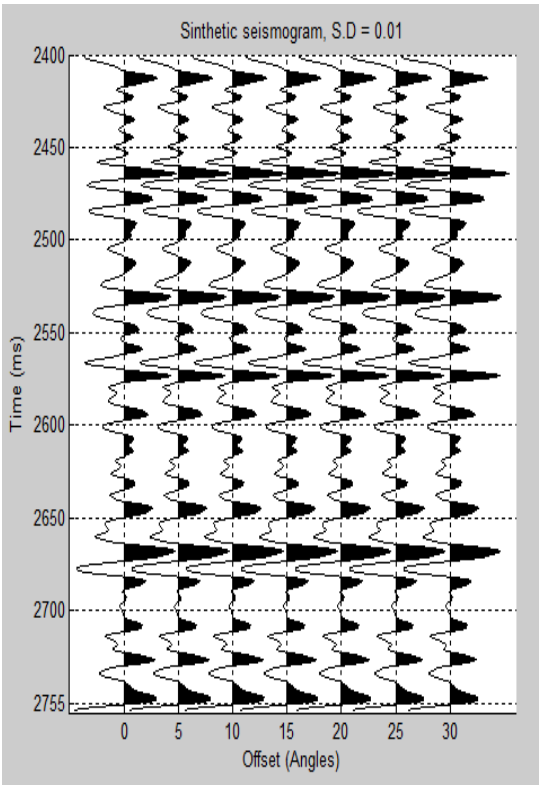

Fig. 4.11. Synthetic seismogram

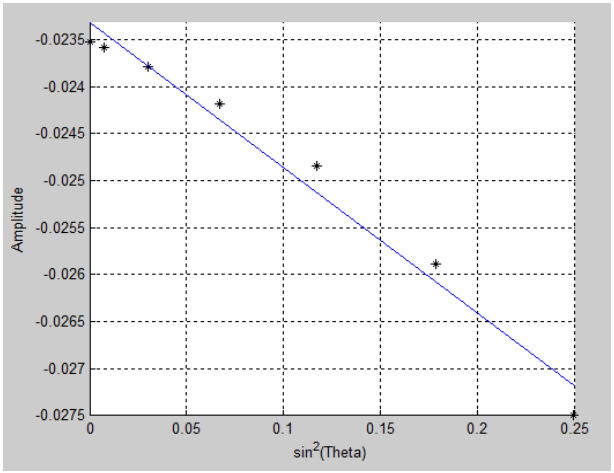

Figure 4.12. Estimated reflection coefficients from the synthetic seismic shown in Figure 4.11. The AVA parameters R_0 and G are computed from linear regression on the data.

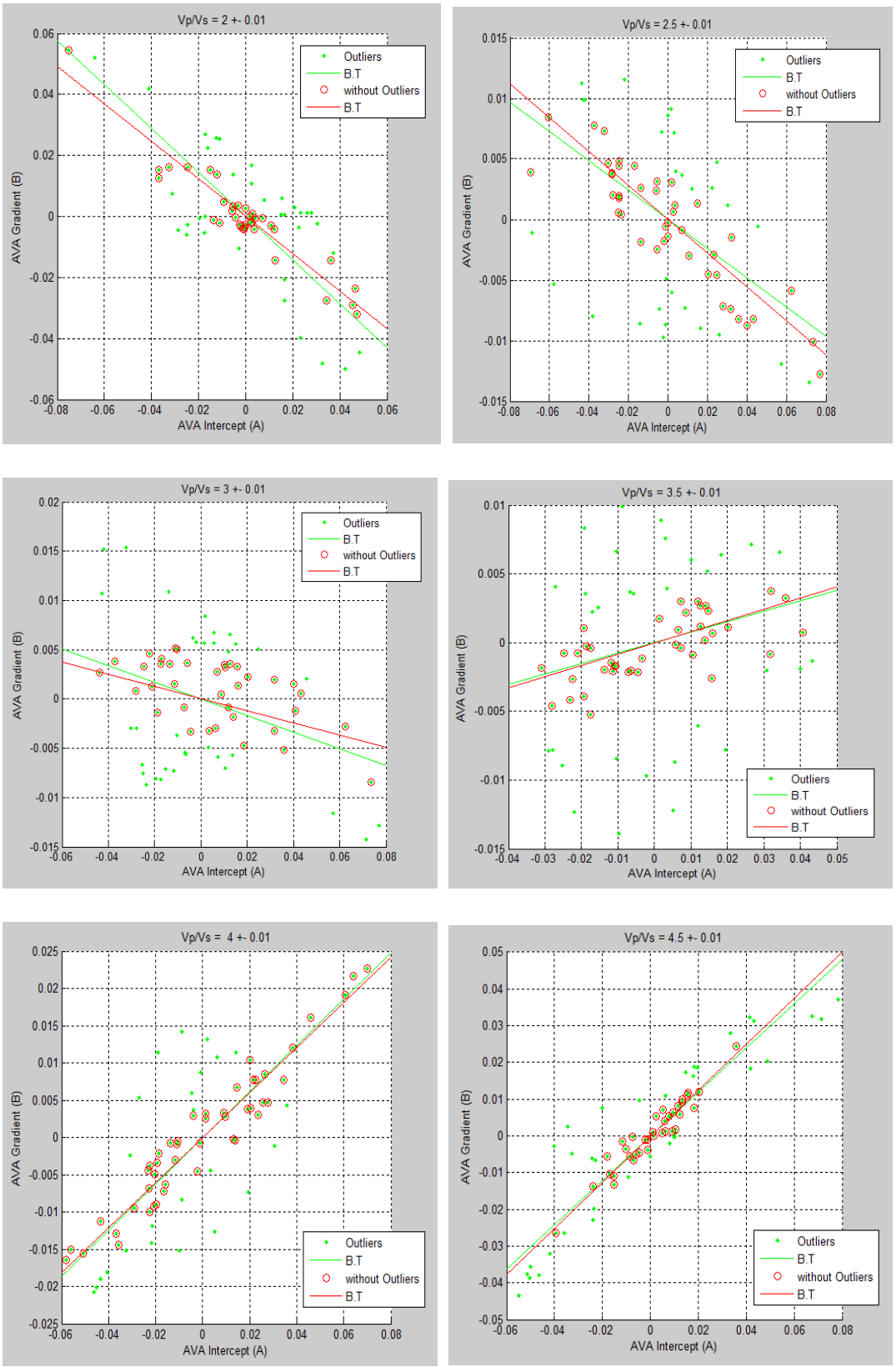

Fig.4.13. Intercept and Gradient values calculated analytically, applying the Shuey's equation to pseudo logs of Vp, Vs and density with the variation of Vp/Vs ratio. The green line represent the slope of the Background Trend with outliers (green points), while, the red line represents the slope of the Background Trend without outliers (point circled in red). With a standard deviation = 0.01.

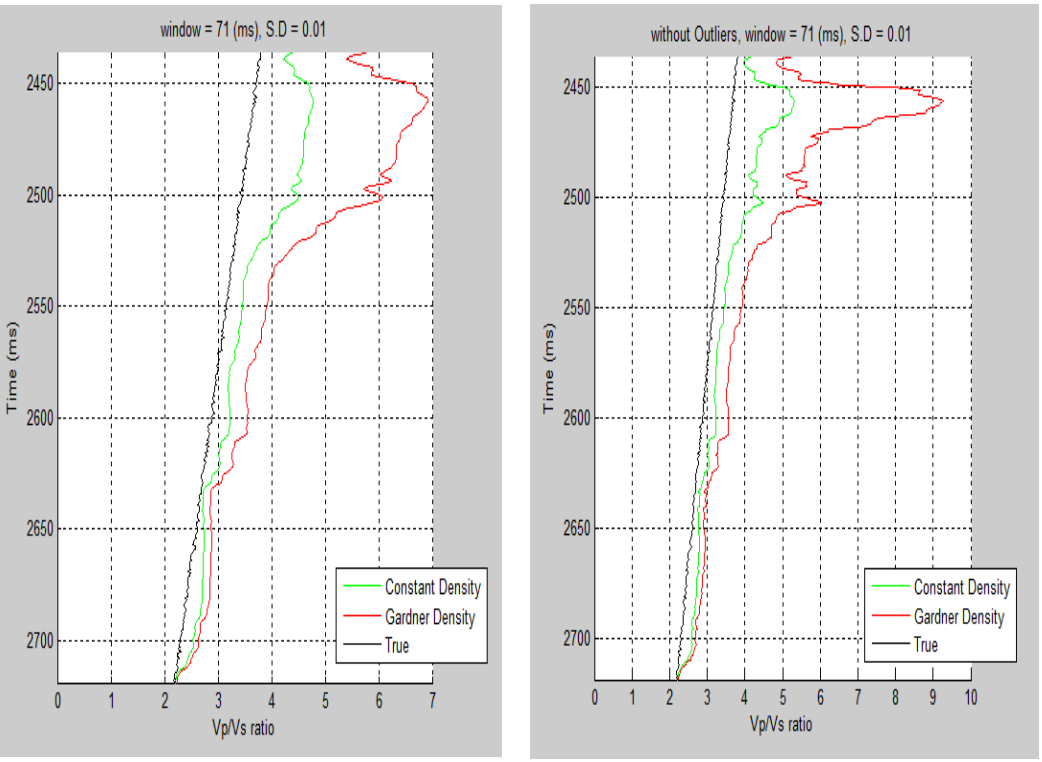

Fig.4.14. Vp/Vs model (left) with outliers, and (right) without outliers. Applying a time window of 71 (ms). Applying a standard deviation = 0.01.

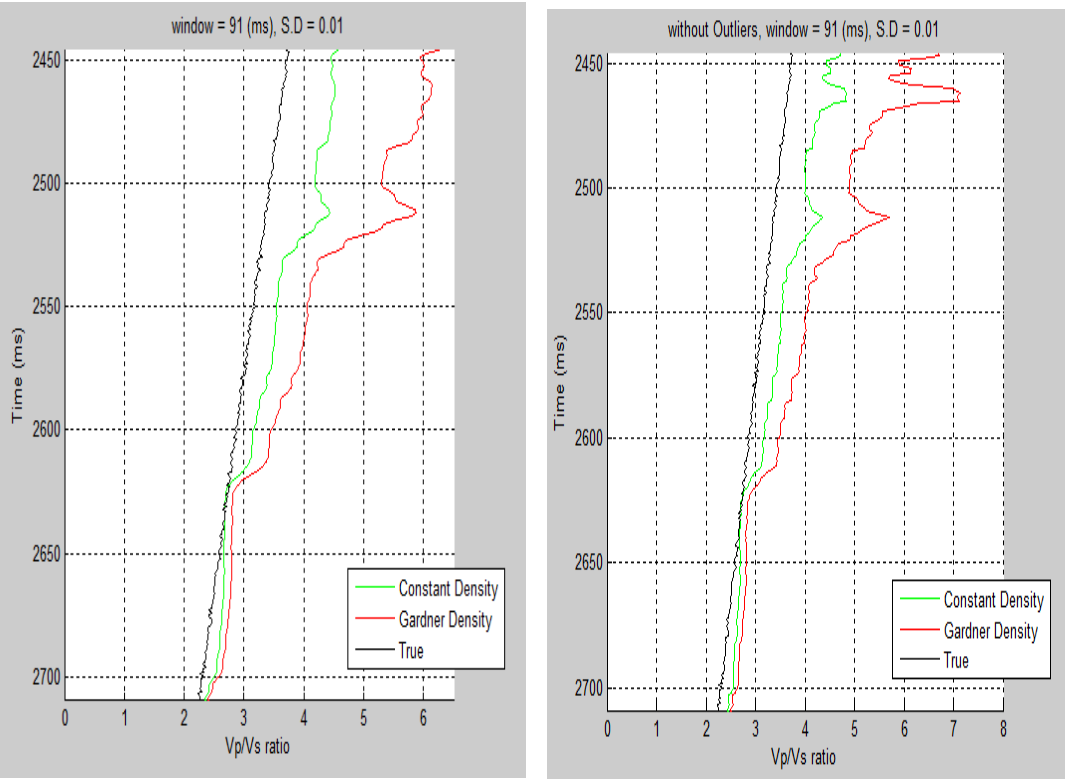

Fig.4.15. Vp/Vs model (left) with outliers, and (right) without outliers. Applying a time window of 91 (ms). Applying a standard deviation = 0.01.

Considering the correct relationship of Vp/Vs ratio, we can see the variations of amplitude with the offset (Angles) on the synthetic seismogram (Mettere il numero della figura). The correct relationship of Vp/Vs always overstimate the Vp/Vs values predicted by Background Trend straight line. It is clear that strong reflections can alter the assessment of Vp/Vs from the slope of the Background Trend.

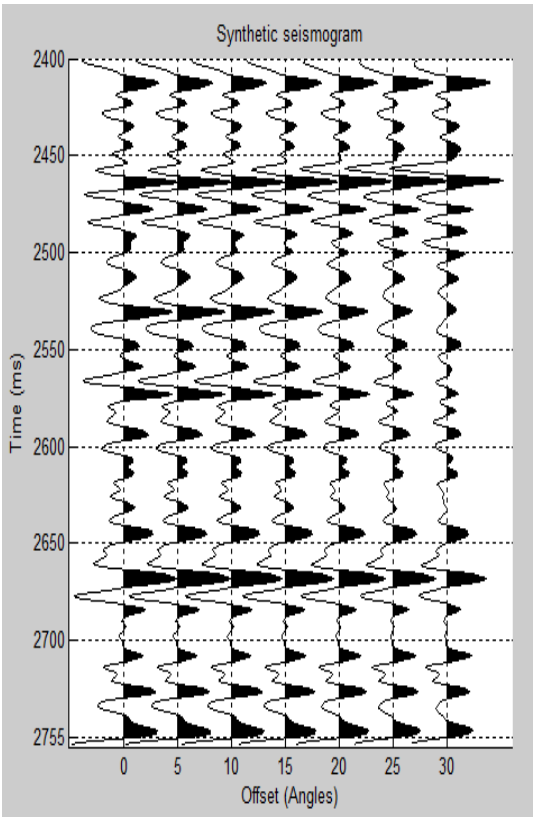

Fig. 4.16. Synthetic seismogram

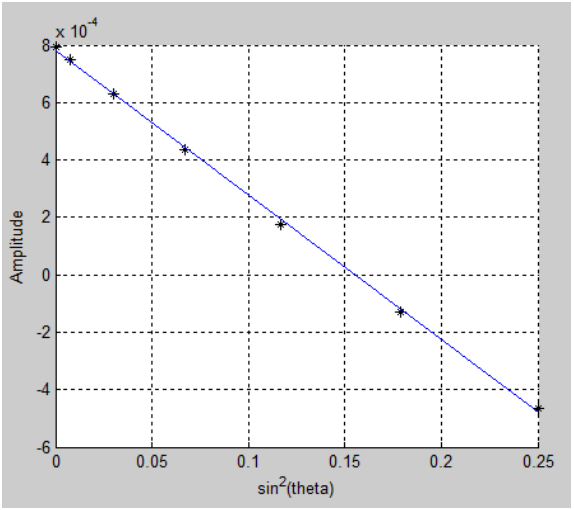

Figure 4.17: Estimated reflection coefficients from the synthetic seismic shown in Figure 4.16. The AVA parameters R_0 and G are computed from linear regression on the data.

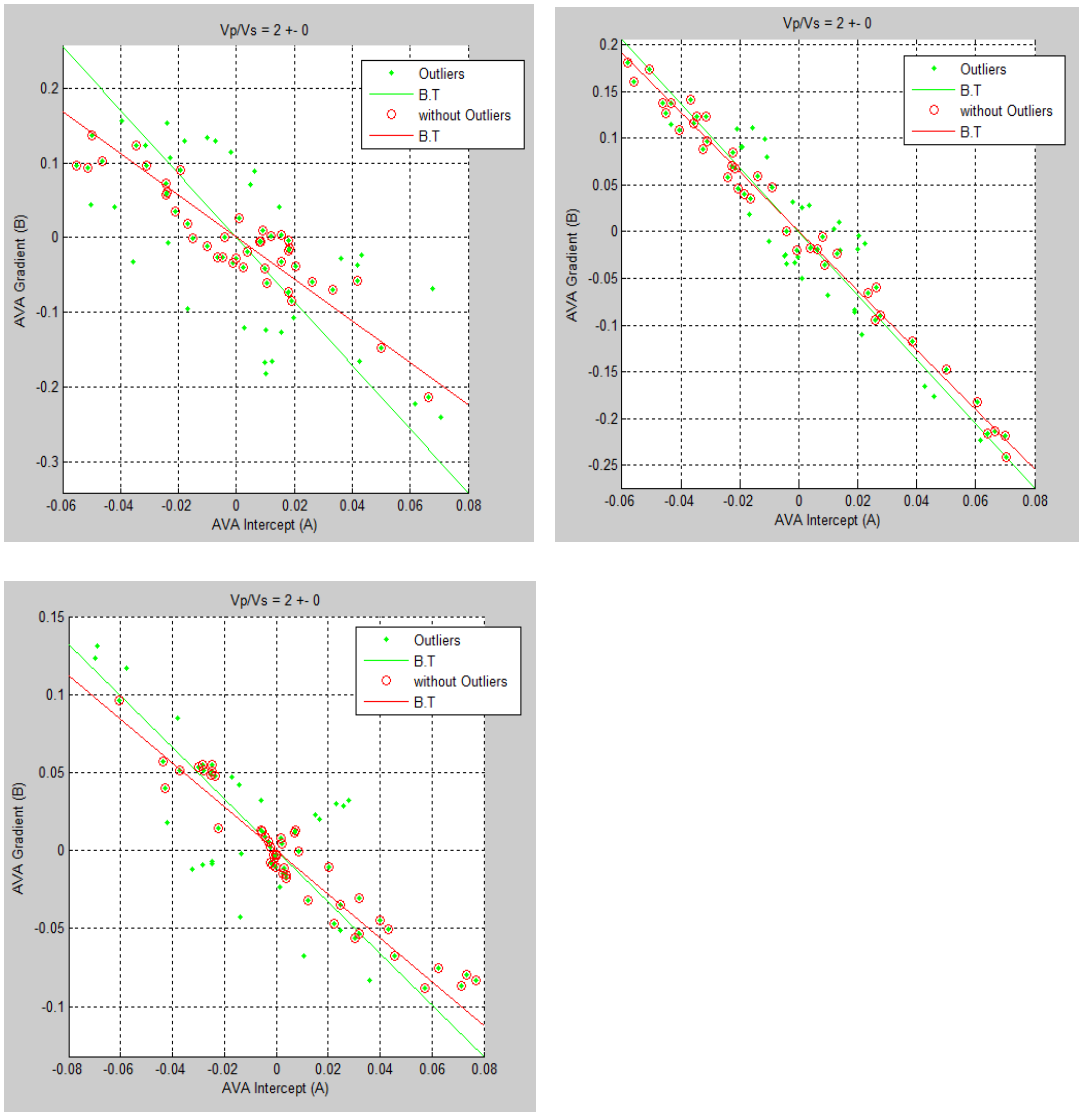

Fig.4.18. Intercept and Gradient values calculated analytically, applying the Shuey's equation to pseudo logs of Vp, Vs and density with the variation of Vp/Vs ratio. The green line represent the slope of the Background Trend with outliers (green points), while, the red line represents the slope of the Background Trend without outliers (point circled in red). With a standard deviation = 0.01

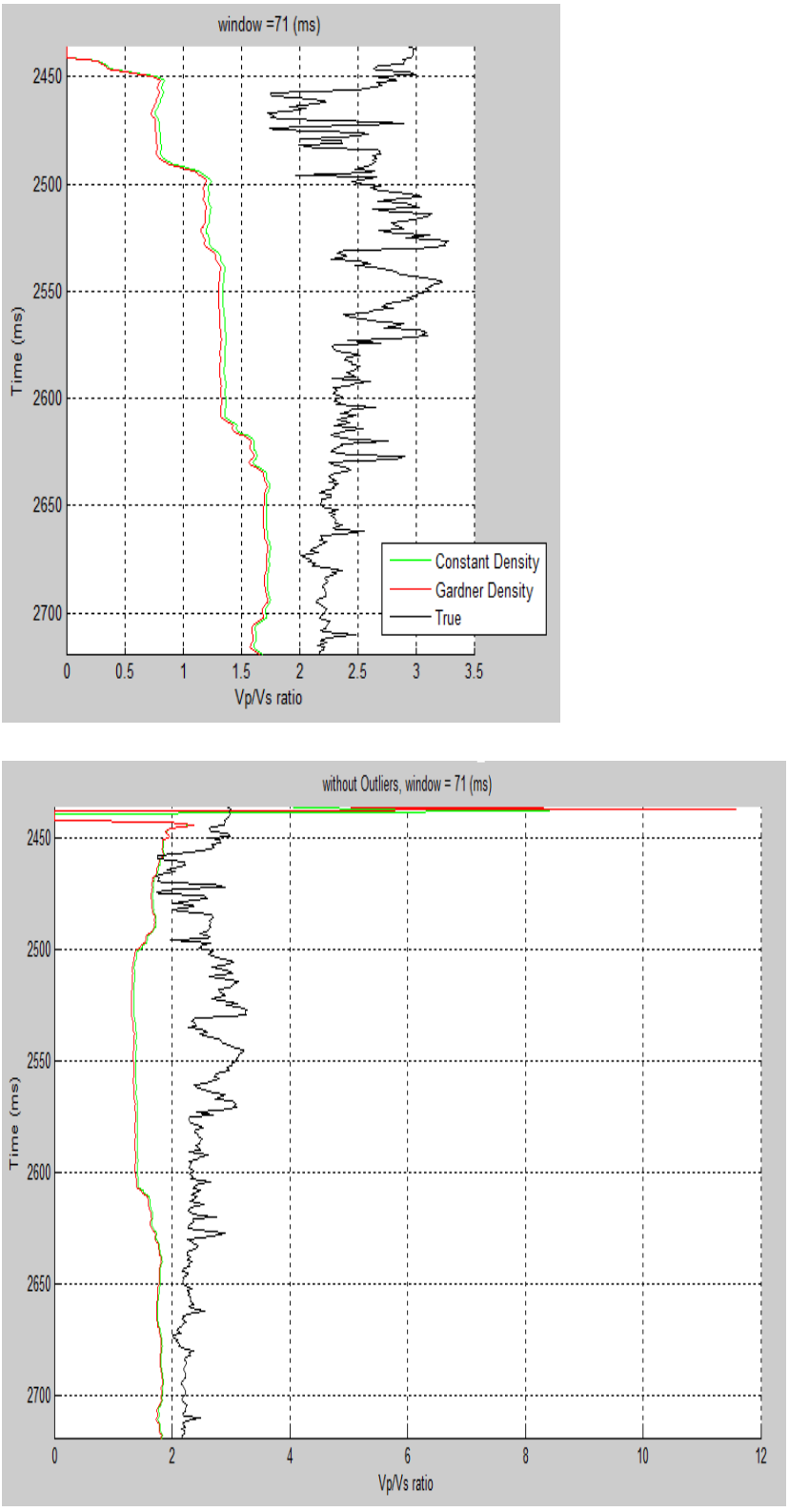

Fig.4.19. Correct relationship of Vp/Vs ratio (top) with outliers, and (bottom) without outliers. Applying a time window of 71 (ms).

4.4 Low Pass filter application

FIR filters are filters having a transfer function of a polynomial in *z*- and is an all-zero filter in the sense that the zeroes in the *z*-plane determine the frequency response magnitude characteristic. The *z* transform of a *N*-point FIR filter is given by

$$H(z) = \sum_{n=0}^{N-1} h(n) z^{-n} \tag{4.15}$$

FIR filters are particularly useful for applications where exact linear phase response is required. The FIR filter is generally implemented in a non-recursive way which guarantees a stable filter. FIR filter design essentially consists of two parts, approximation problem and realization problem.

The approximation stage takes the specification and gives a transfer function through four steps. They are as follows:

A desired or ideal response is chosen, usually in the frequency domain.

An allowed class of filters is chosen (e.g. the length *N* for a FIR filters).

A measure of the quality of approximation is chosen.

A method or algorithm is selected to find the best filter transfer function.

The realization part deals with choosing the structure to implement the transfer function which

may be in the form of circuit diagram or in the form of a program.

There are essentially three well-known methods for FIR filter design namely:

(1) The window method

(2) The frequency sampling technique

(3) Optimal filter design methods

The window Method

In this method, [Park87], [Rab75], [Proakis00] from the desired frequency response specification *Hd* (*w*), corresponding unit sample response *hd*(*n*) is determined using the following relation

$$h_d(n)=\frac{1}{2\pi}\int_{-\pi}^{\pi}H_d(w)e^{jwn}dw$$

$$H_d(w)=\sum_{n=-\infty}^{\infty}h_d(n)e^{-jwn} \qquad (4.16)$$

In general, unit sample response *hd*(*n*) obtained from the above relation is infinite in duration, so it must be truncated at some point say *n*= *M*-1 to yield an FIR filter of length *M* (i.e. 0 to *M*-1). This truncation of *hd*(*n*) to length *M*-1 is same as multiplying *hd*(*n*) by the rectangular window defined as

$$w(n) = \begin{cases} 1 & < n > M\text{-}1 \\ 0 & \text{otherwise} \\ 1 & \end{cases}$$

Thus the unit sample response of the FIR filter becomes

$$\begin{aligned} h(n) &= hd(n)\, w(n) \\ &= hd(n) \qquad < n < M\text{-}1 \\ &= 0 \qquad\quad \text{otherwise} \end{aligned}$$

Now, the multiplication of the window function *w*(*n*) with *hd*(*n*) is equivalent to convolution of *Hd*(*w*) with *W*(*w*), where *W*(*w*) is the frequency domain representation of the window function

$$W(w)=\sum_{n=0}^{M-1}w(n)e^{-jwn} \qquad (4.17)$$

Thus the convolution of *Hd*(*w*) with *W*(*w*) yields the frequency response of the truncated FIR Filter

$$H(w) = \frac{1}{2\pi} \int_{-\pi}^{\pi} H_d(v) W(w-v) dw \tag{4.18}$$

The frequency response can also be obtained using the following relation

$$H(w) = \sum_{n=0}^{M-1} h(n) e^{-jwn} \tag{4.19}$$

But direct truncation of *hd*(*n*) to *M* terms to obtain *h*(*n*) leads to the Gibbs phenomenon effect which manifests itself as a fixed percentage overshoot and ripple before and after an approximated discontinuity in the frequency response due to the non-uniform convergence of the fourier series at a discontinuity.Thus the frequency response obtained by using contains ripples in the frequency domain. In order to reduce the ripples, instead of multiplying *hd*(*n*) with a rectangular window *w*(*n*), *hd*(*n*) is multiplied with a window function that contains a taper and decays toward zero gradually, instead of abruptly as it occurs in a rectangular window. As multiplication of sequences hd(n) and *w*(*n*) in time domain is equivalent to convolution of *Hd*(*w*) and *W*(*w*) in the frequency domain, it has the effect of smoothing *Hd*(*w*). The several effects of windowing the Fourier coefficients of the filter on the result of the frequency response of the filter are as follows:

A major effect is that discontinuities in *H*(*w*) become transition bands between values on either side of the discontinuity.

The width of the transition bands depends on the width of the main lobe of the frequency response of the window function, *w*(*n*) and *W*(*w*).

Since the filter frequency response is obtained via a convolution relation , it is clear that the resulting filters are never optimal in any sense.

As *M* (the length of the window function) increases, the mainlobe width of *W*(*w*) is reduced which reduces the width of the transition band, but this also introduces more ripple in the frequency response.

The window function eliminates the ringing effects at the bandedge and does result in lower sidelobes at the expense of an increase in the width of the transition band of the filter.

4.6 AVA Forward Modelling with Low Pass-filter Application

To improve the assesment of Vp/Vs ratio from the slope of the Background Trend straight line, it has tried out the effects of the application of low-pass filter to extract low frequency trends. It has applied a low pass filter with a cut-off frequency of 10 Hz. The frequencies above 10 Hz have been removed. Considering the simplest case where Vp/Vs ratio remains constant throughout by pseudo logs. The filter application on the seismogram, it improves the Vp/Vs predicted. It shows the effect which filter application on synthetic seismogram in AVA crossplot. In AVA crossplot there are Intercept and Gradient points (CIRCLED IN BLACK) representing wavelet side lobes (not geology). Another factor to consider during the interpretation of AVA crossplot is the signal-to-noise ratio (S/N) issues which tend to broaden the Intercept and Gradient reflectivity points within crossplot space into oval distributions. This oval distributions is more evident when Vp/Vs ratio varies a standard deviation of 0.01. In this case the AVA crossplot response becomes an oval distribution of points around the real location (the S/N decrease with offset) This is due to the sensitivity of the Gradient estimation to noise. This noise trend is easily recognized on real date, for example by crossplotting limited number of samples from the same horizon from a seismic section.

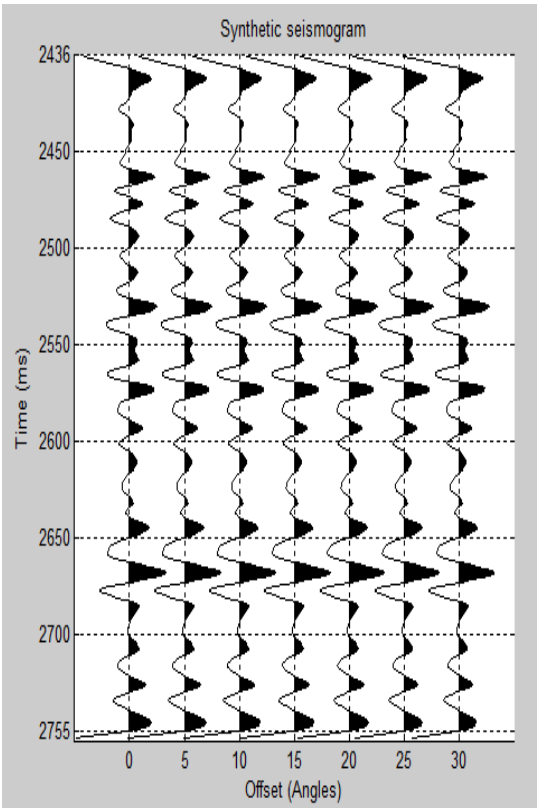

Fig. 4.20. Synthetic seismogram

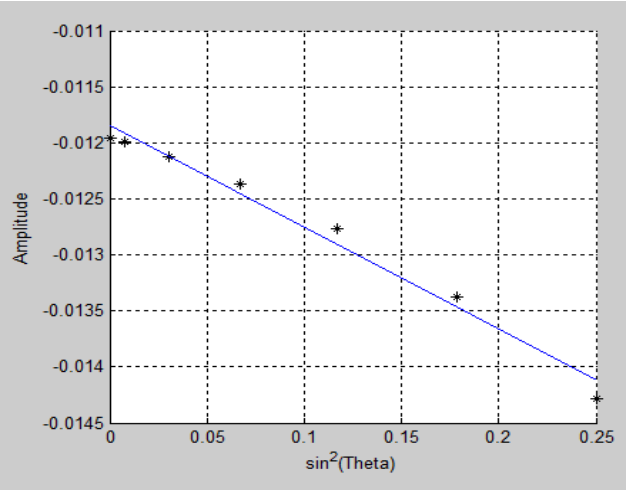

Figure 4.21: Estimated reflection coefficients from the synthetic seismic shown in Figure 4.20. The AVA parameters R_0 and G are computed from linear regression on the data.

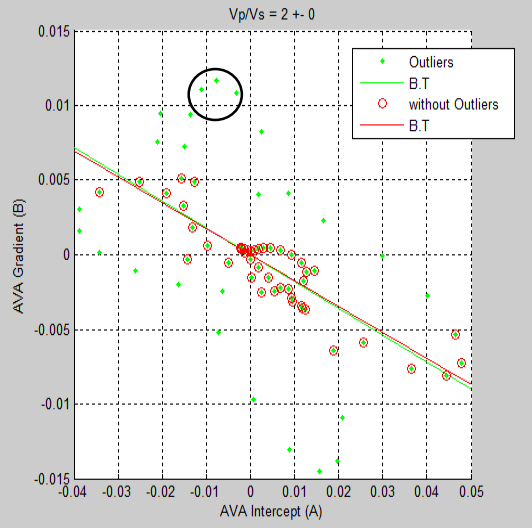
Vp/Vs = 2 +- 0
Outliers
B.T
without Outliers
B.T
AVA Gradient (B)
AVA Intercept (A)

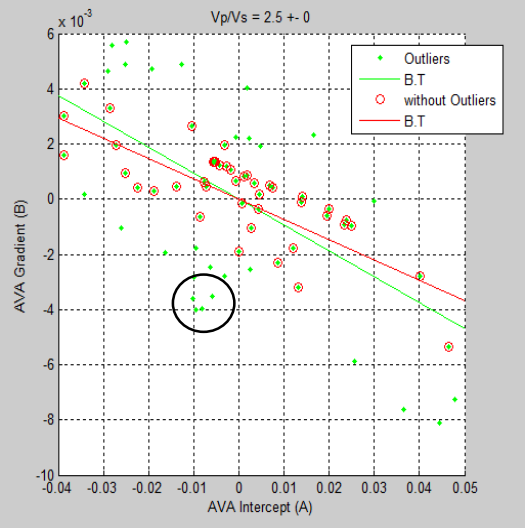
x 10^-3
Vp/Vs = 2.5 +- 0
Outliers
B.T
without Outliers
B.T
AVA Gradient (B)
AVA Intercept (A)

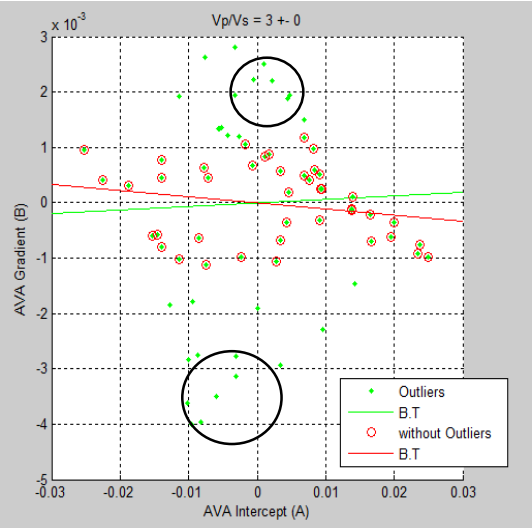
x 10^-3
Vp/Vs = 3 +- 0
Outliers
B.T
without Outliers
B.T
AVA Gradient (B)
AVA Intercept (A)

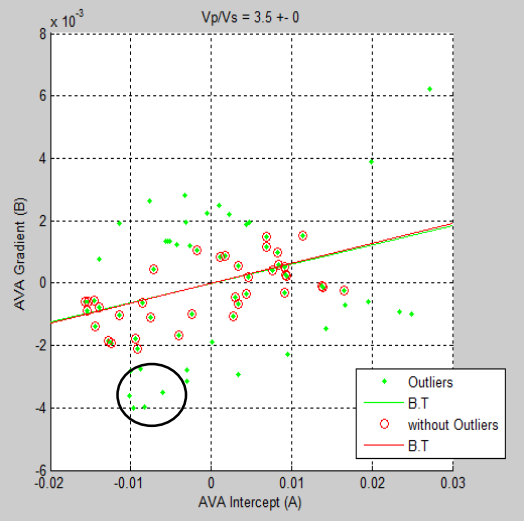
x 10^-3
Vp/Vs = 3.5 +- 0
Outliers
B.T
without Outliers
B.T
AVA Gradient (B)
AVA Intercept (A)

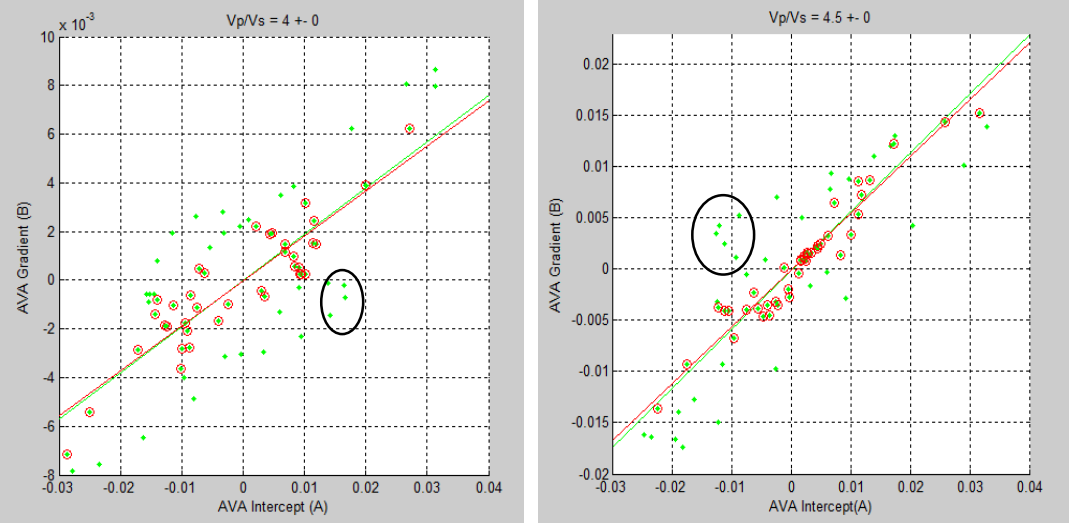

Fig.4.22. Intercept and Gradient values calculated analytically, applying the Shuey's equation to pseudo logs of Vp, Vs and density with the variation of Vp/Vs ratio. The green line represent the slope of the Background Trend with outliers (green points), while, the red line represents the slope of the Background Trend without outliers (point circled in red).

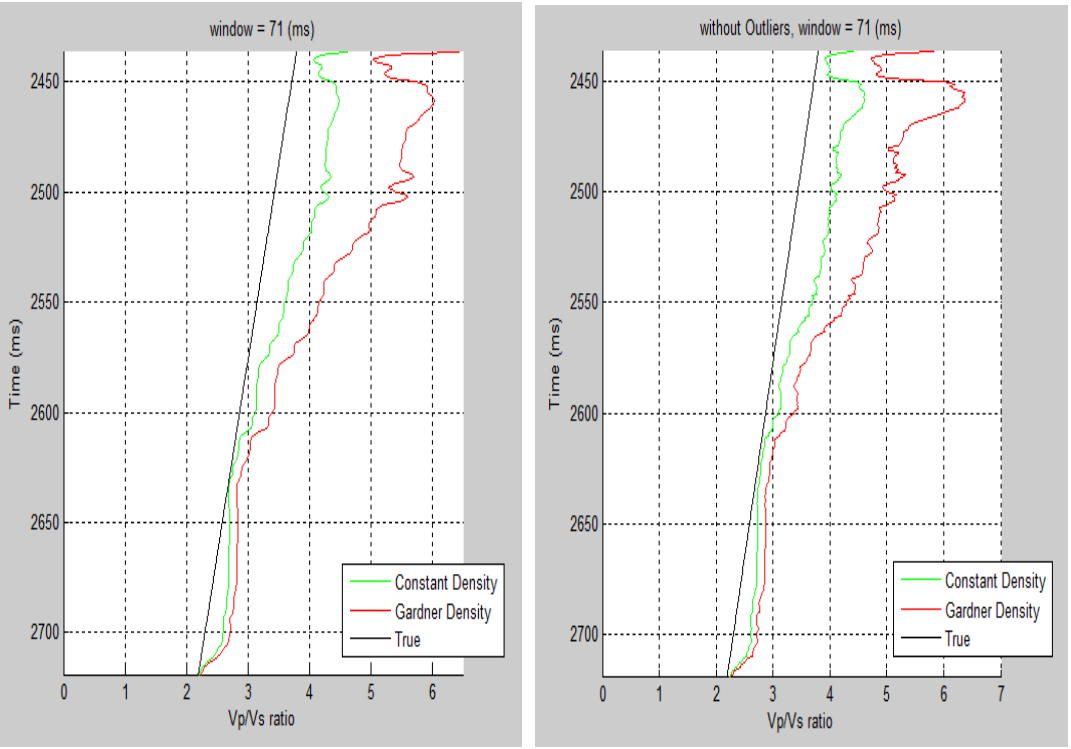

Fig.4.23. Vp/Vs model (left) with outliers, and (right) without outliers. Applying a time window of 71 (ms).

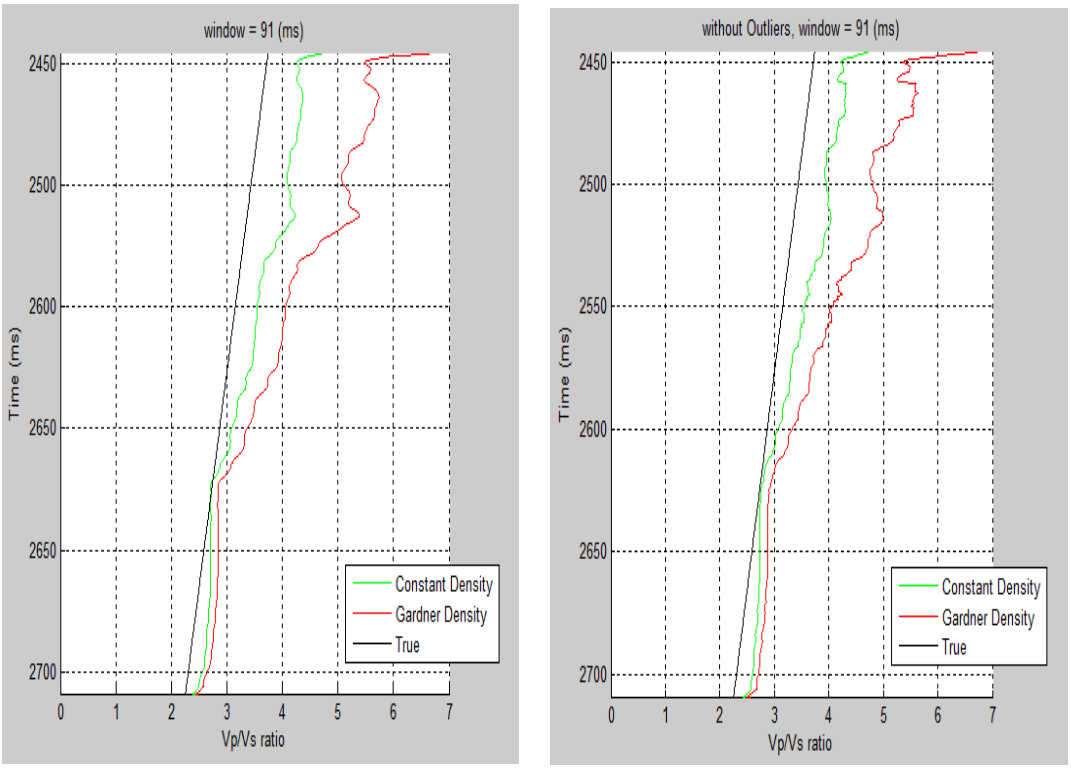

Fig.4.24. Vp/Vs model (left) with outliers, and (right) without outliers. Applying a time window of 91 (ms).

Applying a standard deviation = 0.01.

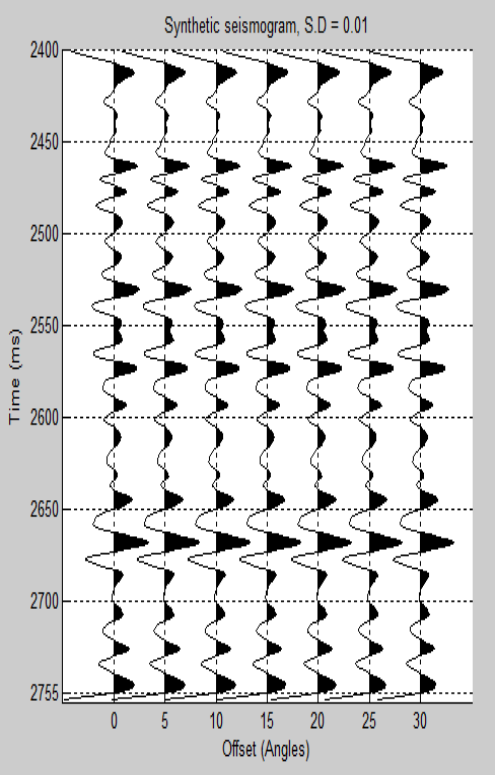

Fig. 4.25. Synthetic seismogram

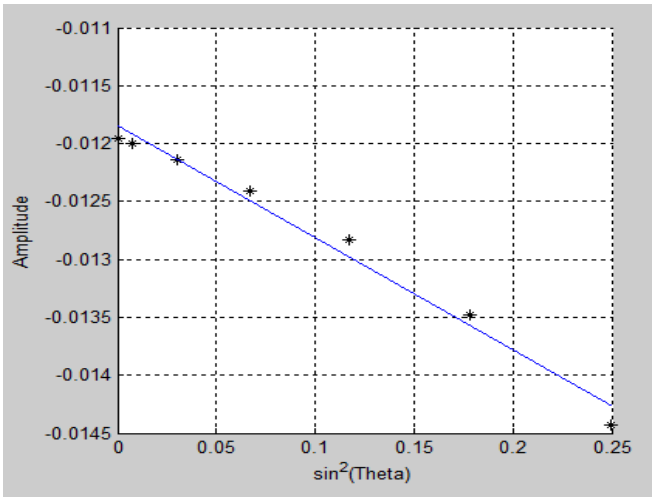

Figure 4.26: Estimated reflection coefficients from the synthetic seismic shown in Figure 4.25. The AVA parameters R_0 and G are computed from linear regression on the data.

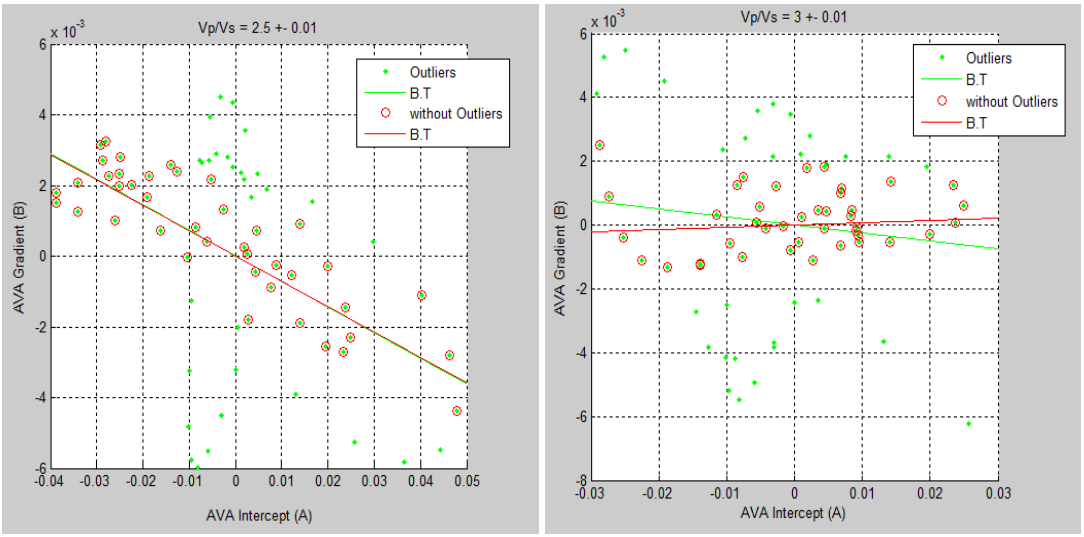

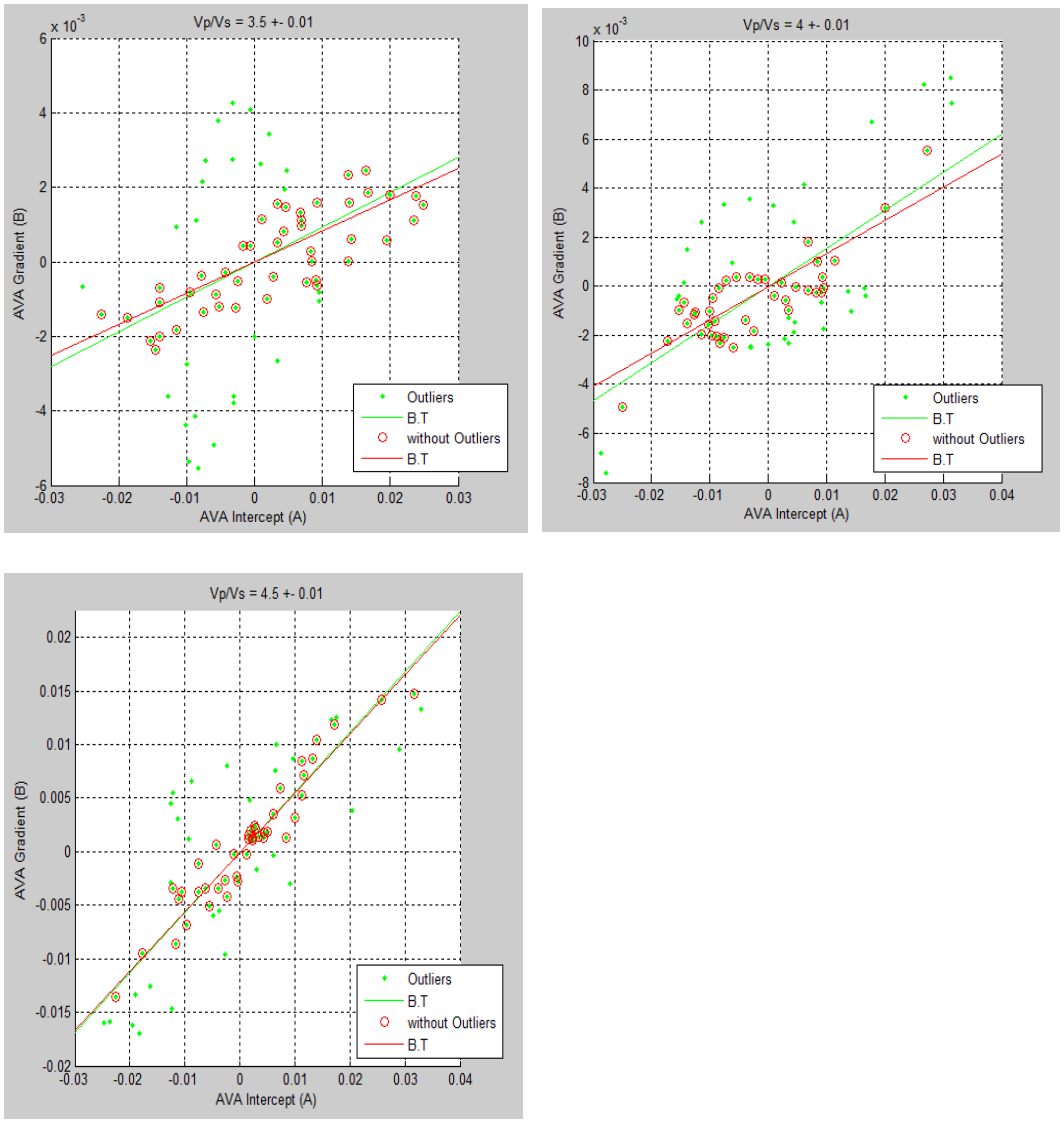

Fig.4.27. Intercept and Gradient values calculated analytically, applying the Shuey's equation to pseudo logs of Vp, Vs and density with the variation of Vp/Vs ratio. The green line represent the slope of the Background Trend with outliers (green points), while, the red line represents the slope of the Background Trend without outliers (point circled in red). We can note, in this case the Vp/Vs ratio changes with a standard deviation = 0.01.

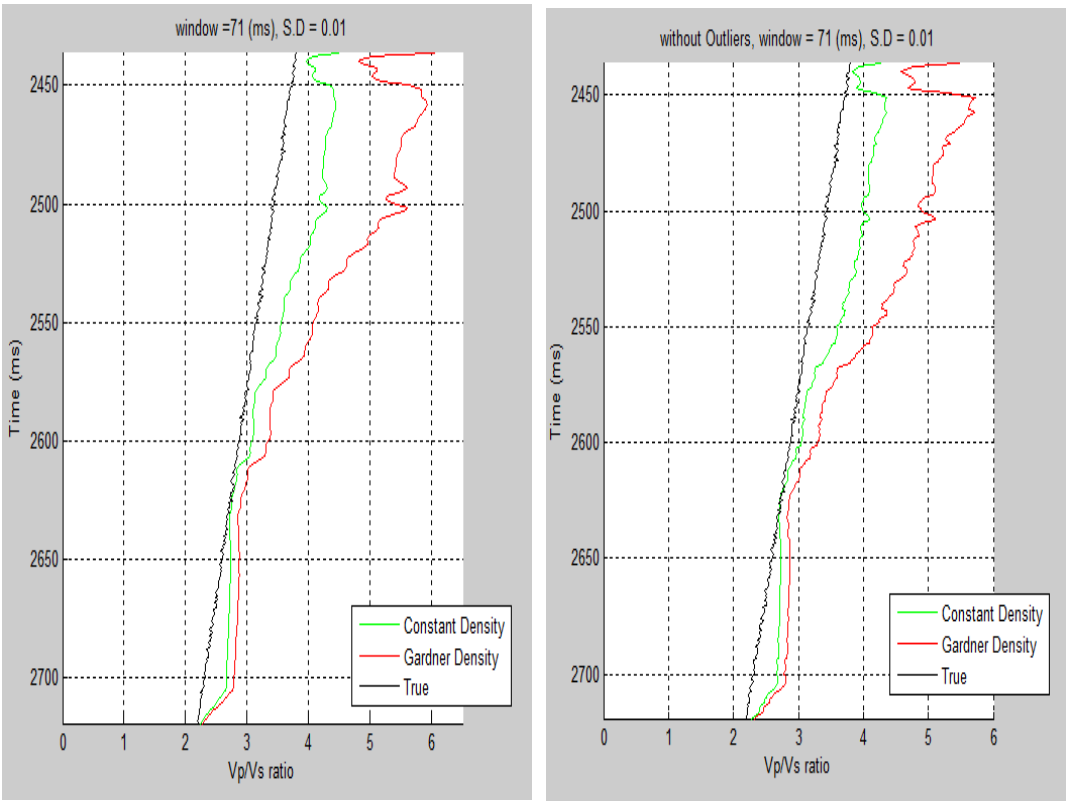

Fig.4.28. Vp/Vs model (left) with outliers, and (right) without outliers. Applying a time window of 71 (ms).

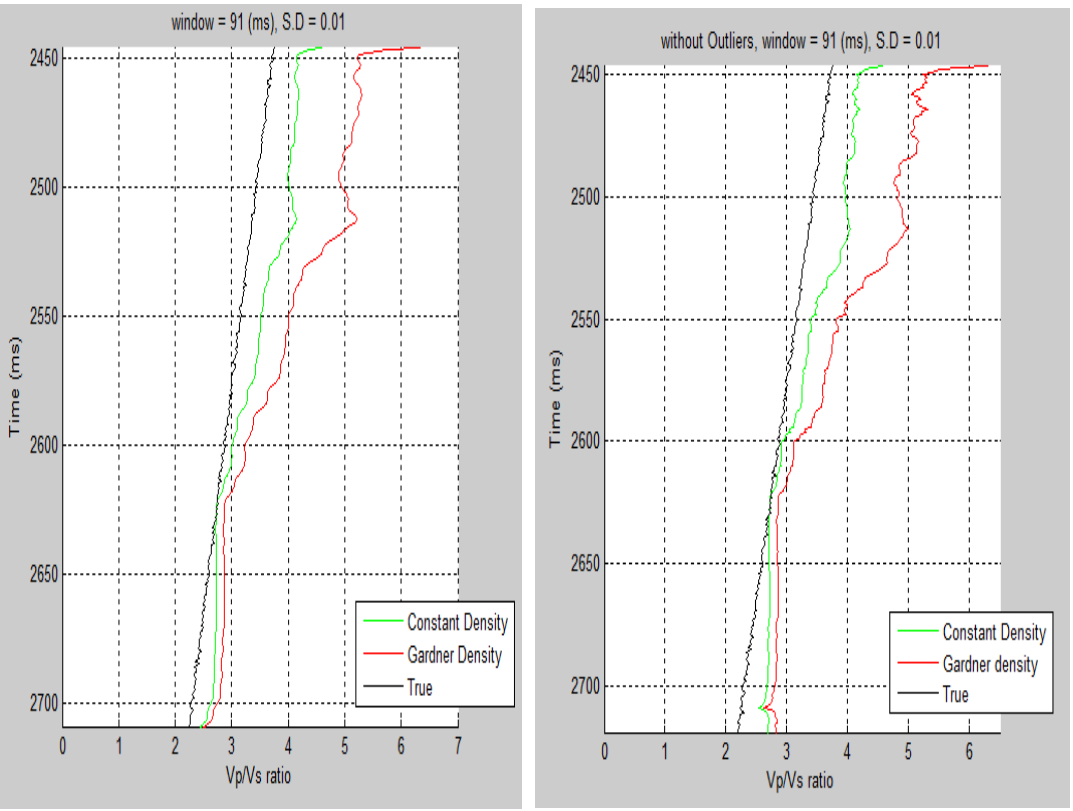

Fig. 4.29. Vp/Vs model (left) with outliers, and (right) without outliers. Applying a time window of 91 (ms).

Correct relationship of Vp/Vs ratio:

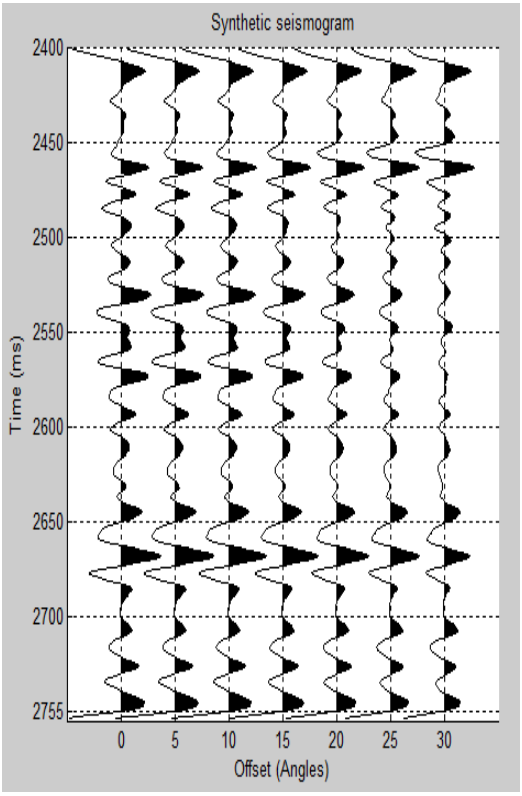

Fig. 4.30. Synthetic seismogram

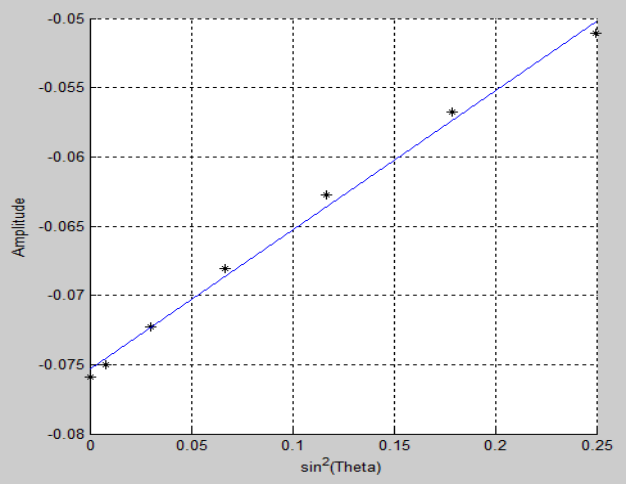

Figure 4.31. Estimated reflection coefficients from the synthetic seismic shown in Figure 4.30. The AVA parameters R_0 and G are computed from linear regression on the data.

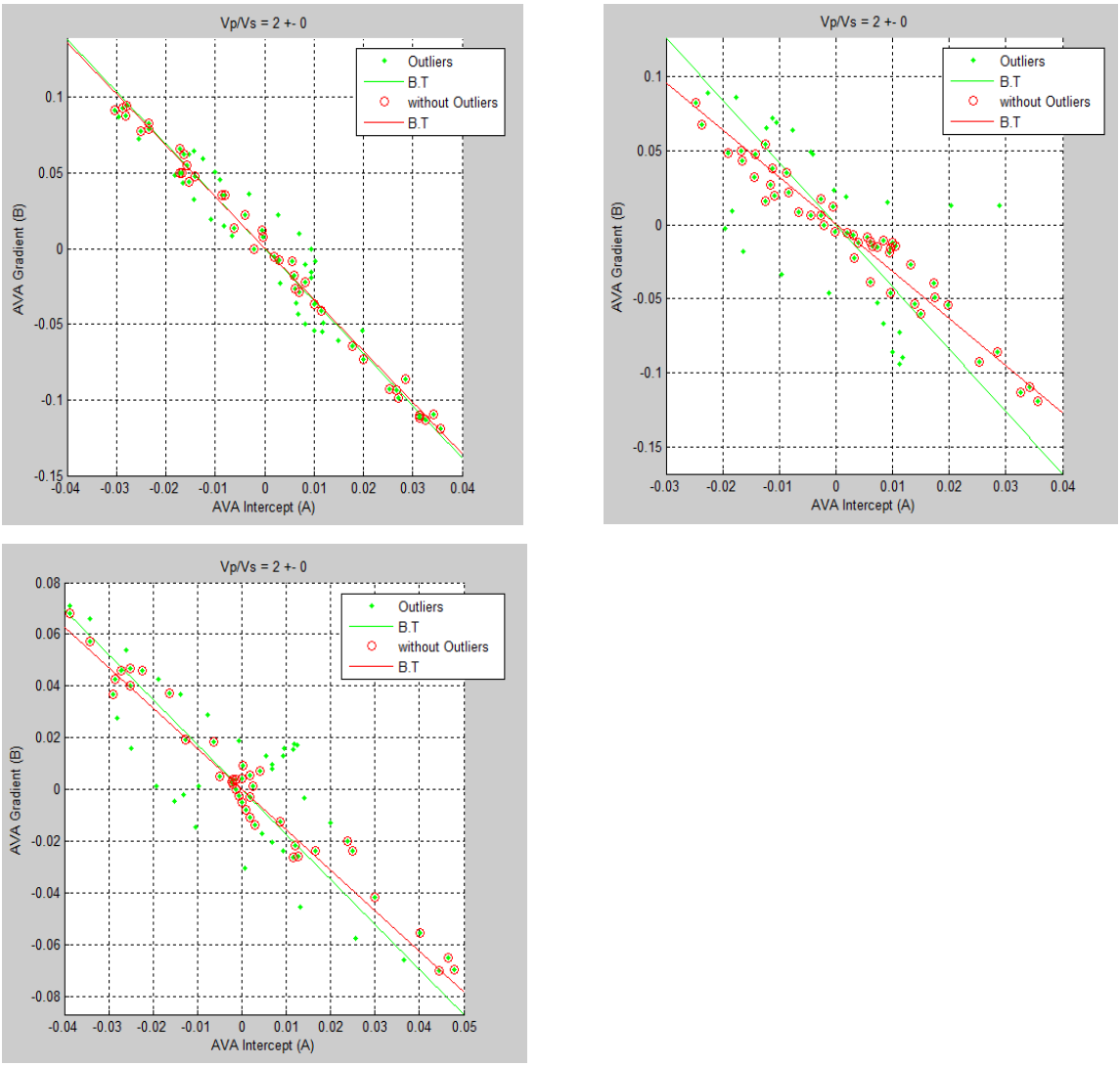

Fig.4.32. Intercept and Gradient values calculated analytically, applying the Shuey's equation to pseudo logs of Vp, Vs and density with the variation of Vp/Vs ratio. The green line represent the slope of the Background Trend with outliers (green points), while, the red line represents the slope of the Background Trend without outliers (point circled in red). We can note, in this case the Vp/Vs ratio changes with a standard deviation = 0.01.

The correct relationship of Vp/Vs always overstimate the Vp/Vs values predicted by Background Trend straight line. It is clear that strong reflections can alter the assessment of Vp/Vs from the slope of the Background Trend.

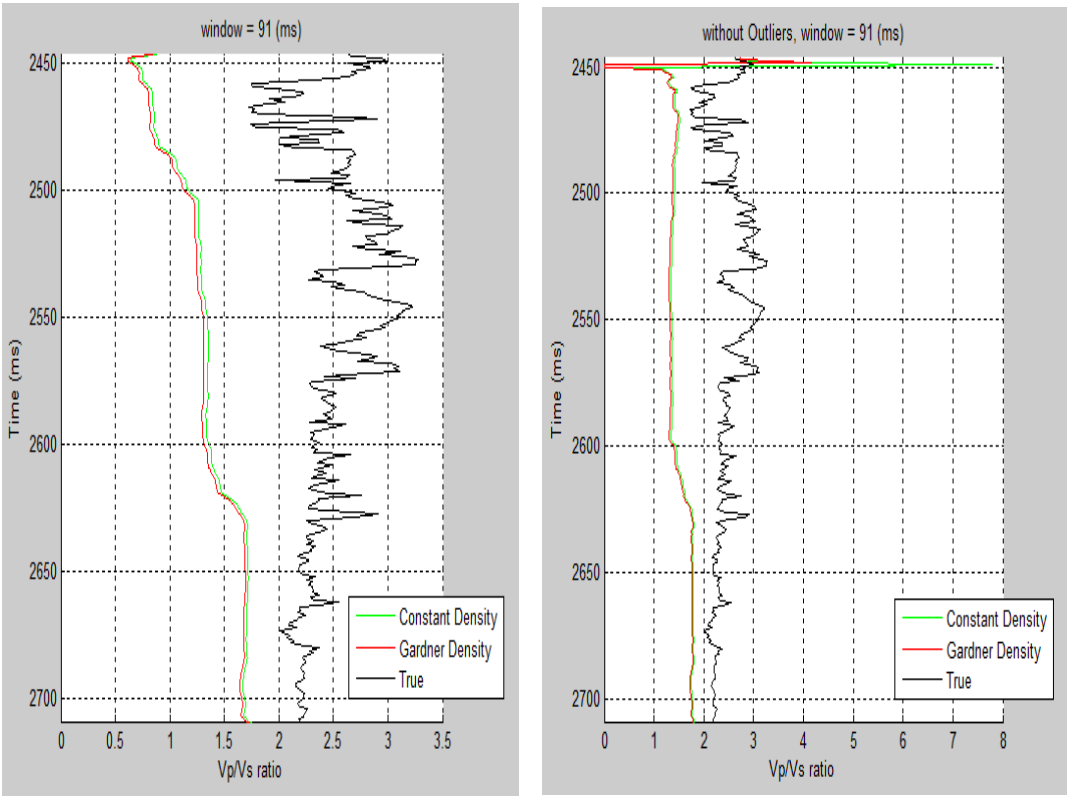

Fig.4.33. Vp/Vs model (left) with outliers, and (right) without outliers. Applying a time window of 91 (ms).

The fourth example considered a ratio Vp/Vs that varied linearly from 4 to 2 and then returned again to a ratio of Vp/Vs = 4, with a standard deviation of 0.01. In the Vp/Vs (Poisson's ratio) different depth trend, it considers the positive deviation as indicator of overpressure. In the interval from 2800 to 3000 (ms), where it has observed an abnormally high Vp/Vs depth trend, it may interpret this interval as an overpressure interval. Poisson's ratio decrease with depth in the first 2800 ms of the interval and then starts to gradually increase due to overpressure.

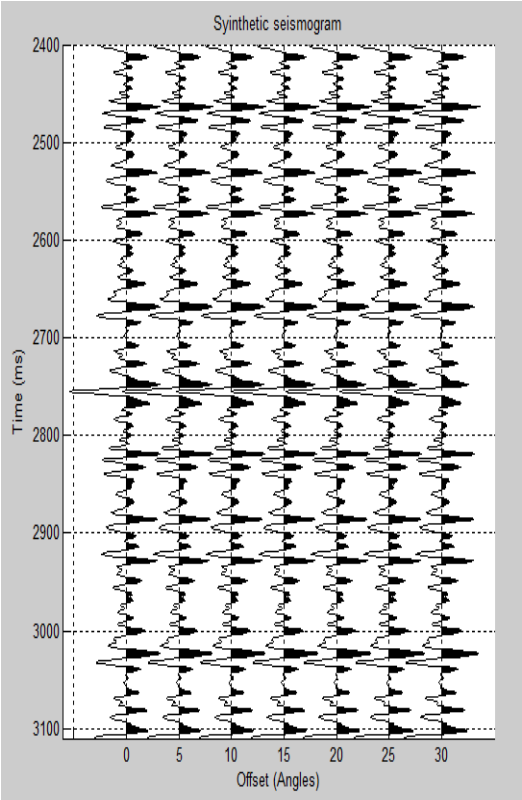

Fig. 4.34. Synthetic seismogram

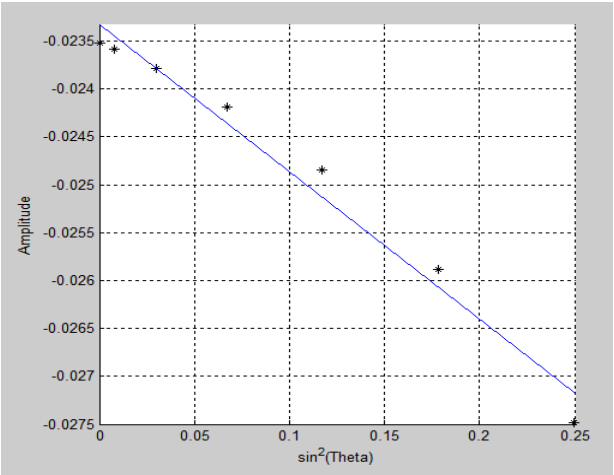

Figure 4.35. Estimated reflection coefficients from the synthetic seismic shown in Figure 4.34. The AVA parameters R_0 and G are computed from linear regression on the data.

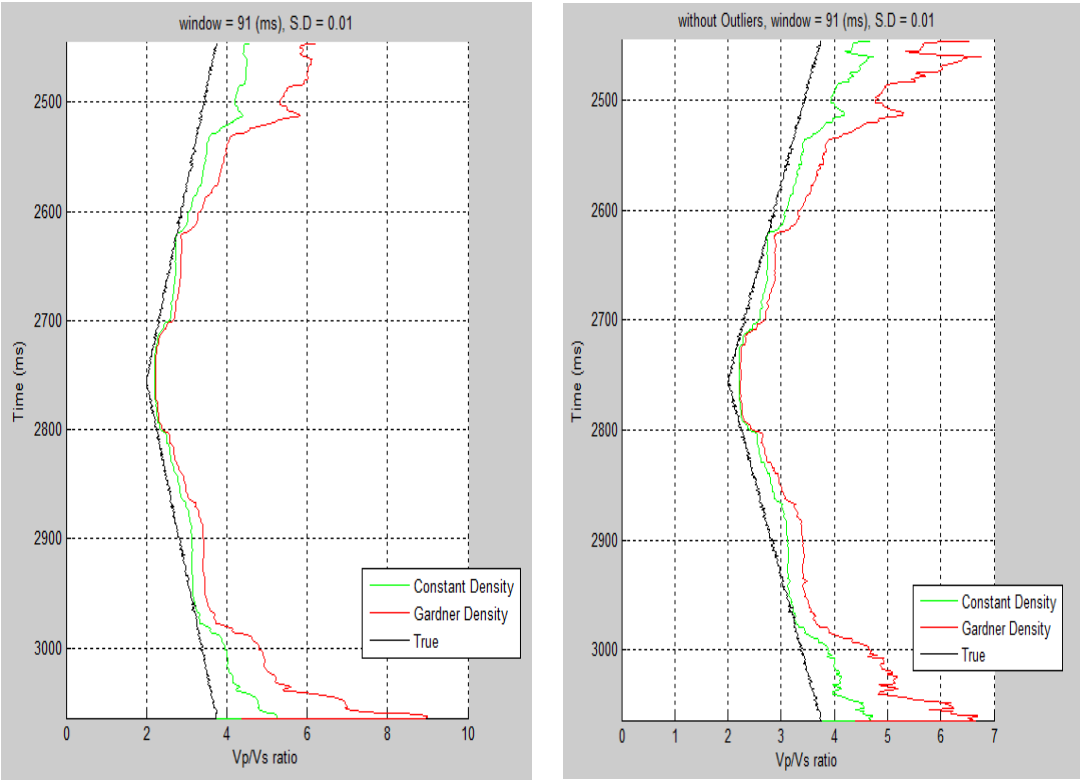

Fig. 4.36. Vp/Vs model (left) with outliers, and (right) without outliers. Applying a time window of 91 (ms).

Chapter 5

Closing remarks

Pore pressure prediction is becoming even more critical to successful drilling as conditions for exploration and exploitation of oil and gas reserve move into more hostile enviroments. In this present study I investigate the effects of changes in rocks and fluid properties on amplitude-variation with angle (AVA). AVA methodology has been used to predict anomalous pressure values directly from seismic data. I have presented in this work AVA attribute that can be used to evidence the anomalies associated to overpressured formations. The AVA attribute was derived from Intercept and Gradient values computed by Shuey equation. I have presented in this work AVA attribute that can be used to evidence the anomalues associated to overpressured formations. The AVA attribute was derived from the Intercept and Gradient values computed by Shuey equation.

This work that is based on 1-D seismic data of empirical case study using well logs and seismic data, demonstrates that AVA is a suitable method in exploitation of overpressure zones using AVO attributes, especially the intercept and gradient. In this work, I have compared an Analytical and Experimental response. In all examples shown, these attributes don't show anomalous responses in correspondence to overpressured layers, except one, when it considered a ratio Vp/Vs that varied linearly from 4 to 2 and then returned again to a ratio of Vp/Vs = 4, with a standard deviation of 0.01.

I compare the Analytical and Experimental Response:

In the examples shown, when I consider the Vp/Vs ratio remains costant throughout the interval described by pseudo logs (in the Experimental and Analytical response), the Gardner Density always shows a Vp/Vs ratio greater than the Gardner Density.

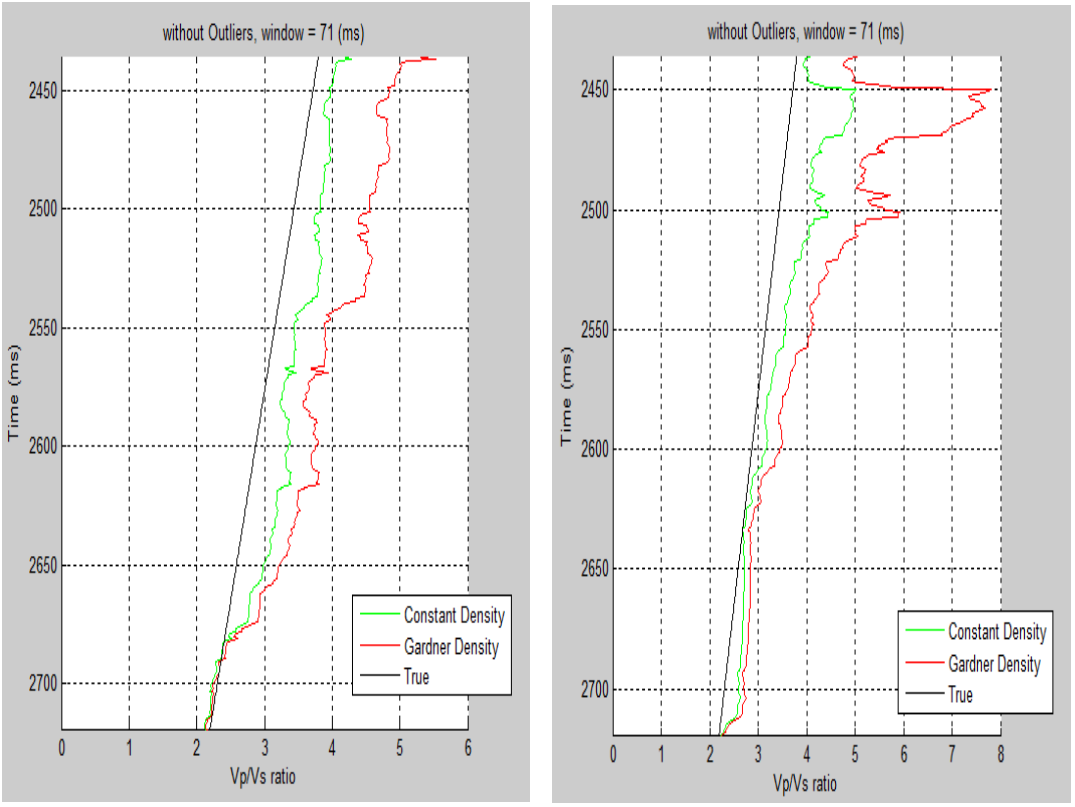

Fig.5.1. It compares the Analytical (left) and Experimental (right) response, with a time window of 71 (ms).

Generally, the Gardner Density follows a relationship between P-velocity and density. In this case the P-velocity and density well logs don't show this relationship (Figure 5.2).

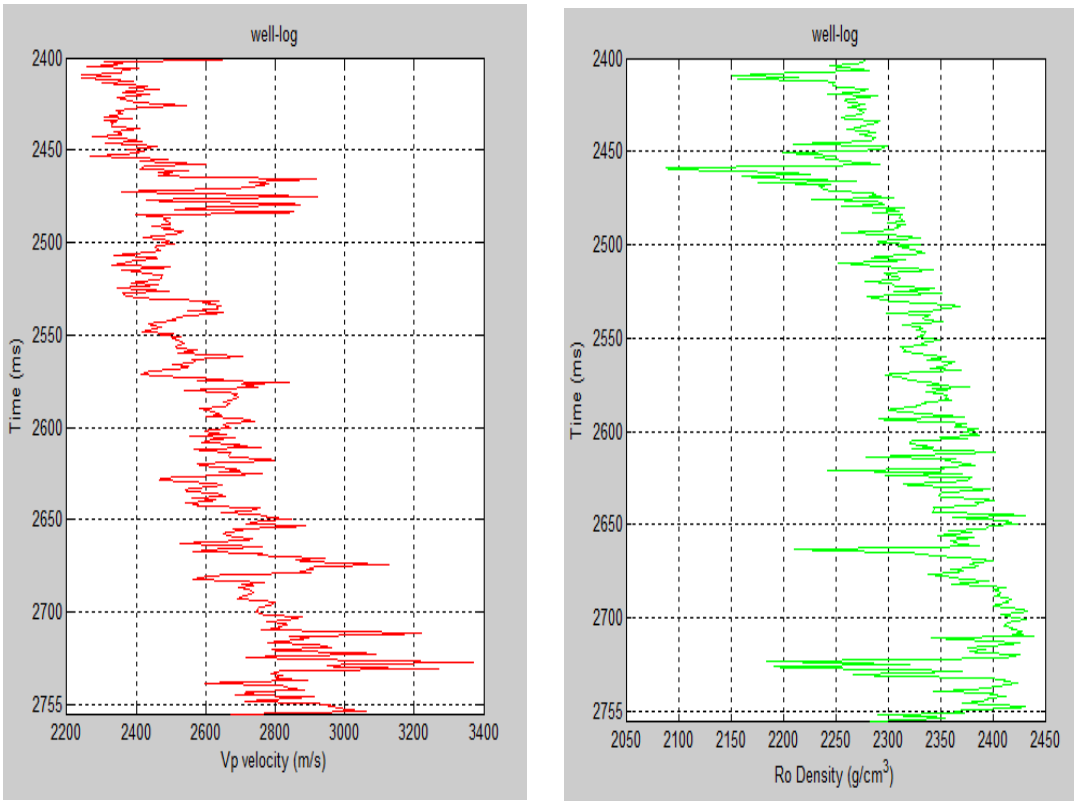

Fig.5.2. Vp velocity (left) and Ro density (right).

This could be a reason because the Gardner Density shows a Vp/Vs ratio greater than Costant Density.

It have applied a low pass filter with a cut-off frequency of 10 Hz, attempts to define a low resolution profile of Vp/Vs ratio and not its local variations of high frequency. Filter results, improve the values Vp/Vs predicted, mostly when I apply a time window of 91 (ms).

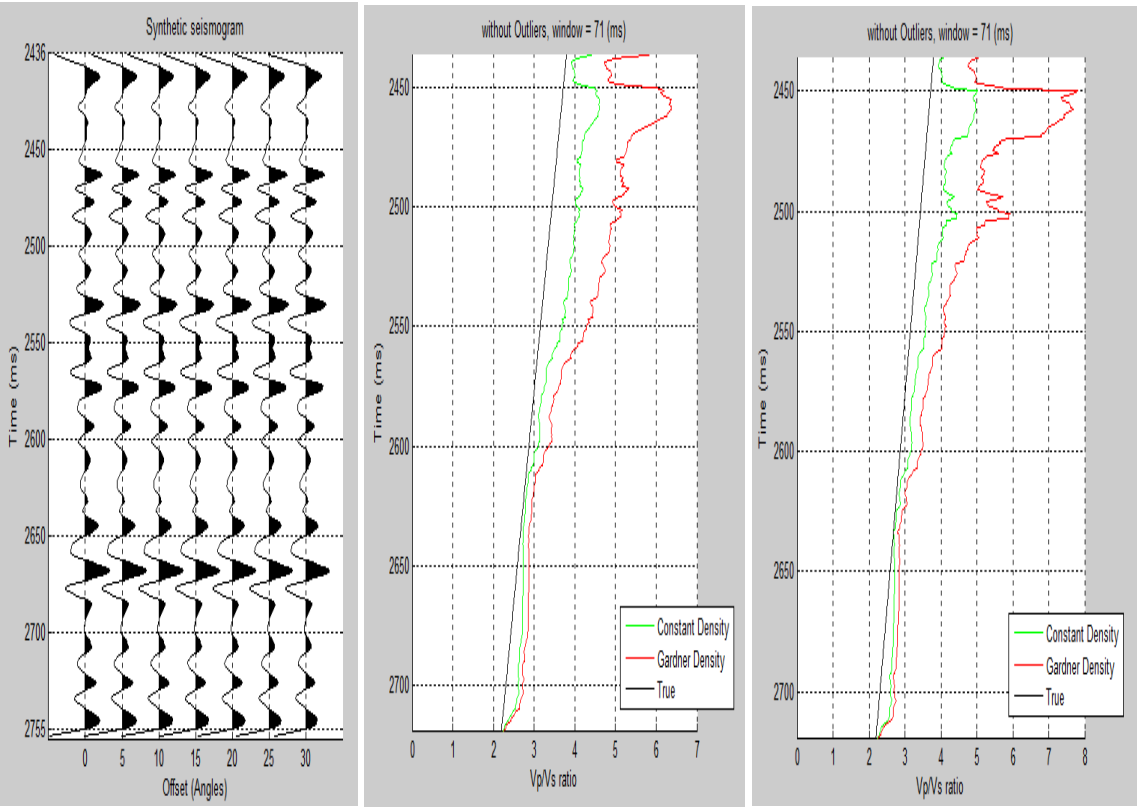

Fig. 5.3. The synthetic seismogram (left), in the middle with the low-pass filter application and (right) without the low-pass filter application. With a time window of 71 (ms).

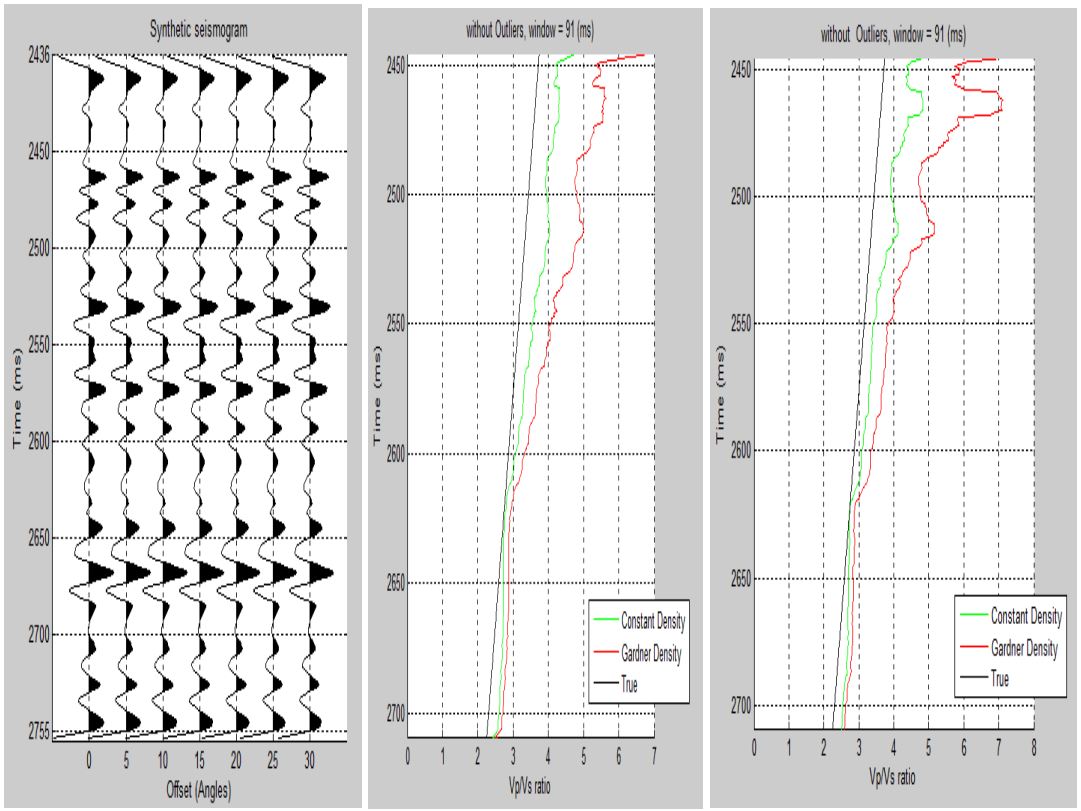

Fig. 5.4. The synthetic seismogram (left), in the middle with the low-pass filter application and (right) without the low-pass filter application. With a time window of 91 (ms).

Considering the correct relationship of Vp/Vs ratio with a time window of 91 (ms):

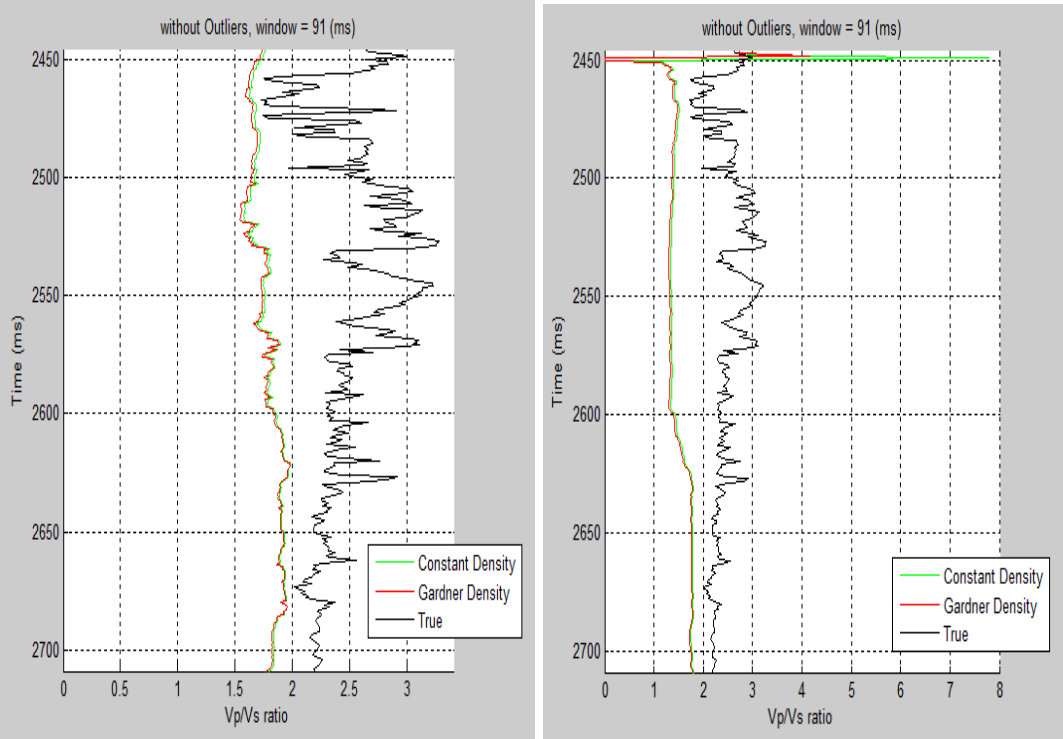

Fig. 5.5. It compares the Analytical (left), and Experimental (right) response with a low-pass filter application, with a time window of 91 (ms).

The values Vp/Vs predicted in the Analytical response are close to the true Vp/Vs, while, in Experimental response the values Vp/Vs predicted show a deflected opposite trend from true Vp/Vs. The problems encountered in all Experimental response, but mostly when I consider the correct relationship of Vp/Vs (METTERE IL NUME>RO della figura di questo ultimo esempio), they could be due :

In intrinsic attenuation, also referred to as absorption, the seismic wavefield loses energy in the form of heat as it travels through the Earth. The degree of absorption is a property of the material through which the energy is travelling. Absorption is frequency dependent, with higher frequencies being more attenuated than low frequencies. For deeper targets, this will lengthen the wavelet still further, causing loss of resolution as well as amplitude. The frequency-dependent nature of the energy loss also causes a distortion in phase. Extrinsic attenuation includes a number of factors such as mode conversion and scattering,

which also contribute to energy loss. Since far offsets travel longer in the Earth than near offsets, attenuation is offset dependent; because it is determined largely by lithology it will vary spatially. In isotropic media, thin layering causes interference between the top and bottom reflections. Interference tends to increase with offset when the reflection target has a higher velocity.

I have considered a ratio Vp/Vs that varied linearly from 4 to 2 and then returned again to a ratio of Vp/Vs = 4, with a standard deviation of 0.01. In the interval from 2800 to 3000 (ms), where it has observed an abnormally high Vp/Vs depth trend, it may interpret this interval as an overpressure interval. Poisson's ratio decrease with depth in the first 2800 ms of the interval and then starts to gradually increase due to overpressure.

Low-pass filter application with a standard deviation of 0.01:

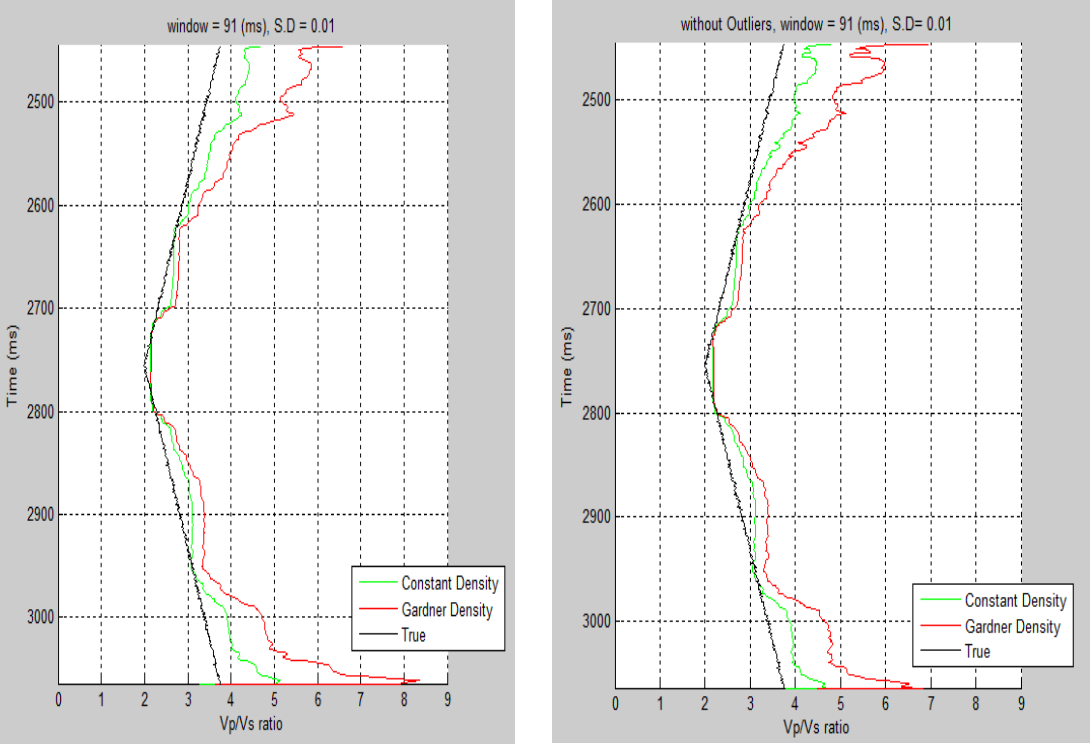

Fig. 5.6. Vp/Vs model (left) with outliers, and (right) without outliers. Applying a time window of 91 (ms).

Reccomandation

On future work a accurate relationship between P-valocity and density well logs, these relationship link the petrophysical property under investigation to the observed seismic response. In AVA forward modelling, the option exist to include the scattering effect in the calculation of the effective reflection coefficient.